FRACTURE ANALYSIS IN A STEEL PLATE

by

© Abdullah Jamaly

A Thesis submitted to the

School of Graduate Studies

in partial fulfillment of the requirements for the degree of

Master of Engineering

Faculty of Engineering and Applied Science

Memorial University of Newfoundland

May 2019

St. John’s Newfoundland and Labrador Canada

Abstract

This research study is carried out to investigate the ultimate strength of a steel plate under the effect of an ice load. Fracture onset is predicted by numerical and analytical analyses, and compared with experimental results. The test setup is designed based on theoretical and FEA models. In the theoretical solution, a model is developed to predict fracture onset in a steel plate. LS-DYNA is used in simulating the fracture onset. The numerical and theoretical results are compared with experimental results. It has been shown that the theoretical solution provides an accurate prediction of fracture onset with a critical strain level of 20% for mild steel plate and that FEA provides more accurate results in comparison to the theoretical solution for high tensile strength steel plates.

Acknowledgements

This research has been carried out under the supervision of Dr. Claude Daley and Dr. Bruce Colbourne as a part of STePS2 project. I am most grateful for their support and patience during this research program. I would like to acknowledge and thank Dr. Bruce Quinton for his guidance during the design of the experiment and Mr. Mathew Curtis for his assistance in the laboratory. I also wish to thank Dr. Ayhan Akinturk for his support during my master's program. Last but not the least, I would like to express my gratitude to my family and especially to my love Tayyebe who has always been patient and enthusiastic. Without her support, I would not have been able to complete this research. This thesis is dedicated to her.

Table of Contents

List of Tables

List of Figures

List of Appendices

Chapter 1: Introduction

1.1 The Need to Navigate and Operate in Polar Waters

The Arctic plays an important role in world economics. The increased opportunities, arising from huge oil and gas fields and shorter shipping routes, have enlarged marine operations in the Arctic. According to an assessment by the US Geological Survey (USGS) in 2008, the undiscovered hydrocarbon resources in the Arctic are estimated to be 412 billion barrels of "oil equivalent", that is, about 13 and 30 percent of world's undiscovered oil and gas, respectively (Bishop A., 2011). In 1972, the first offshore structure in the Arctic was constructed to operate in only 3 meters of water depth in the Beaufort Sea (Sanderson T. 1988). Since 1972, the high demand for oil and gas has directed explorations from shallow to deep waters.

In addition to the oil and gas reservoirs in the Arctic, the Northwest Passage and Northern Sea route in this area considerably reduce the international shipping distances (Figure 1-1). The Northwest Passage connects the Atlantic and Pacific Oceans through the Arctic Archipelago across the north of Canada. It reduces the shipping distance between the west coast of the USA and Europe by 3,200 kilometers and the distance between Tokyo and London to 12,800 kilometers from 23,600 kilometers, when the Suez Canal cannot be used. It would also permit the navigation of larger ships than the dimensions of the Panama and Suez canals (Abraham J. 2008). The Northern Sea route that is on the other side of the Arctic Ocean passes along the Russian coast of Siberia and crosses five Arctic seas, including the Barents Sea, the Kara Sea, the Laptev Sea, the East Siberian Sea and the Chukchi Sea. Using this route, the navigation distance from Rotterdam to Yokohama decreases to 8,500 kilometers from 20,800 kilometers via the Suez Canal, which means the

reduction of transit time to 16 days from 33 days. The reduction in navigational distance will not only make benefits with a shorter transit time, but also provides a higher productivity of the vessels in a year and the significant reduction of bunker consumption which will lead to lower emissions.

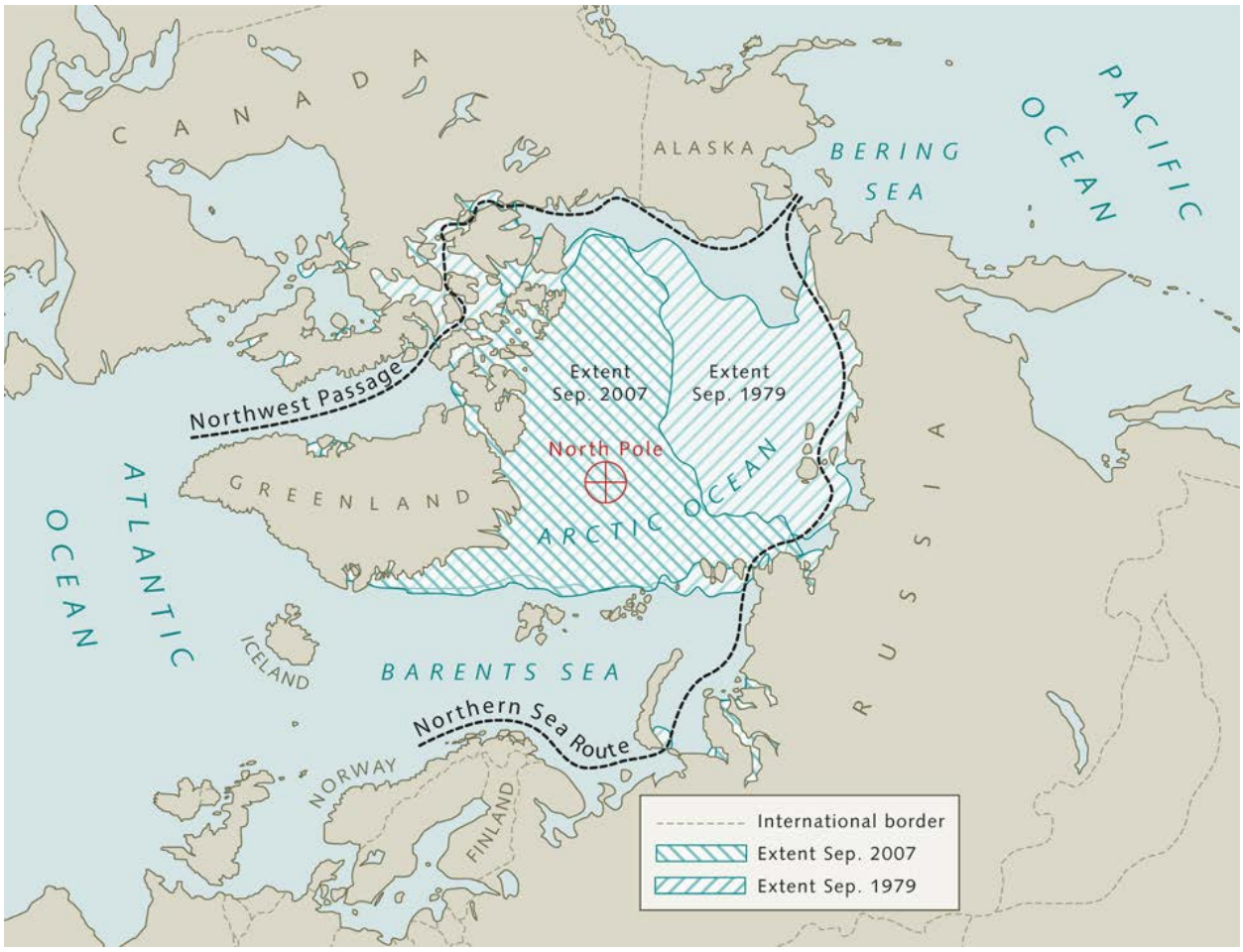

Figure 1-1. Northwest Passage and Northern Sea Route

Despite all the aforementioned advantages, the exploration for the natural resources and transportation in the Arctic requires icebreakers, offshore platform, and ships with ice breaking capabilities.

1.2 Plastic Design in Ice Class Structures

Plastic design is an approach for designing the structure of ice class vessels and offshore structures. In plastic design, using the ductility of the steel structure, local deformations under overload conditions are permitted. This design technique provides a high reserve capacity which will considerably increase the safety margin of the structure. However, if local deformations cause the final failure of the structure and consequently, a total loss of the structural stability, the benefits of this design method will not be valuable anymore. Therefore, in comparison with elastic design, the plastic design method requires consideration of various limit states in the plastic zone.

Under extreme loads such as ice loading, the reserve capacity of the structure provides a higher strength margin. It provides a lighter structure, that is an advantage for the whole life of the ship. However, the difficulties in accurate estimation of the rupture initiation complicate determining the “real safety margin” in plastic limit state design (Paik et al. 2002).

Limit state is defined as the condition where the structure is not suitable for its design objectives; it occurs due to the applied loads. Paik et al, 2002, divide the structural limit state into four types, including “Serviceability Limit State (SLS), Ultimate Limit State (ULS), Fatigue Limit State (FLS) and Accidental Limit State (ALS)”. In SLS, the structure cannot continue to provide the service that it is designed for due to problems such as deflection in the deck plate or elastic buckling. ULS identifies the total failure of the structure as a result of “loss of structural stiffness”. It may occur due to reaching the maximum strength of the structure’s members, equilibrium failure in the structure and

instability in the structure following buckling or plastic collapse of the structure. Two examples of ULS are collision and grounding, when the structure reaches the ultimate limit state. (Lamb T. 2003)

In limit state design, the ductility of the steel structure is used to develop the reserve capacity of the structure beyond the yield strength. The strain hardening of the steel contributes to the development of ductility in the structure. In Figure 1-2, this distribution is presented in a unit thickness of steel material under an applied bending load. The ductility helps to use the reserve capacity of the structure. The reserve capacity is a result of strain hardening of the steel material. In Figure 1-2, the stress distribution is linear in the cross section up to the point that the yield stress limit initiates at an extreme distance from the neutral axis (point a). A further increase in load level distributes the yielding across the section and beyond that point (c), an increase in load level may collapse the structure.

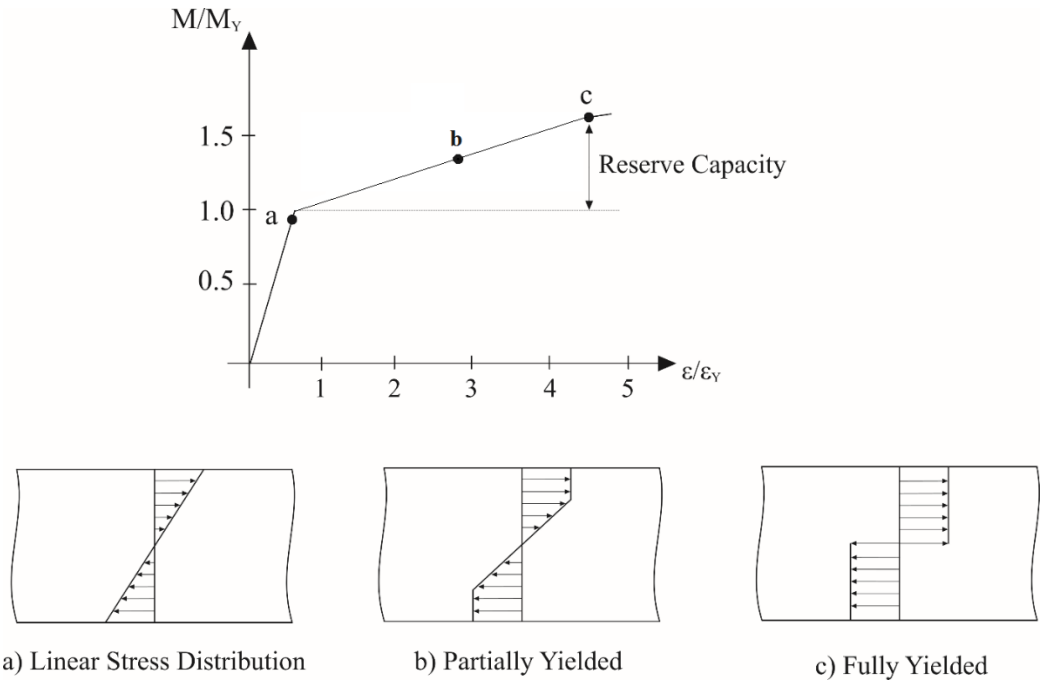

Figure 1-2. Development of reserve capacity in steel structure (SSC 393, 1997)

In recent years, different design standards have been developed based on limit state design. Goal-Based Standards (GBS) have been developed by the International Maritime Organization (IMO) and are applicable to bulk carriers and oil tankers constructed on or after July 1st, 2017. In the second tier of GBS, the design of the structure based on ultimate strength is a functional requirement in the design stage (MSC Res. 287(87)). In 2006, the Common Structural Rules (CSR) were developed by the International Association of Classification Societies (IACS) to achieve more robust design and safer ship structures. The CSR requirements are applicable to double hull oil tankers with a length of more than 150 m and to bulk carriers having a length of more than 90 m, constructed on or after April 2006. The CSR requirements can be considered as a pilot for IMO GBS requirements, where the structural scantling should be provided by direct fatigue and strength analysis (Bamford and Stewart).

In 2008, IACS developed Unified Requirements (UR) for ice class ships. In the UR for Polar Ships (UR I), using the plastic limit state equations, local deformations of the structure are permitted under ice loading, if the total integrity of the structure will not be endangered as a result of the local dents (Daley C. 2001). In this UR, the limit states for modeling of frame capacity are derived and validated by finite element analysis. In this model, since the large deformations and membrane stresses are ignored, the analytical solutions underestimate the capacity of frames (Abraham J. 2008). The background and derivation of the formulae in the Unified Requirements for Polar Ships are discussed in Daley C. 2001.

The classification societies have also developed Ice Class Rules for different ice conditions. In Table 1-1, the summary of Ice Class notations in IACS UR I, ABS and DNV rules is presented. In the ABS rules, in addition to multi-year Ice Class notations (PC1 to PC7), lower Ice Class Notations (A0, B0, C0, and D0) are developed for first year ice conditions (ABS Rules, Part 6). In DNV rules, the frame warping effects for unsymmetrical cross-sections are also considered and developed (Rahman M. 2012).

Table 1-1. The summary of Ice Class notations in IACS UR I, ABS and DNV rules

Reference	Ice Class Notation	Notation Description	Ice Thickness
IACS	PC-1	Year-round operation in all polar waters	-
	PC-2	Year-round operation in moderate multi-year ice conditions	-
	PC-3	Year-round operation in second-year ice which may include multi-year ice	-
	PC-4	Year-round operation in thick first-year ice which may include old ice	-
	PC-5	Year-round operation in medium first-year ice which may include old ice	-
	PC-6	Summer/autumn operation in medium first-year ice which may include old ice	-
	PC-7	Summer/autumn operation in thin first-year ice which may include old ice	-
ABS	Ice Class A0	Year around navigation in water with first-year ice with: Extreme ice conditions while escorted by PC4 or higher Ice Class vessel or very severe ice conditions while escorted by PC5 or higher Ice Class vessel	0.6 m and above 0.3 m and above
		Independent year round navigation in water with first-year ice with severe ice conditions	0.3 m and above
	Ice Class B0	Year around navigation in water with first-year ice with: Extreme ice conditions while escorted by PC3 or higher Ice Class vessel or	0.6 m and above

		very severe ice conditions while escorted by PC5 or higher Ice Class vessel	0.3 m and above
		Independent year round navigation in water with first-year ice with medium ice conditions	less than 0.3 m to 1.0 m
	Ice Class C0	Year round navigation in water with first-year ice with very severe ice conditions while escorted by PC5 or higher Ice Class vessel	0.3 m and above
		Independent year round navigation in water with first-year ice with Light ice conditions	less than 0.3 m to 0.6 m
	Ice Class D0	Independently Year around navigation in water with first-year ice with very light ice conditions	less than 0.3 m
Finish – Swedish Ice Class rules	IA Super	Capable of navigating in difficult ice conditions without the assistance of icebreakers	1.0 m
	IA	Capable of navigating in difficult ice conditions, with the assistance of icebreakers when necessary	0.8 m
	IB	Capable of navigating in moderate ice conditions, with the assistance of icebreakers when necessary	0.6 m
	IC	Capable of navigating in light ice conditions, with the assistance of icebreakers when necessary	0.4 m
DNV	ICE-15	Encountering winter ice with pressure ridges. No ramming is anticipated.	1.5 m
	ICE-10		1.0 m
	ICE-05		0.5 m
	POLAR-30	Encountering winter ice with pressure ridges and multi-year ice-floes and glacial ice inclusions. Occasional ramming is anticipated.	3.0 m
	POLAR-20		2.0 m
	POLAR-10		1.0 m

1.3 Ultimate Limit State Design

The plastic design method provides a more economical and reliable design in comparison to traditional design methods based on yield stress. However, the main limitation of using

the plastic design method is the unknown ultimate capacity of the structure. Review of ship accidents at sea shows that the main factors resulting in total loss of structural integrity can be classified into three categories as follows:

- Improper operation of the vessel, i.e., poor loading and unloading
- Structural degradation, i.e., wastage and corrosion in structure
- Lack of limit state design methods in design stage of the vessel

Hughes et al. have reviewed eight different accident cases with a focus on the preceding parameters (Hughes et al., 2010).

Fracture analysis can be classified into three categories: empirically based methods, numerically based methods and analytical methods. A brief review of some research is introduced here. More detailed review of literature studies can be found in the reference publications. Analysis of fracture initiation and crack propagation provides a practical tool for development of the Ultimate Limit State. One of the first studies on fracture analysis in grounding is conducted by Minorsky (Minorsky V. U. 1959). In Minorsky's method, the dynamics of ship collision are analyzed by evaluation of the loss of kinetic energy that is assumed to be absorbed by structural deformation. In his method, he used steel deformation data from actual ship collisions to develop empirical formula. His method can be considered an empirical analysis (Pill and Tabri 2009, Alsos H. 2008).

In 1992, Amdahl and Kavlie studied the stranding of a scaled double bottom structure by using non-linear finite element analysis. In that study, the mesh sensitivity and crushing speed are studied, and it is assumed that the fracture initiates when the effective stress reaches 90% of the ultimate stress (Amdahl and Kavlie). The numerical analysis is

compared with the results of the experimental test. In 1997, Simonsen developed a theoretical method for the analysis of ship grounding on a conical rock with a rounded tip. In that study, it was assumed that during grounding, the intersections between the structural elements remained intact and a model for the calculation of horizontal and vertical forces in a grounding scenario was developed. His model can be used to evaluate the structural damage on shell plating and frames. Simonsen validated his model with experimental large scale tests that showed a deviation of less than 10 percent between the experimental and analytical results (Simonsen 1997). In 2000, Wang et al investigated the behaviour of a double hull structure in different grounding scenarios. They conducted nine scaled experiments in which the indentation of a rigid conical indenter with different tip radii on a scaled double bottom structure was modeled. Using the geometry of collision parameters, they provided a simple analytical method for the prediction of structural behaviour for different sea bed geometries. The test results were in good agreement with the analytical estimation (Wang G. et al., 2000).

In 2004, Simonsen and Tornqvist conducted a combination of experimental and numerical analyses. They studied mode I cracks in steel and aluminium plates. In that study, the empirical criteria for crack propagation were defined by an experimental-numerical calibration procedure and the developed strain criterion was validated. The validated model is used in simulation of a fracture in a grounding experiment and the grounding on a double bottom is modeled (Simonsen and Tornqvist, 2004).

There are limited research studies on structure failure under an ice load. The ultimate capacity of plate panels under an ice load is yet unknown. In 1985, Ratzlaff and Kennedy

developed an analytical method in an effort to analyze ice loads on offshore structures. In that model, they analyzed the behaviour of a long steel plate with "zero aspect ratio"[1] under a uniform transverse load. Although plate fracture is not discussed in that model, it predicts the elastic and plastic behaviour of a steel plate in a reasonable agreement with numerical and experimental data (Ratzlaff and Kennedy 1985). They developed a theoretical solution for the analysis of a steel plate under the lateral indentation of an ice load. In their model, it is assumed that the ice load is distributed along the span of the plate uniformly and by considering a unit width of the plate, the analysis is simplified to a two dimensional problem. Using this hypothesis, the elastic and plastic behaviour of the plate are studied and the governing equations for each state are derived. In another study, Bond and Kennedy (2000) assessed the "post-yield behaviour" of icebreaker hull panels by conducting numerical and experimental analyses of stiffened panels under a lateral load. In one test panel, rupture started at the mid span of a main frame and the crack was propagated to the shell plating (Bond J. and Kennedy 2000).

1.4 Research objectives and thesis overview

Analysis of stiffened panels can be conducted at three different levels, including the entire panel, the stiffened structure and the plate alone (Hughes et al 2010). Plates, as the outer members of the panels, are exposed to environmental loads such as wind, wave and ice loads; therefore, it can be said that the plates are the most important structural members in marine structures (Okumoto et al 2009).

[1] Zero aspect ratio (as defined by Ratzlaff and Kennedy 1985): long narrow plate having width/length ratio approaching zero.

Considering limited resources on estimation of structure capacity, the objective of this research is to study fracture initiation in steel plate and to provide a simplified tool in predicting fracture onset in structure. In this work, the fracture initiation in steel plates is studied to evaluate the ultimate capacity of the plates under a lateral load.

In the elastic design of a steel plate with a constant thickness and an aspect ratio (length to width ratio) of more than 2, the deflection and stress values under the lateral distributed load will be almost equal to the deflection and stress values of a beam with the same length and one unit's breadth. Additionally, in the plastic design of steel plates, as the aspect ratio increases, the coefficient values in the governing equations gradually converge to constant values. Therefore, in the analysis of steel plates with large aspect ratios, the plate behaviour can be reasonably modeled by a beam with a length equal to the plate length and with a unit width.

In a stiffened panel, the beams surround the plate on four edges. The bending rigidity of the edge beams is significantly higher than the plate and therefore, the deflection of boundaries is much smaller than the plate deflection, even up to the collapse of the plate. In addition, the rotational restraint of the beams under lateral pressure tends to be indefinite, due to the symmetrical pattern of plate deformation between the frames. As a result, it is reasonable to assume that the boundaries of the plate are clamped up to the plastic initiation in the edges (Hughes et al 2010).

Considering the behaviour of the plates under a laterally distributed load, in this research, the ultimate capacity of the plate is studied by experimental analysis of a steel plate with

clamped boundary conditions at both ends. The general layout of the initial concept of the experimental design is presented in Figure 1-3.

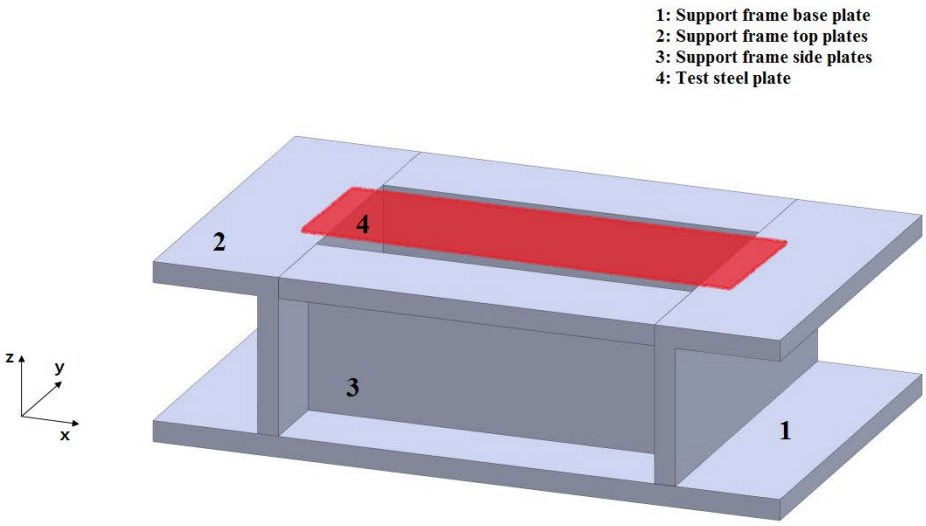

Figure 1-3. The initial concept of the support frame

As shown in Figure 1-4, with a gradually increasing lateral load on a plate, the plate will be deflecting in elastic mode and upon reaching a certain load level, two plastic hinges will form at the plate ends. By increasing the load intensity, a third plastic hinge will form at the middle of the plate and with the further increase of the load, the plastic region will extend in the plate field till the whole plate will change into a plastic membrane. From this point, any increase in the applied load will deflect the plastic membrane, which will lead to in-plane stretching of the plate. Finally, the failure will occur at a welding defect or in the plate material (Okumoto et al 2009).

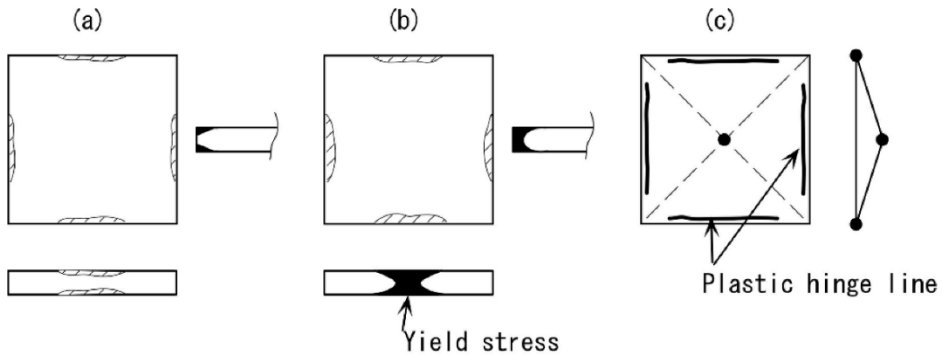

Figure 1-4. Formation of plastic hinges on steel plate under lateral uniform load (Okumoto et. al., 2009)

In Figure 1-5, the behaviour of a thin steel plate under lateral pressure is presented. In this figure, the dashed line represents the load-deflection of the plate under “flexural action” only (Curve F). The dashed-dotted line shows the load-deflection behaviour under “membrane action” only (Me) and the solid line presents the total load-deflection behaviour of the plate (Curve E).

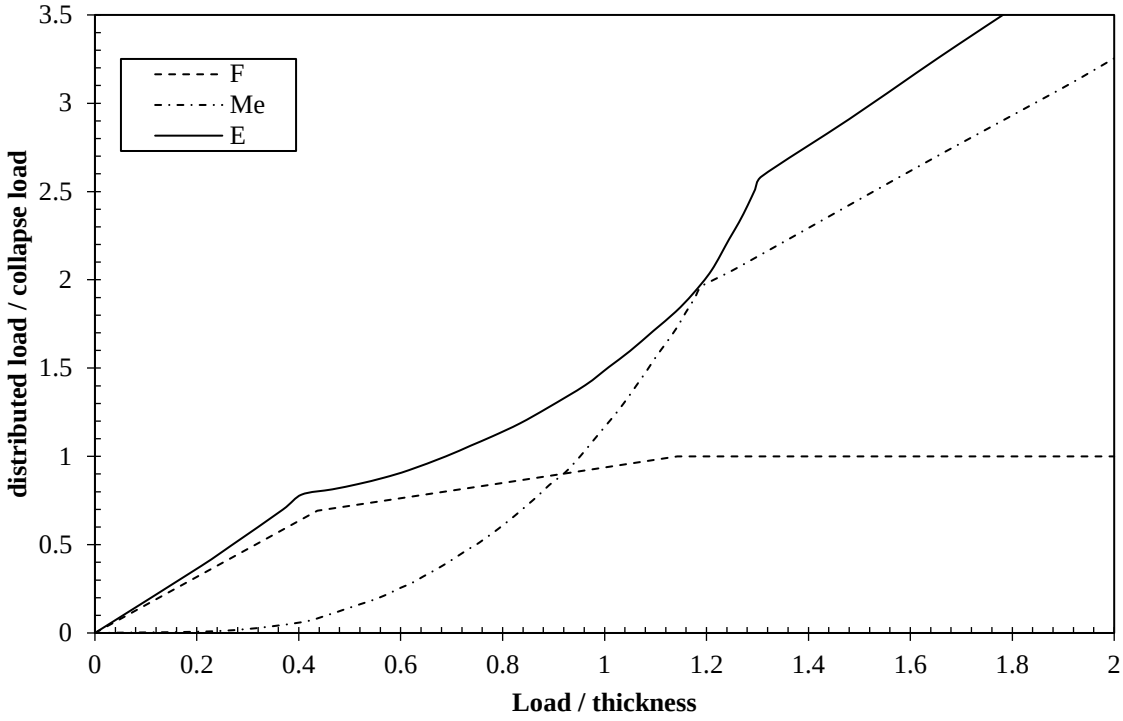

Figure 1-5. Behaviour of thin plate under lateral uniform pressure (Ratzlaff et. al., 1985)

On the flexural action curve (F), the load-deflection behaviour consists of three straight lines representing elastic behaviour, formation of edge plastic hinges and middle plastic hinge, respectively. The membrane behaviour curve (Me) presents the load-deflection relationship with two curves. The first portion of the trend represents the plate behaviour starting from a zero-deflection state to a full plastic membrane state and the second portion on the right presents the stretching of the plate in a plastic state to the rupture initiation. The solid line (E) diagram is the combination of flexural and membrane behaviours under lateral pressure. In this figure, it can be seen that the membrane effect dominates the flexural effect in the plastic region in larger deflections. Therefore, in a large deflection of the plate, it is acceptable to consider the membrane effect only and neglect the effect of flexural action. However, it should be noted that for thicker plates, the flexural effect will

dominate the membrane action, even in the plastic region. The effect of plate thickness on load-deflection behaviour is studied for three plates with thick, intermediate and thin thicknesses by Daley C., 2014. The analytical study of the governing equations for load-deflection behaviour are explained in Section 2.2.

The bending of a plate with a large aspect ratio under lateral pressure will mainly form in one direction only. Therefore, for the failure criteria, it is assumed that the rupture will initiate when the uniaxial strain in the plate field reaches a critical value (Wang G. et al., 2000). It should be noted that the transverse shear force at the plate ends requires the consideration of shear limit as another failure criterion in combination with the uniaxial strain. Experiments conducted by Ratzlaff and Kennedy, in 1985, show that in a rectangular thin plate under lateral distributed pressure, the rupture initiation occurs close to the plate edge, upon reaching the shear limit (Ratzlaff and Kennedy, 1986). In large deflections, the clamped boundary condition at the plate edges applies excessive bending moments, due to the eccentricity of the axial force. This effect will make the plate edges more prone to rupture initiation (Ratzlaff and Kennedy, 1986). The shear limit effect is not studied in this research. Therefore, the support frame end plates and test specimen profile are modified to eliminate the effect of shear stress. Figure 1-6 shows the layout of the test setup.

#	Description
A	Longitudinal
B	Curved Bracket
C	Top Horizontal
D	Lower Horizontal
E	Vertical Rib
F	Curved End
G	Test Plate
H	Upper Bar
I	Key
J	Bolt and Nut 5/8"

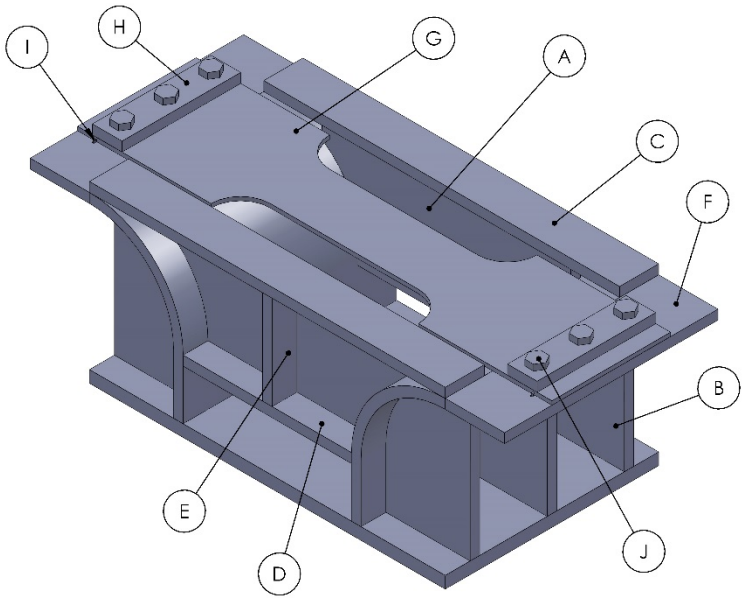

Figure 1-6. Layout of the final experimental design

In the current study, the fracture initiation is analyzed by both numerical and experimental models. The objective of this research is to study the ultimate capacity of a steel plate under lateral indentation. A supporting frame has been designed to conduct the experiments on steel plates, while considering the laboratory limitations. In the design stage of this research, the LS DYNA software program is used to simulate fracture onset and to design the test supporting frame. As a side study, theoretical calculations are used to evaluate the total load required to initiate fracture in the steel plate. Later, the test supporting frame is fabricated using the facilities at Technical Services of the Faculty of Engineering and Applied Science at Memorial University of Newfoundland and the experiments are conducted in the Structure Laboratory.

In Chapter 2, the design of supporting frame and test specimens are described based on theoretical and numerical analyses. The capacity and scantling limitations of the test machine are introduced and considered in the experimental design.

In Chapter 3, Finite Element Analysis (FEA) is discussed and the results of the behaviour of the test specimens and supporting frame are studied. The design and installation of the test supporting frame and test plates are presented in Chapter 4. The experiment results for each test are described and the results are discussed.

Chapter 5 contains the comparison of FEA and theoretical analyses with regard to experiment results and the conclusions.

1.5 Summary of contributions

In this research, fractures in steel plates are studied through theoretical, numerical and experimental analyses. Throughout this study, a unique experimental setup has been designed and fabricated. The test specimens have been specifically designed to simulate fracture onset without the effect of supporting members. Theoretical and numerical analyses have been used to design the experiment and then the experiment results are used to validate the initial analyses.

Chapter 2: Experimental Design

2.1 Test Setup Design

A hydraulic test machine with the maximum load capacity of 1500 kN (300 kip) is used to apply the lateral load on the test specimen. In Figure 2-1, the general outline of the machine with the test setup is presented.

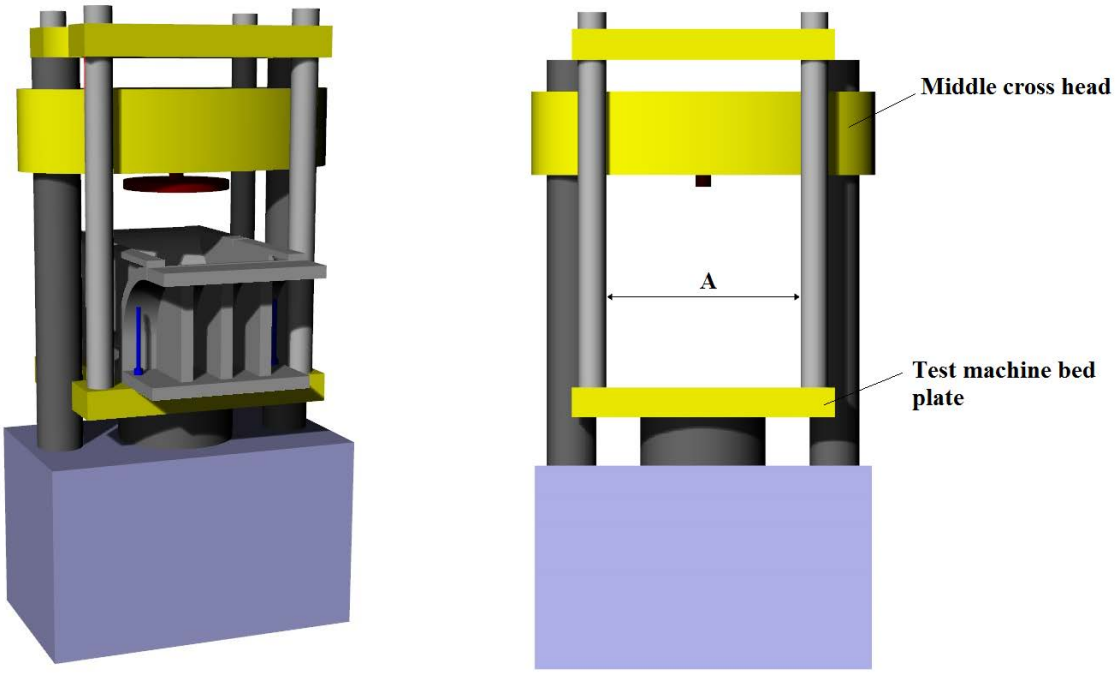

Figure 2-1. Layout of hydraulic test machine

The total stroke of the testing machine is 229 mm, imposing a limitation on the total indentation distance. Another limitation is related to the total clearance between screws, distance A shown in Figure 2-1, that is 610 millimeters. Therefore, the width of the supporting frame should be less than this value. The testing speed of the machine can be adjusted between 0 to 76 millimeters per minute.

The initial support frame was a steel box with relatively rigid boundaries with an open top surface to install the test specimens (Figure 1-3). However, in that design, the sharp edges

at the ends apply a high shear force on the plate edges, as described in Section 1-4, which would lead to high shear load at the ends. As described in Section 1-4, high shear loads will result in final rupture of the plate close to the boundary before rupture initiation at the center. The Finite Element Analysis and theoretical analysis proved this behaviour too. The related theoretical calculations are presented in Section 2.2. The two edges of the test setup were changed to a curved profile to avoid a high level of shear force on the test plate close to the boundary edges. Using Finite Element Analysis (FEA) and also considering the capacity of the workshop's bending machine, a range of boundary curvature radius was analyzed and a radius of 150 millimeters was chosen. The width of the test plate in the central region was reduced to avoid high shear loads at the edge of the test specimen prior to plate rupture in the central region. Various combinations of edge and plate width with different transition radii were analyzed by FEA. Figure 2-2 shows the top view of the final profile of the test specimen with the edge and central width and the transition radius.

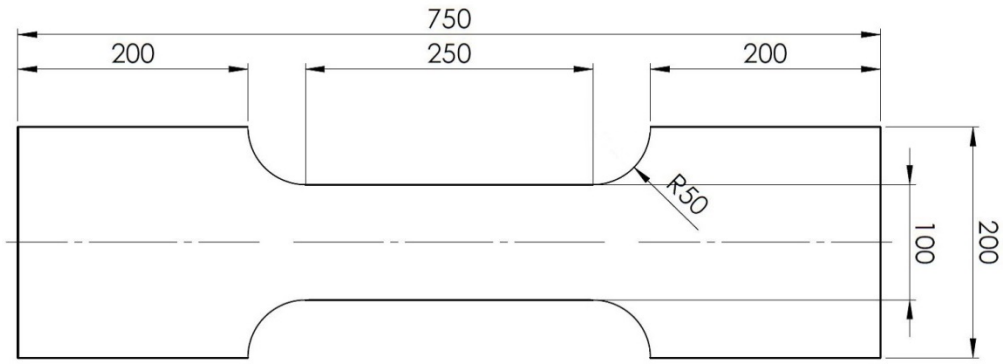

Figure 2-2. Layout of the test specimen (dimensions in millimeters)

In designing the length and width of the test plate, the test machine's dimensional limitations had to be considered. Due to the limitation on the stroke of the test machine, the

total depth of the support frame was limited to the maximum stroke. Therefore, the plate rupture should occur at a deformation of less than the total stroke.

Considering these limitations, numerical and theoretical analyses were conducted to specify the scantling of the supporting frame and the thickness of the test specimen. The FEA model and the related results are presented in Section 2.3 and in Chapter 3. Theoretical calculations are described in Section 2.2.

In the FEA, the stress and strain level in the boundary condition is monitored and the design is made reasonably rigid to keep the relative motion of the edges as low as practicable. In Figure 2-3 the general layout and the scantling of the support frame are presented.

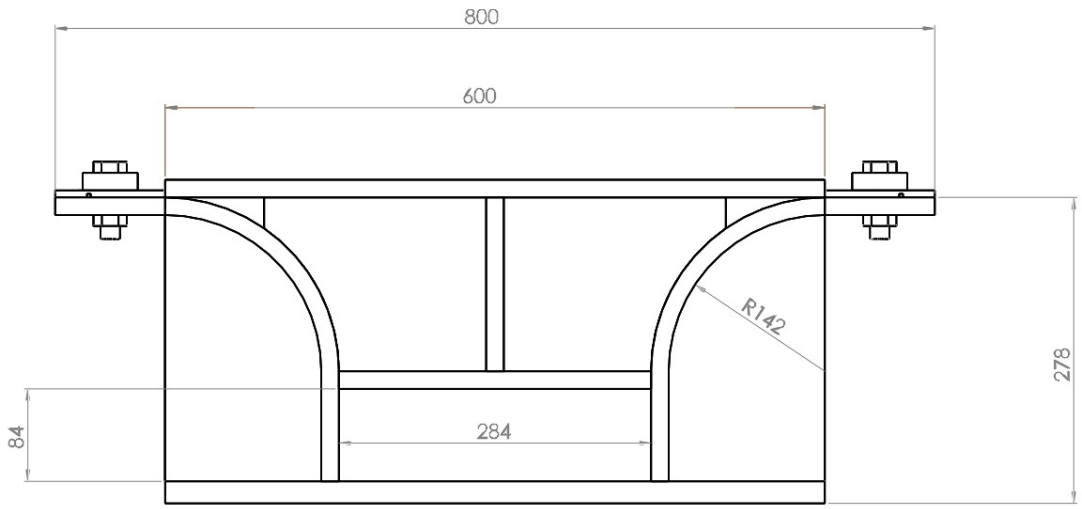

Figure 2-3. The layout of the support frame (dimensions in millimeters)

In Table 2-1, the summary of the scantling and grade of materials used in the test setup is presented.

Table 2-1. The properties of steel plates used in the experiment

Part	Grade	Thickness		Area
Boundary condition	High Strength Steel	19 mm	3/4 in	Lower base plate
Boundary condition	High Strength Steel	16 mm	5/8 in	Other than # 01
Test plate – Thin	Mild Steel	3.175 mm	1/8 in	-
Test plate – Thick	High Strength Steel	6.350 mm	1/4 in	-

In the test design, a combination of bolt and key is used to connect the test plate to the supporting frame (See Figure 2-4). In comparison to a welded connection, bolt connection provides an easier setup and does not require the welding and cutting of broken samples after each test.

The key is used to increase the cross-sectional area of the contact interface and to reduce the shear load in the bolts. It helps to decrease the total area of the drilled hole in the test plate and support frame and to reduce the stress concentration at the ends. In order to design the bolts, the total forces applied to the plate edges are measured using FE analyses and by direct calculations, the estimated forces are used to calculate the required material and diameter of the connecting bolts. Based on the direct calculations, three Grade 8 bolts with the nominal size of 5/8 inches are used at each end of the connection joint. The relevant direct calculations are presented in Appendix 1.

The scantling of the key and keyway was determined by FEA. In its design, the critical depth of the slot on the supporting frame and test plate was considered to avoid crack propagation on the slot corner. Table 2-2 provides a summary of the properties of the bolts and keys used in the test setup.

Table 2-2. Specification and mechanical properties of the bolts and keys used in the experiments

Item	Qty	Scantling	Material	Tensile Strength	Yield point
Bolt and Nut	6	Hex Bolt - Nominal diameter 5/8”	Grade 8	1035 MPa	895 MPa
Key	2	L, b, t (mm): 205, 6.35, 3.175	Low Carbon Steel	440 MPa	370 MPa

Figure 2-4 shows the arrangement of the test plate and support frame. As shown in Figure 2-4, in addition to bolts and a key at each end, a steel bar is used on top of the test plate. The bolts are passed through the bar, test plate and the boundary edge. The key was not used for the thin plate.

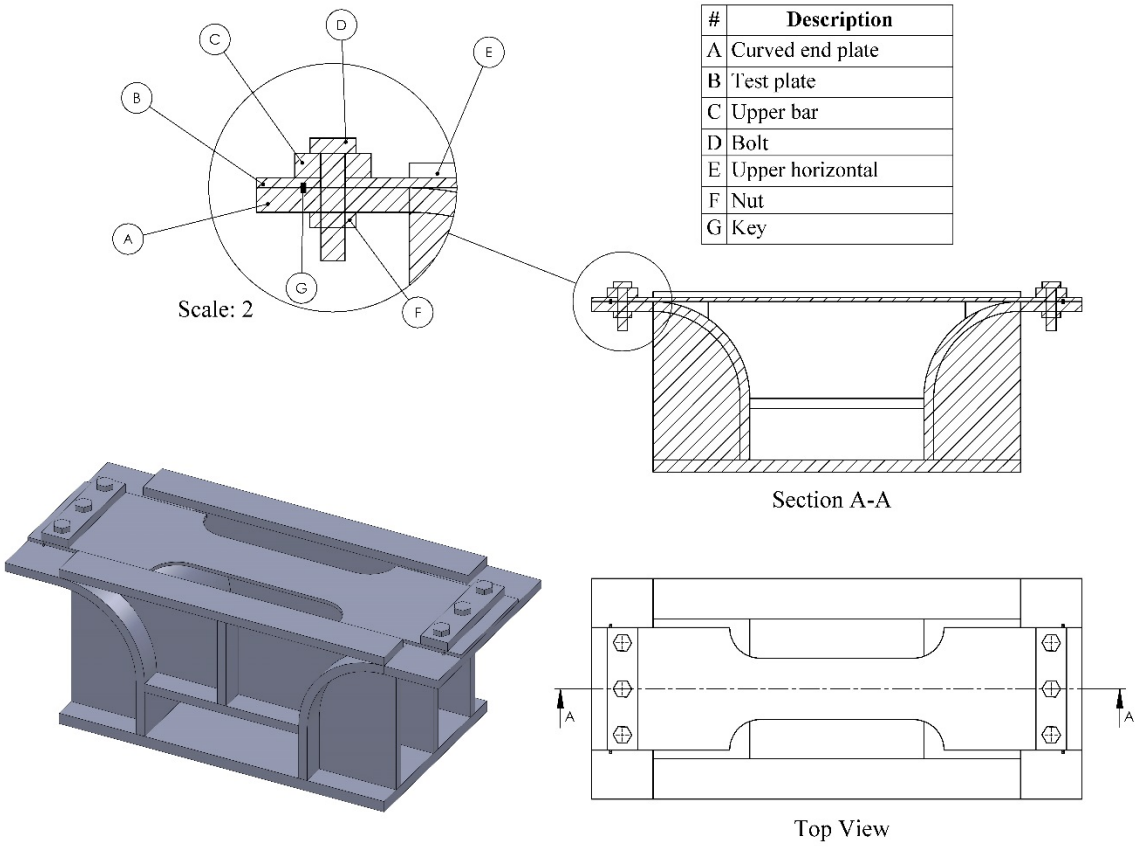

Figure 2-4. The arrangement of end connection

In this study, rigid and soft indenters are used for the crushing experiments. The rigid indenter material is mild steel and the soft indenter material is High Density Polyethylene (HDPE). The physical and mechanical properties of HDPE material are presented in Table 2-3.

Table 2-3. Soft indenter mechanical properties

Property	Value	unit
Density	959.19	kg/m^3
Yield point	29.37	MPa
Elongation at yield	18	%
Tensile strength	30.46	MPa
Young's modulus	1.55	GPa

To simulate two-dimensional failure, a constant cross section is used for the indenter along the width of the test plate. A semicircular cross section profile is selected to avoid the plate rupture under the contact face due to the high stress near the sharp edges of the indenter. The total lateral deflection of the test plate up to fracture onset identifies the required penetration depth by the indenter.

Figure 2-5 shows the layout of the indenter on the test machine and its components. The connection of the indenter head to the stud is provided by a long stud, two securing holed plates and two heavy nuts. This combination is used to ensure that the indenter is fixed in place under the maximum design load of the experiment. As shown in Figure 2-5, the stud is first passed through the middle crosshead of the test machine and is hung from the crosshead using the upper keeper plate and the top-heavy nut. On the lower surface of the

crosshead, the stud is fixed in place using the lower keeper steel plate and the bottom heavy nut. The other end of the stud is bolted to the threaded hole on the indenter head.

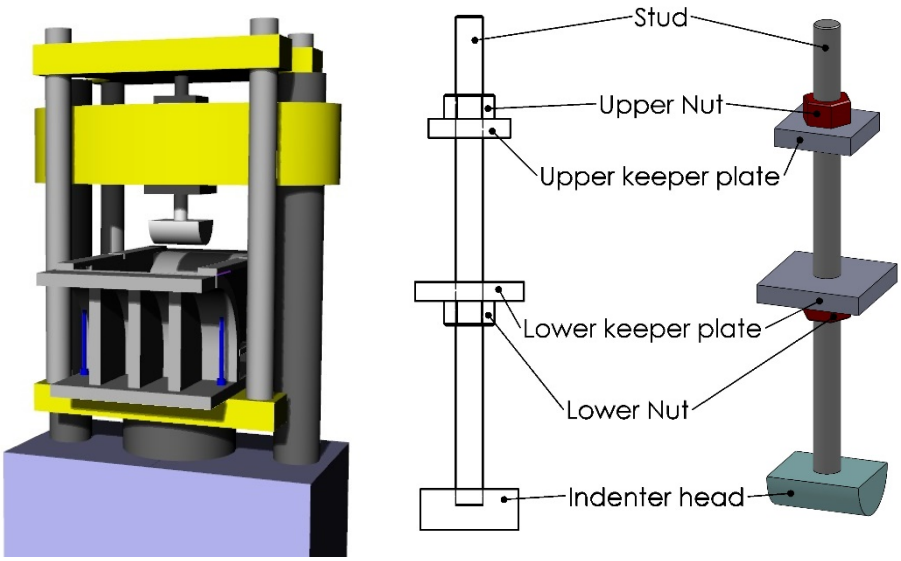

Figure 2-5. The arrangement of indenter

2.2 Theoretical Analysis

As stated in Chapter 1, Ratzlaff and Kennedy developed a theoretical solution for analysis of a steel plate under a lateral indentation of ice load. In this study, this solution method is developed to a partial load distributed on the center of the plate. Critical rupture strain is used as the criterion for the fracture initiation in the steel plate. This criterion employs a simple tool to predict the fracture onset that keeps the calculations simple while achieving reasonable results in comparison with the experimental data (Wang G. et al. 2000). In this study, critical rupture strain of 20% or 0.2 has been used as the failure criterion. This criterion has been used by Wang G. et al. in analysis of plate rupture with reasonable results

(Wang G. et al. 2000). Based on this failure criterion, the fracture onset happens when the strain reaches the critical strain value equal to 0.2.

As described in the earlier sections, it can be assumed that the bending of a long plate occurs in one direction only. In Figure 2-6, the side view of a plate with a unit width normal to the x-z plane and under the effect of a lateral load is presented. In this figure, the load intensity, load extension, plate length and plate thickness are designated by q, b, L and t, respectively.

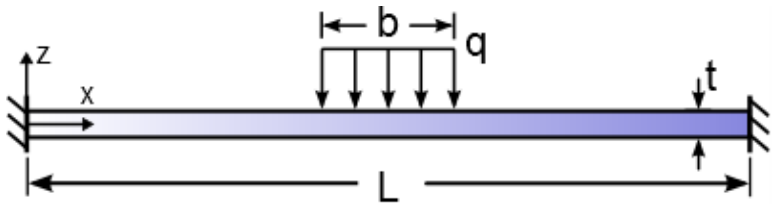

Figure 2-6. Side view of the loaded plate.

Since the plate thickness is much smaller than the plate span, it is reasonable to denote $t \ll L$. Therefore, the membrane behaviour exceeds the flexural behaviour in large deflections and the effect of flexural resistance can be neglected in large indentations. However, in the elastic region with the significant flexural effect, the model can be considered as the “lower bound” of the plate behaviour (Ratzlaff and Kennedy, 1985).

The relationship between lateral load, membrane force at the plate end and the deflection along the plate length were established by considering the free-body diagram of the plate (Figure 2-7). Since the membrane effect is the dominant effect in larger deflections, the bending moments are not considered in the free body diagram.

The relationships between load intensity, horizontal reaction force and beam deflection in three regions of the plate can be found by considering the moment equilibrium of the free-bodies and are as follows:

In Region 1:

$$q = \frac{2F_x w(x)}{bx} \qquad \text{Eq. (2-1)}$$

In Region 2:

$$q = \frac{8F_x w(x)}{-4x^2 + 4Lx - (L-b)^2} \qquad \text{Eq. (2-2)}$$

In Region 3:

$$q = \frac{2F_x w(x)}{b(L-x)} \qquad \text{Eq. (2-3)}$$

where

F_x = Horizontal reaction force

w(x) = Plate deflection in x direction.

At the left end of the plate, the membrane force, F, is:

$$F = \sqrt{{F_x}^2 + \left({qb}/{2}\right)^2} \qquad \text{Eq. (2-4)}$$

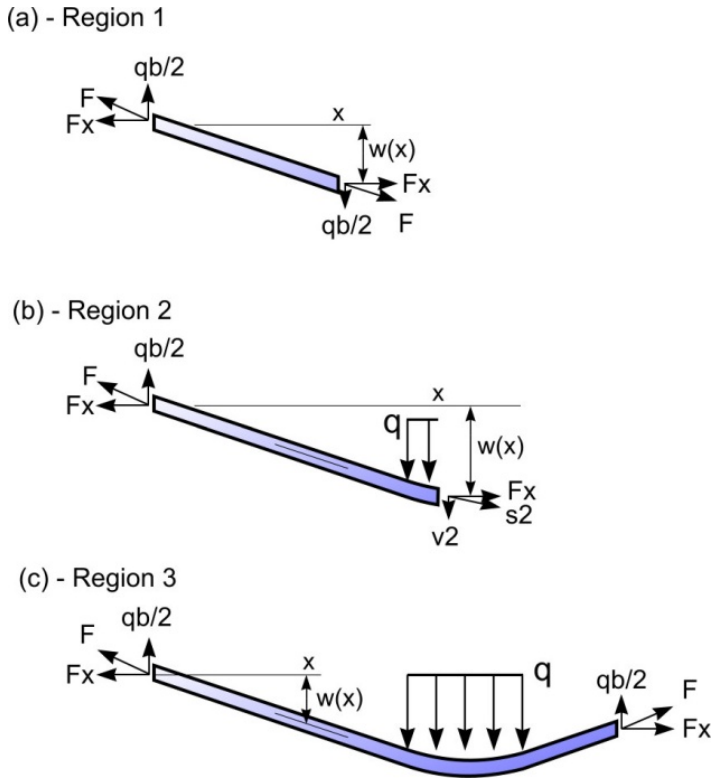

Figure 2-7. Free body diagram of plate side view in region 1, 2, and 3.

Knowing that maximum deflection w_m occurs at the middle of the plate where x=L/2, from Eq. 2-2 it can be found that:

$$w_m = \frac{qb(2L-b)}{8F_x} \qquad \text{Eq. (2-5)}$$

Now, by combining Eq. 2-4 and Eq. 2-5, the load intensity can be identified as a function of plate geometry, load extension, maximum deflection and membrane force at the left end:

$$q = \frac{8w_m F}{\sqrt{(2Lb-b^2)^2 + (4w_m b)^2}} \qquad \text{Eq. (2-6)}$$

Elastic Behaviour

The membrane force at any location can be derived from the following formula:

$$F = \frac{Et\varepsilon}{1-\nu^2} \qquad \text{Eq. (2-7)}$$

and,

E = Young's modulus of the steel plate

ε = Strain in the normal direction of the plate cross section

ν = Elastic Poisson's ratio

To calculate the strain at any section, the elongation along the plate should be divided by the initial length of the plate. The elongation at the middle of the plate can be defined as a function of the slope along the length of the plate by Eq. 2-8, as follows:

$$\Delta l = \int_0^{\frac{L}{2}} \left[\sqrt{1 + \left(\frac{dw}{dx}\right)^2} - 1 \right] dx \qquad \text{Eq. (2-8)}$$

By using Eq. 2-1, 2-2 and 2-5, the slope in Region 1 and 2 will be:

In Region 1:

$$\frac{dw}{dx} = \frac{4w_m}{2L-b} \qquad \text{Eq. (2-9)}$$

In Region 2:

$$\frac{dw}{dx} = \frac{4w_m}{b(2L-b)}(L-2x) \qquad \text{Eq. (2-10)}$$

Now, by solving the integration formula based on Eqs. 2-9 and 2-10, the total elongation of the plate at the middle can be found. If it is assumed that the strain is uniform along the length of the plate, the mean value of the normal strain can be defined as a function of the maximum deflection (Eq. 2-11).

$$\varepsilon = -1 + \frac{2L-b}{2L}\sqrt{1+U^2} + \frac{b}{2UL} ln\left(U + \sqrt{1+U^2}\right) \qquad \text{Eq. (2-11)}$$

where

$$U = \frac{4w_m}{2L-b} \qquad \text{Eq. (2-12)}$$

It should be noted that for small deflections, Eq. 2-8 can be simplified to a shorter equation (Timosheko, 1959). However, Eq. 2-11 is the exact solution to Eq. 2-8 and can be used for both small and large deflections.

By combining Eq. 2-6, Eq. 2-7, Eq. 2-11 and Eq. 2-12, the load-maximum deflection relationship in the elastic region can be found as follows:

$$q = \frac{UEt(2L-b)}{bL(1-\nu^2)} - \frac{2UEt}{b(1-\nu^2)\sqrt{1+U^2}} + \frac{Et}{L(1-\nu^2)\sqrt{1+U^2}} ln\left|U + \sqrt{1+U^2}\right| \qquad \text{(Eq.2-13)}$$

Plastic Behaviour

Employing the maximum principal strain theory (Ratzlaff and Kennedy, 1985), the yielding occurs when the stress reaches:

$$\frac{\sigma_{yield}}{1-\nu^2} \qquad \text{(Eq. 2-14)}$$

where

σ_{yield} = The yield stress value of the plate material

If it is assumed that the plate material is elastic-perfectly plastic steel, the maximum membrane force, F_m, will establish when the first point on the plate field reaches the yield point and its value can be determined by Eq. 2-15 as follows:

$$F_m = \frac{\sigma_{yield} t}{1 - \nu^2} \qquad \text{(Eq. 2-15)}$$

Substituting F_m in Eq. 2-6, the equation for load-deflection beyond the yield point will be:

$$q = \frac{2U\sigma_{yield} t}{b(1 - \nu^2)\sqrt{1 + U^2}} \qquad \text{(Eq. 2-16)}$$

The general behaviour of the plate predicted by Eq. 2-13 and Eq. 2-16 includes the membrane effect only and does not model strain hardening in the plastic region. Taking the strain hardening into account, the maximum membrane force can grow to higher values than given by Eq. 2-15 and the load capacity will be higher than the load estimated by Eq. 2-16. It is possible to consider the strain hardening effect for bilinear stress-strain behaviour but adding this effect will make the governing equations more complex (Kozarski, 2005).

The other assumption made in the previous formulae is the use of a constant value for Poisson's ratios for both elastic and plastic behaviours. However, when the plastic state is distributed in the plate, Poisson's ratio gradually changes to a plastic value. In this study, the constant value of 0.5 is used for plastic Poisson's ratio; however, Stang et al. (1946) developed an expression for Poisson's ratio in the plastic range as a function of the deflection and strain level. This expression can be used to make the estimation more accurate, but this makes the governing equation more complex. As noted by Ratzlaff and Kennedy (1985), substituting plastic Poisson's ratio in previous relationships will provide an "upper limit" for plate behaviour in the plastic region (Eq. 2-17):

$$q = \frac{2U\sigma_{yield} t}{b(1 - \nu_p{}^2)\sqrt{1 + U^2}} \qquad \text{(Eq. 2-17)}$$

Figure 2-8 presents the pressure and strain level in a steel plate with the properties summarized in Table 2-4. The pressure and strain level are functions of maximum deflection in the plate field that are derived from Equations 2-1, 2-3, 2-4 and 2-5.

Table 2-4. The properties of the sample steel plate

Item	Value	Unit
Length (L)	400	mm
Thickness (t)	3	mm
Yield Stress (σ_{yield})	235	MPa
Elastic Modulus (E)	207	GPa
Elastic Poisson's ratio (ν)	0.3	-
Plastic Poisson's ratio (νp)	0.5	-
Load extension (b)	100	mm

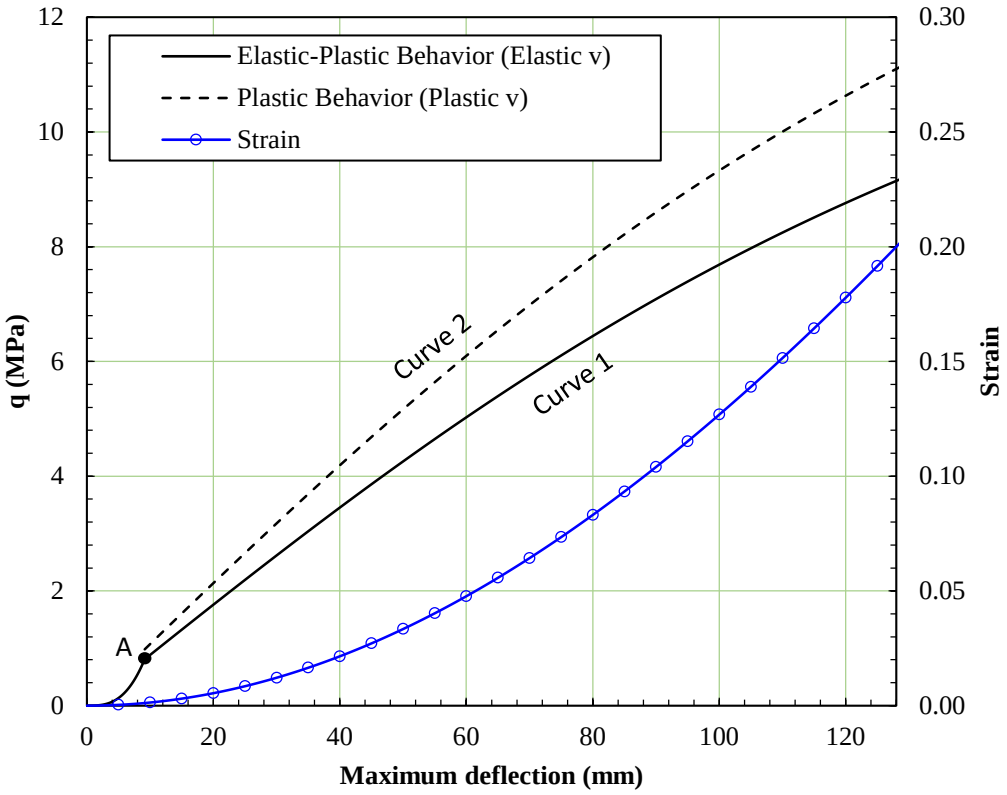

Figure 2-8. Pressure and Strain vs. maximum deflection curve.

In Figure 2-8, Curve 1 shows the plate behaviour in elastic and plastic regions while the Poisson's ratio has a constant value equal to 0.3. Above this curve, the "upper limit" of the plastic behaviour (dashed line) represents the plate behaviour with the plastic Poisson's ratio equal to 0.5 (Ratzlaff and Kennedy, 1985). Point A shows the yield initiation and beyond that point, the load-deflection relationship will follow an almost linear curve. It is expected that the plate behaviour under an actual load would be between Curve 1 and Curve 2. In large deflections the plate behaviour would rise above Curve 2. The reason for this difference is the assumption in the material modeling. In the theoretical solution, it is assumed that the steel material behaviour is elastic-perfectly plastic, and the strain hardening effect is neglected in driving the governing equations.

In Table 2-5, the summary of material properties and geometrical scantling of the test plates are presented.

Table 2-5. Summary of test plate mechanical properties and the geometrical scantling

Thickness	3.175 mm (1/8”)	6.350 mm (1/4”)
Steel Grade	A	EH 40
Yield Point	235 MPa	420 MPa
Young’s Modulus	203 GPa	
Poisson’s ratio	0.3	
Plastic Poisson’s ratio	0.5	
Load extension	100 mm	
Plate width	100 mm	

By using a critical strain of 0.2, the theoretical solution predicts the fracture onset at a critical load in the range of 9.12-11.07 MPa at 127.5 mm of displacement.

The preceding theoretical solution is used to predict the plate behaviour. The results are presented in Figures 2-9 and 2-10. According to the theoretical solution, the fracture initiates after about 159 mm and 161 mm of indentation in the thin and thick plates, respectively. The lateral load at the fracture onset is predicted to be in the range of 93-113 kN for the thin plate and 311-378 kN for the thick plate.

In the next section, the result of the theoretical solution is compared with Finite Element Analysis.

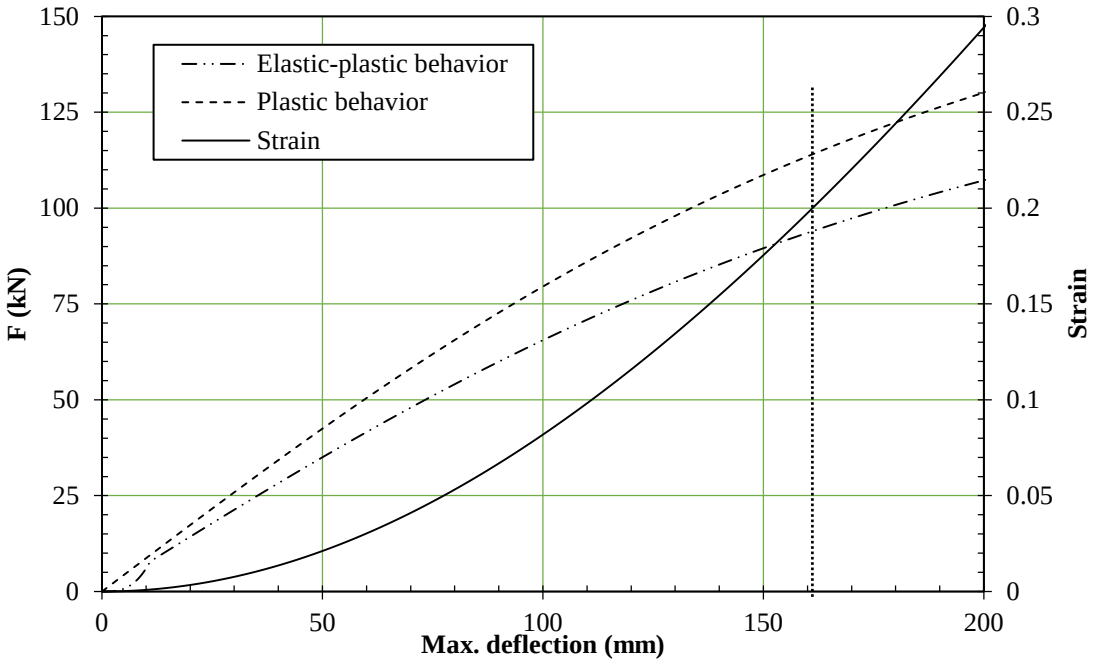

Figure 2-9. Theoretical results for the behaviour of the thin plate – dotted vertical line shows the predicted fracture onset point

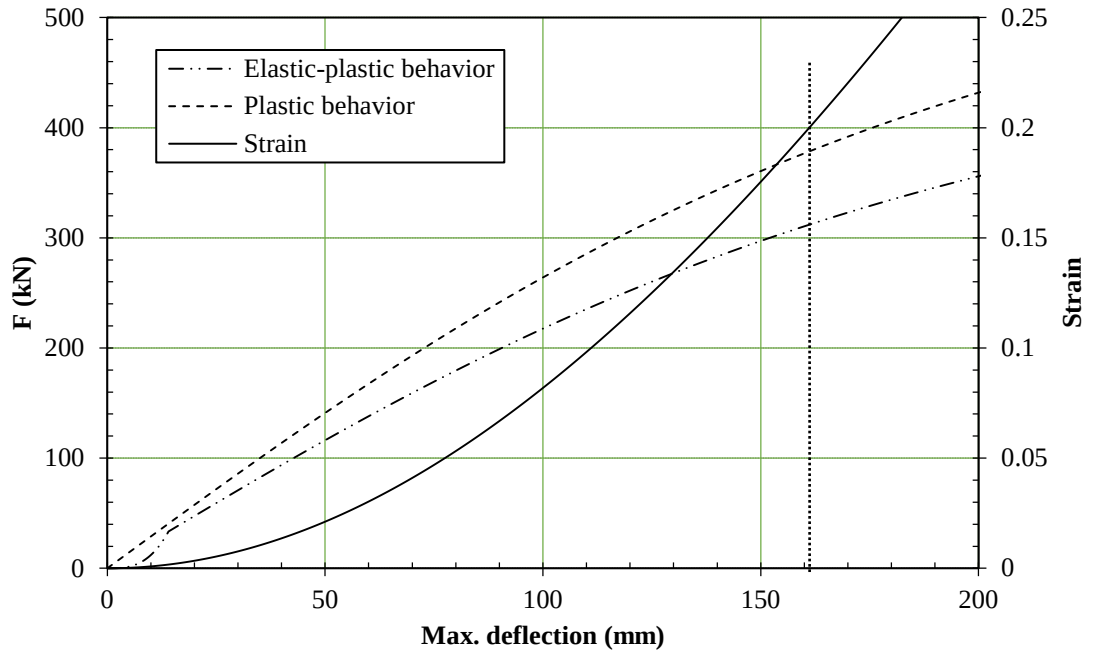

Figure 2-10. Theoretical results for the behaviour of the thick plate – dotted vertical line shows the predicted fracture onset point

2.3 Finite Element Analysis

In addition to the theoretical estimation, Finite Element Analysis of the test setup is conducted to evaluate the theoretical calculation's estimate of the load level in the supporting frame. In this section, the final results of FEA are introduced in order to define the supporting frame scantlings. In Chapter 3, the numerical analysis is explained in more detail.

In FEA, the mechanical properties of the materials are defined based on steel mill certificates for the supporting frame and test plates. In Figure 2-11, the final FEA model is shown.

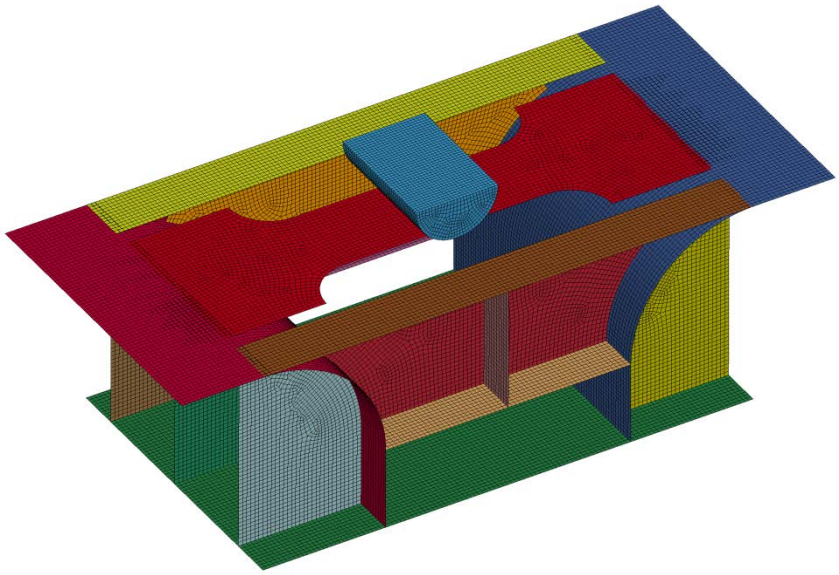

Figure 2-11. The layout of the FE Model of the test setup

The scantling of the final test setup is presented in Figure 2-12 as follows.

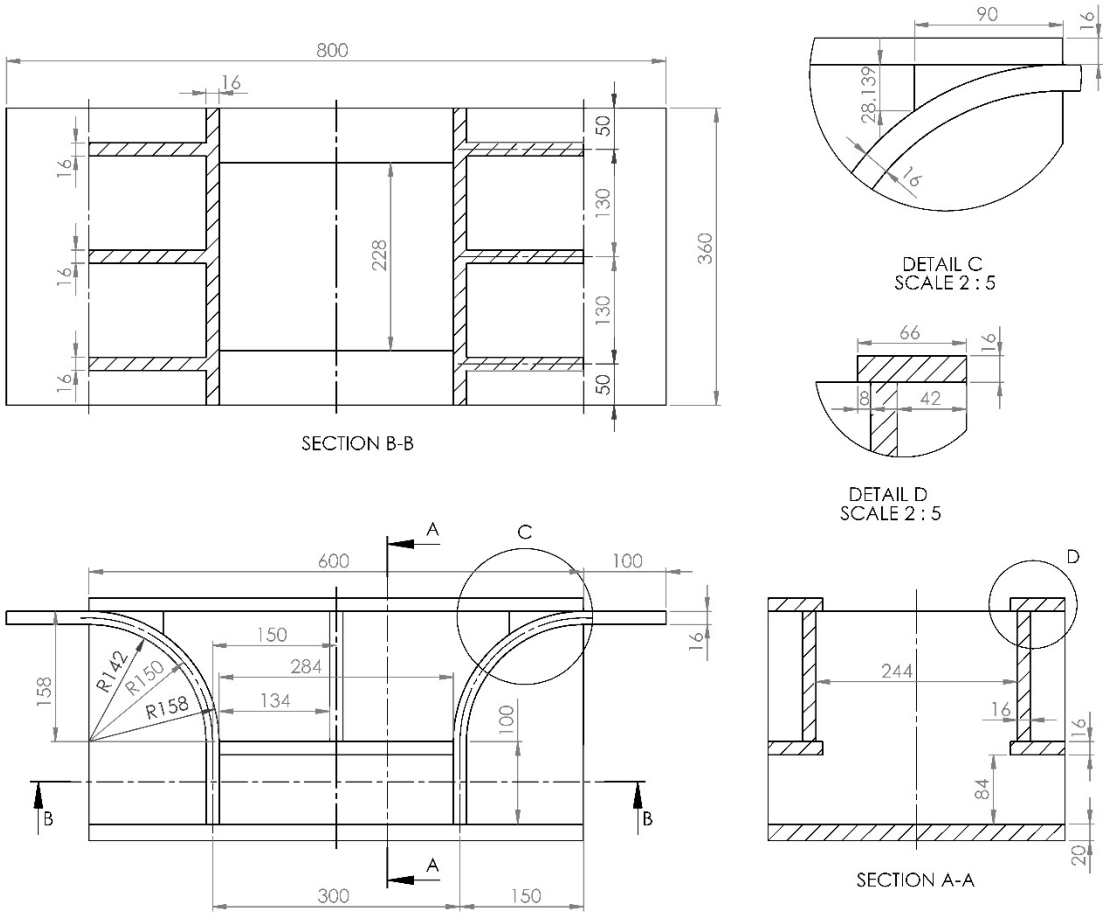

Figure 2-12. The scantling of the designed test setup based on FEA and theoretical calculations

The results of FEA for the prediction of fracture initiation in the test plates are presented in Figures 2-13 and 2-14 for the thin and thick plates, respectively. As can be seen, the FEA predicts fracture onset at 124 mm and 118 mm of displacement in the thin and thick plates at the load level of 108 kN and 333 kN, respectively.

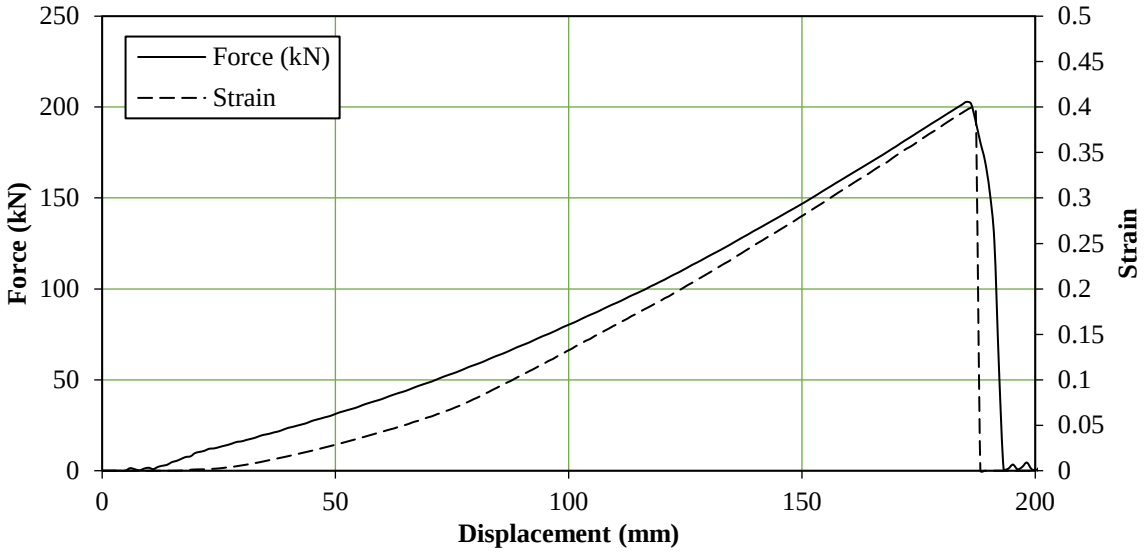

Figure 2-13. The result of FEA for the thin plate

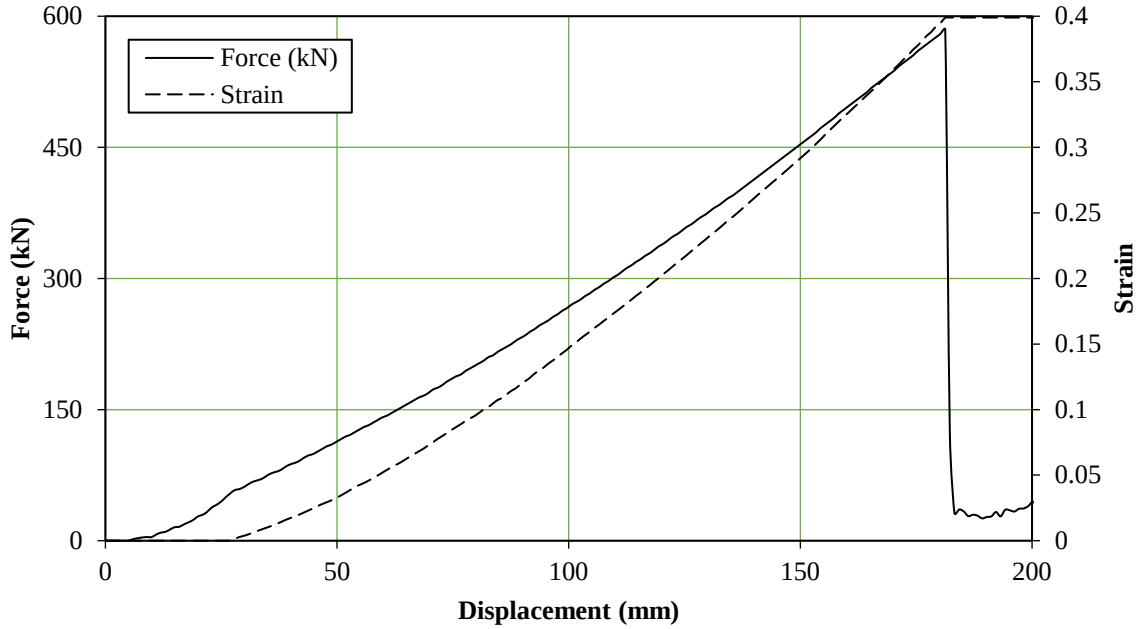

Figure 2-14. The result of FEA for the thick plate

Comparing the results of FEA and theoretical analysis reveals that the maximum load level at rupture is within the specified range using theoretical analysis. However, the maximum displacement estimated by FEA is lower than the estimated value using theoretical analysis.

This difference is related to the difference in material modeling between the two methods. In theoretical analysis, an elastic-perfectly plastic material represents the test plates; in FEA, the stress-strain behaviour is modeled by a bilinear curve that considers the strain hardening effect. Therefore, in FEA a higher load level is reached at a lower displacement.

2.4 Fabrication of the Test Setup

The whole test assembly was fabricated at Technical Services of Memorial University of Newfoundland. The maximum capacity of the bend machine and other available facilities were considered in the final design. Upon finishing the design of the test setup, the shop drawings were prepared to evaluate the type and dimension of the required materials for the fabrication. The shop drawings were also needed for accurate cutting, drilling, bending, welding and threading of the components with the Waterjet and CNC machines. The shop drawings used in the fabrication of the test assembly are presented in Appendix 2.

The test assembly was constructed from two different plate thicknesses, as presented in Table 2-1. Steel plates with the thickness of 5/8 and 3/4 inches were used for the boundaries of the assembly. The cutting layouts of the boundary steel plates are presented in Figure 2-15 and 2-16.

In Figure 2-15, the two components labelled with “F” were bent to the designed radius, as shown in Figure 2-12, to form the curved boundaries of the supporting frame. This was accomplished with sequential cold bending using the bending machine and the process was monitored to avoid cracking on the plate. The slight line marks on the plate as shown in Figure 2-17 are the result of the sequential bending.

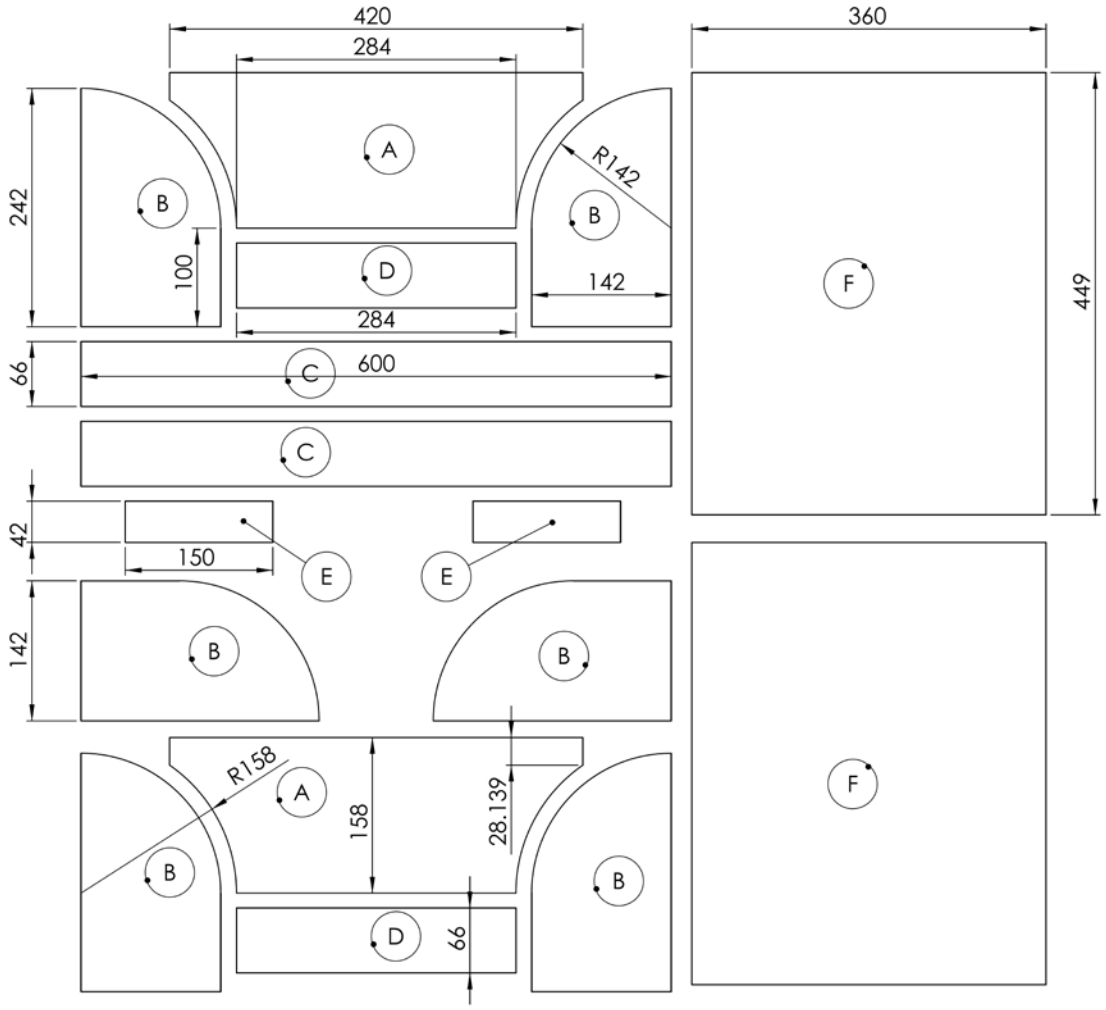

Figure 2-15. Cutting layout of the test setup assembly

Shielded Metal Arc Welding (SMAW) was used to weld the joints. In doing so, appropriate edge preparation of the weld joints was controlled prior to the welding. Additionally, preheating, for the control of interpass temperature and cleanness and dryness of the welding electrodes, was conducted to avoid the weld defects and delayed hydrogen cracking that are common defects in high strength steels. The final welded structure was visually inspected to detect and repair any weld defects.

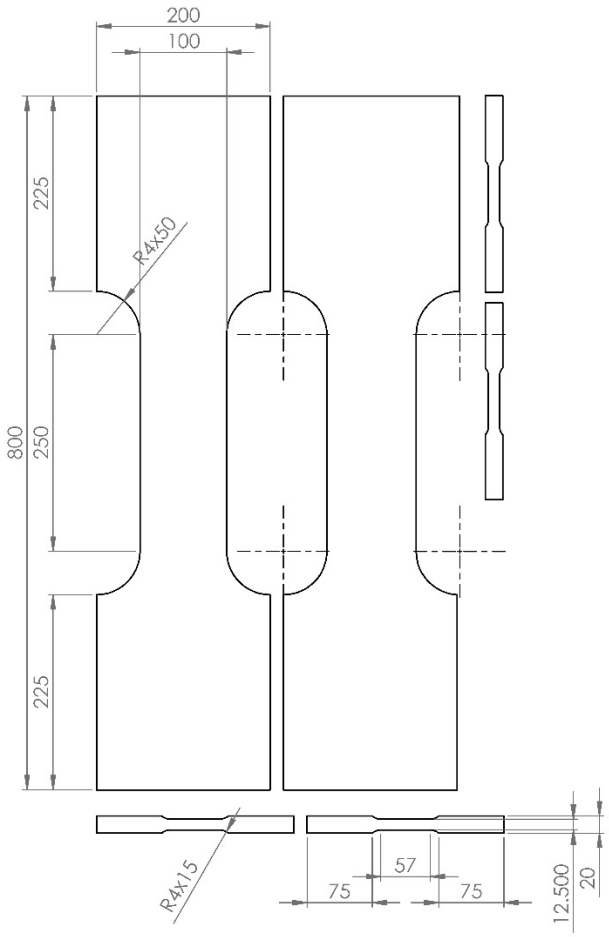

Figure 2-16. The cutting layout of test plates

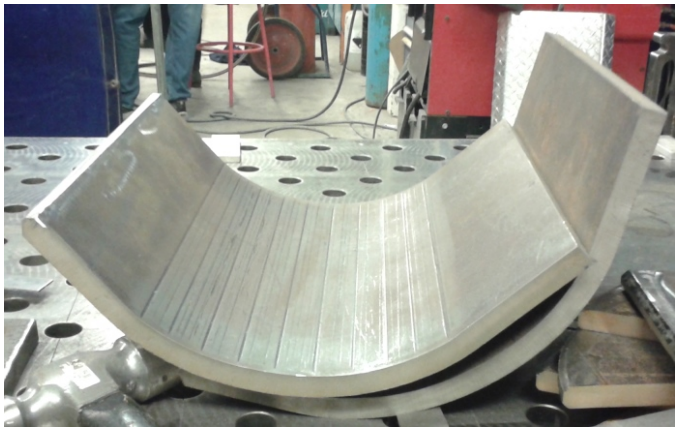

Figure 2-17. The curved members of the test setup after bending

Upon completion of welding, the supporting frame was machined to drill bolt holes and keyway slots. The drilling and cutting were conducted by a CNC machine.

Figure 2-18. The supporting frame and one test plate after machining process

The design of the indenter assembly was explained in Section 2-2. Different components of the indenter were fabricated according to the design scantling. The only variation between the initial design and the final fabrication is the use of an adapter for the stud where it penetrates into the indenter head. This adapter is shown in Figure 2-19. The main reason for installing this adapter is to decrease the diameter of the drilled hole in the indenter head to avoid its collapse (especially in the case of the plastic indenter). The CNC machine was used to drill the hole in the indenter heads and also thread the drilled hole in which to fit the indenter stud in. Figure 2-20 shows the final prepared indenter head after machining.

Figure 2-19. The adapter bolt

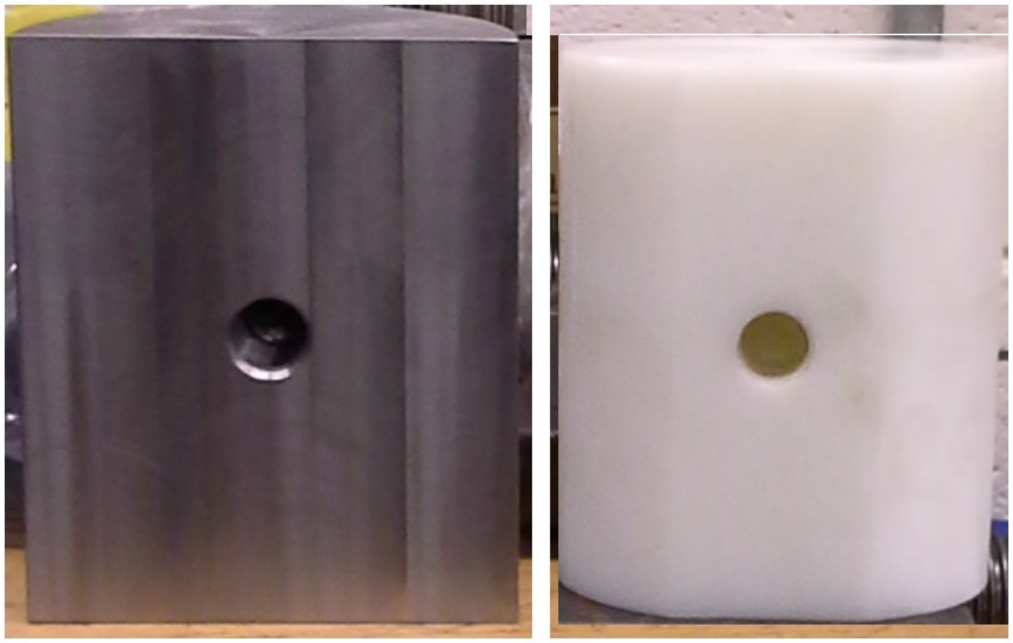

Figure 2-20. The top view of steel and plastic indenter heads

Chapter 3: Numerical Analysis

3.1 Introduction

The LS-DYNA finite element program, an appropriate tool for the analysis of nonlinear problems, is used for the numerical analyses. For the modeling and post processing of the results, the LS-PrePost program is used.

The geometry, scantling, and arrangement of the supporting frame, the test plates and the indenter are presented in Chapter 2. Several finite element models were analyzed to design the final test setup to simulate fracture onset at the middle part of the test plate. Initially, a box shaped supporting frame was designed for the test setup. In that design, the boundary plate edges were sharp and the test plate was lying over the supporting frame, similar to a stiffened panel (Figure 1-3). The eccentricity of the end bending moments resulted in the fracture onset close to the plate ends (Ratzlaff and Kennedy, 1985). Therefore, the test design was modified and the curved boundary plates were used for the supporting frame. The radius of the curved boundary plates and the width of the test setup were defined considering the geometrical limitations of the test machine, the capacity and capabilities of the bending machine intended to be used for fabrication of the support frame, and the location of the first failure in the plate field. Figures 1-6 and 2-3 in the previous chapter present the final arrangement of the supporting frame. The scantling of the test plate profile was defined by FE analysis.

3.2 Material Properties

In the design stage, the mechanical properties of the test plates were determined with reference to steel mill certificates. Upon availability of the test materials, a series of experiments on standard coupon samples was completed. For further details, refer to Seif

T., 2014. In Table 3-1, the summary of mechanical properties of the test plates based on tensile tests is presented.

Table 3-1. Summary of the mechanical properties of test plates after the tensile test

Item	Tensile Strength	Yield Strength	Young's Modulus	Poisson's Ratio
Thick plate	715 MPa	426 MPa	202 GPa	0.3
Thin plate	475 MPa	244 MPa	214 GPa	0.3

The material properties of the supporting frame were determined in accordance with the minimum requirements of ABS Rules for Testing and Certification of Materials. The equivalent grade in ABS Rules is Grade AH32, with the mechanical properties presented in Table 3-2. Note that according to mill certificates for the supporting frame materials, yield and tensile strengths of the plates were higher than the above mentioned minimum rule requirements.

Table 3-2. The mechanical properties of the supporting frame and the indenter head.

Item	Tensile Strength	Yield Strength	Poisson's Ratio	Elongation
Boundary plates	440 MPa	315 MPa	0.3	22 %
Indenter head	400 MPa	235 MPa	0.3	22 %

The arrangement of the indenter assembly on the test machine is explained in Chapter 2. In the finite element analysis, for modeling the contact between the indenter and test plate, only the indenter head with a semi-cylindrical profile is modeled. The material properties of the indenter head are summarized in Table. 3-2.

3.3 FEA Model: Geometry, Modeling, and Mesh

The geometry of the test setup is modeled using the LS-PrePost software program. The "Geometry" and "Surface" tools of the LS-PrePost software are used to create the initial geometry of the model. Figure 3-1 presents the three-view geometry of the initial model created in LS-PrePost.

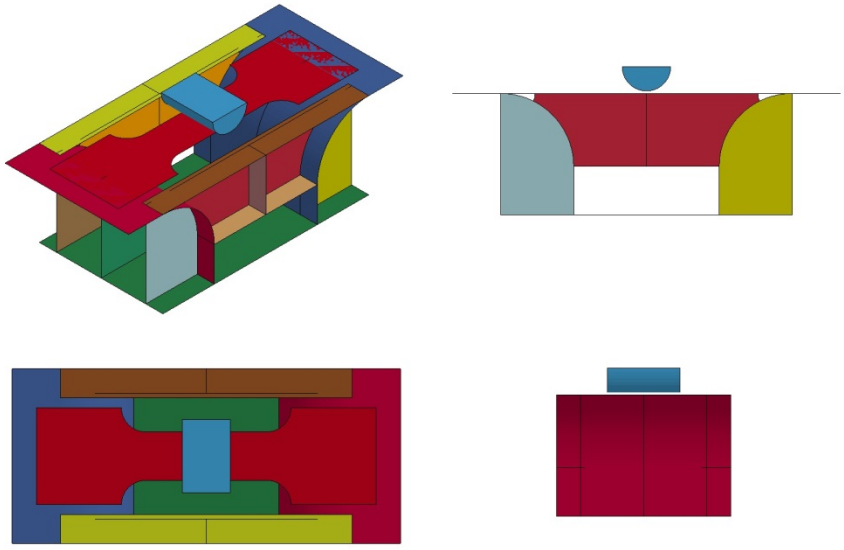

Figure 3-1. The layout of the test setup model in LS-PrePost

Later, the "Mesh" tool was used to apply mesh on the geometry using the "Auto Mesh" capability of LS-PrePost and the manual mesh generation option. To create the mesh manually on surfaces with special layouts such as the test plate, "2D Mesh generation" and "Element Generation" tools of the software were used to design the appropriate mesh.

Non-rigid shell elements were used to model the test plates. The same shell elements were applied to the supporting frame to assess its rigidity during the indentation experiments.

A mesh convergence study was conducted on the geometrical model to define the mesh size. The optimum mesh size for the analysis of the shell elements was 5 mm. The identification of the model, including the total number of elements and nodes, is summarized in Table 3-3. The final meshed FE model is presented in Figure 3-2.

Table 3-3. Total number of elements and nodes in the final FE model

Item	**No. of elements**
Shell elements	43118
Nodes	55968
Solid elements	10830

During the modeling, the “Element Editing” tool in LS-PrePost software was used to control the quality of the generated mesh. The initial quality control items and the associated values used to evaluation of the elements are summarized in table 3-4. As shown in this table, in the final model, the total number of violated elements is 12 for the minimum quad angle and 15 for the maximum quad angle criteria representing less than 0.035% of the total elements. The final results are presented in table 3-4. This violation was rectified by deleting the unacceptable quad elements and replacing them with new triangular elements.

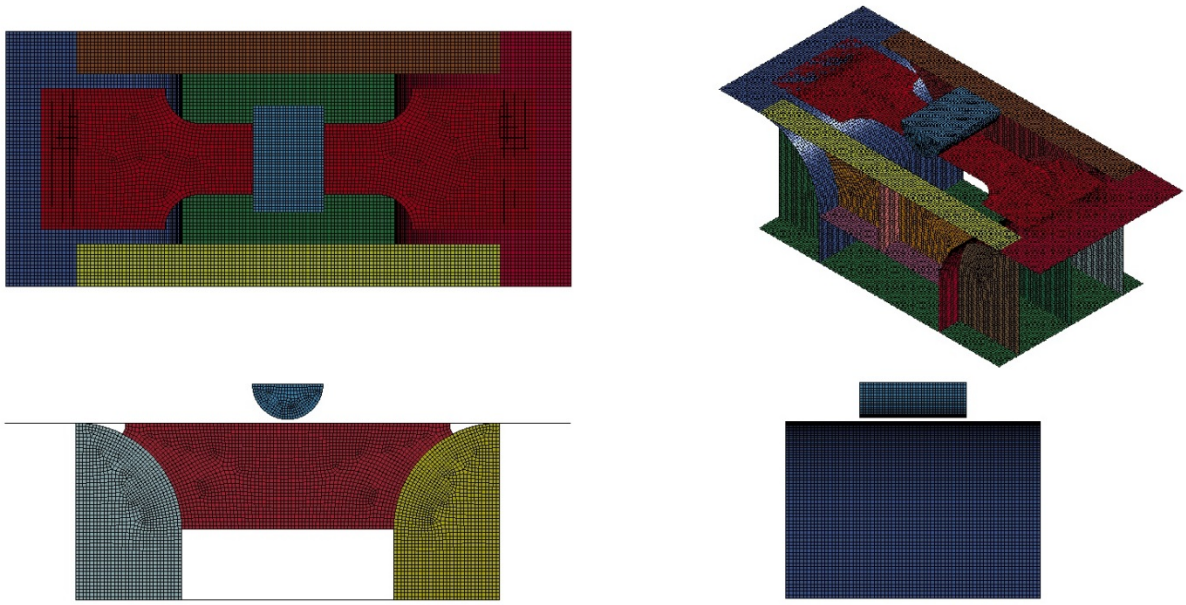

Figure 3-2. The layout of the final FE model

Table 3-4. Shell element quality check summary

Quality Name	Min. val	Max. val	Allowable	#Violated(%)
Max side length	3.38	7.42	10	0 (0%)
Aspect Ratio	1	2.28	4	0 (0%)
Min Quad Angle	39.5	90	45	12(0.0278%)
Max Quad Angle	90	140	135	15(0.0348%)
Taper	0	0.456	0.7	0 (0%)
Skew	0	41	45	0 (0%)

As shown in Figure 3-3, in the experiment, four C- clamps were used at each end to attach the supporting frame to the test machine. Similarly, four node groups were defined at each end of the supporting frame, representing the footprint of the clamps, as shown in Figure 3-4. These node groups are restrained in six degrees of freedom. Another node group was

defined on the upper surface of the indenter head with five degrees of freedom, allowing motion in the vertical direction only (z-axis).

Figure 3-3. The arrangement of C-clamps on the test setup

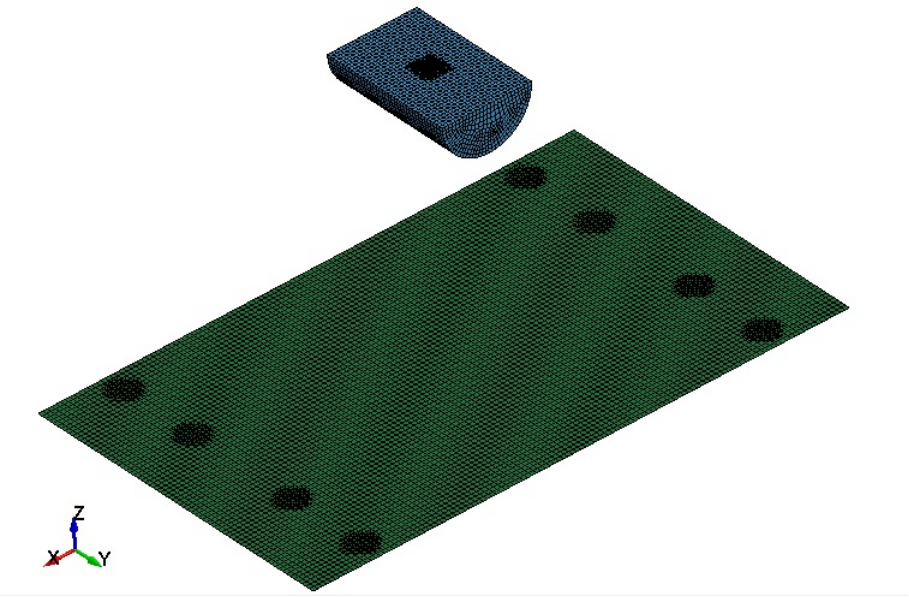

Figure 3-4. Defined boundary conditions on the FEA model (some members are not shown)

3.4 Contact Model

In the FE model, the indentation of the indenter results in an initial contact between the rigid indenter and the test plate and with contact progress, another contact between the test plate and the curved boundaries of the support frame at both ends of the test plate. Therefore, in total, there are three contact models in the final analysis.

The first contact between the indenter and test plate is modeled by using a one way contact (One-Way-Surface-to-Surface) between the solid elements (the rigid indenter) and shell elements (the test plates). In this case, since it is assumed that the indenter head is a rigid material and only the analysis of the test plate is intended, a one-way contact mechanism is used.

The contact between the test plate and the supporting frame is simulated by an automatic two way contact model (Automatic-Surface-to-Surface). The automatic contact model provides the capability to define the initial penetrations between the contact surfaces as the baseline for the analysis.

The initial penetration of the indenter into the test plate is avoided by defining an initial gap of 10 mm between them. This method is used in modeling the contact between indenter and plate (Figure 3-5). Due to the geometry of the supporting frame, the test plate should lie on top of the curved boundary plates with bonded edges, as shown in Figure 3-6.

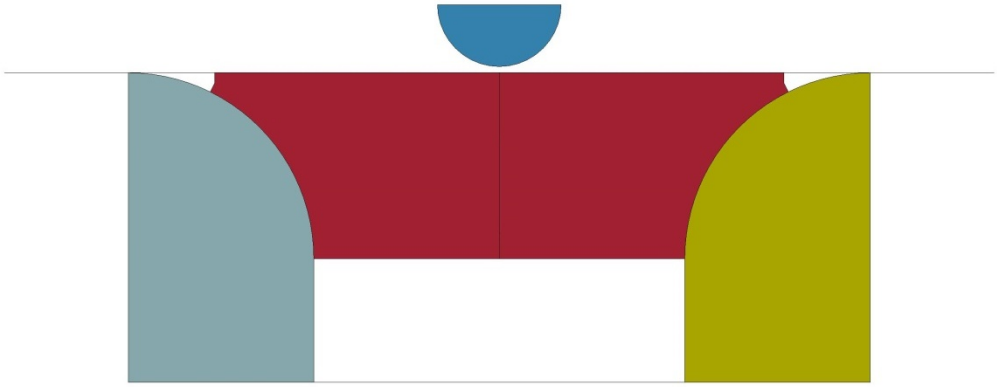

Figure 3-5. Side view of test frame showing the initial offset.

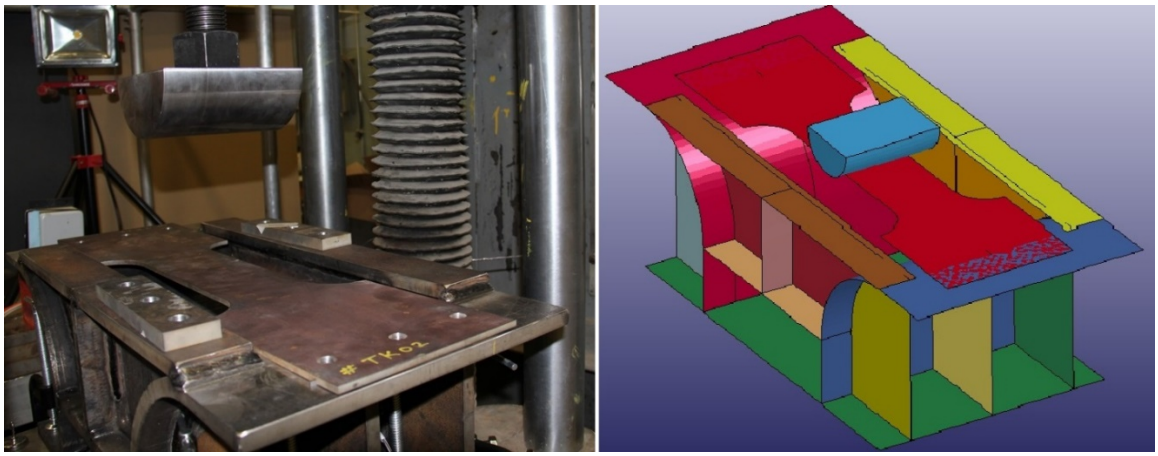

Figure 3-6. Layout of test supporting frame

LS-Dyna provides a keyword card in contact modeling (IGNORE) that enables definition of the initial penetration as the baseline for analysis. This parameter is used in the contact model between the plate and curved boundaries. The effect of this parameter is studied by comparing the analysis results between two models. An abrupt change in negative contact energy shows the effect of initial interpenetration. Therefore, appropriate keyword values are defined in the model to provide the contact energy for each contact in the model. This is achieved by defining the keyword *DATABASE-SLEOUT in the model. Figure 3-7

presents contact energy curves for the contact between the test plate and supporting frame with the active IGNORE card. The IGNORE card eliminated the effect of the initial penetration.

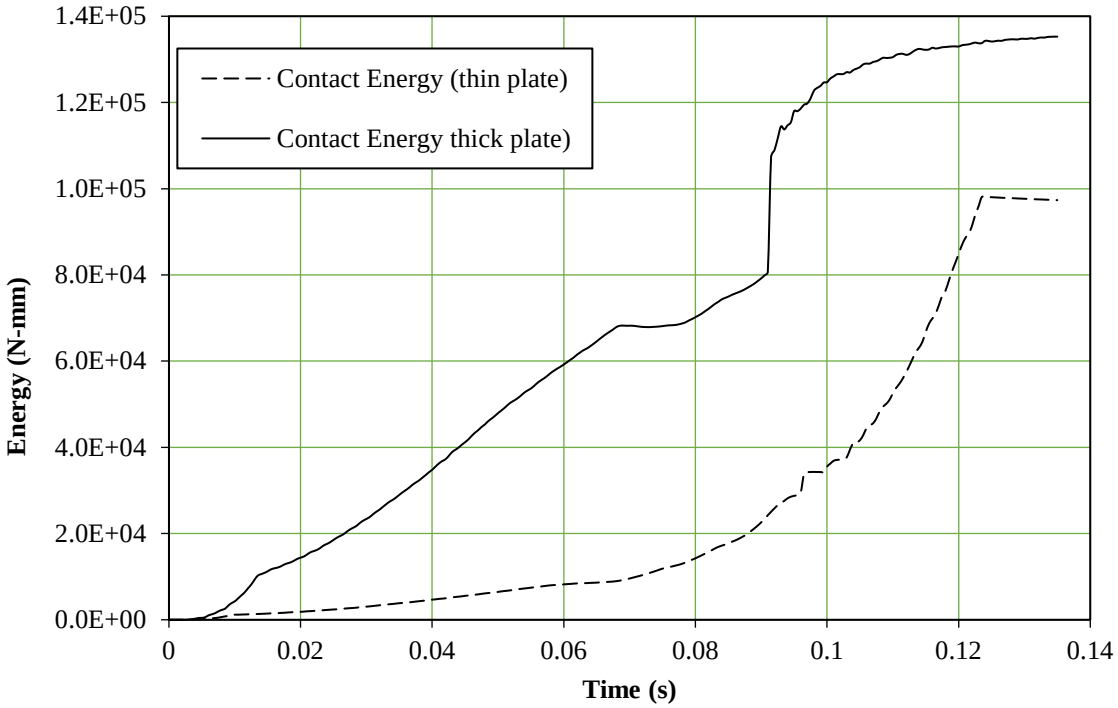

Figure 3-7. Contact energy: the contact model with the effect of the IGNORE card for the thin and thick plate.

In addition to this approach, a mesh refining study was also performed to define an optimum refined mesh size. It is recommended by the LS-DYNA theory manual to define a consistent mesh size on adjacent contact parts in order to avoid penetration problems. In the final model, the mesh size of 5 mm was selected for both test plate and curved boundary plates of the supporting frame.

As recommended in the LS-DYNA theory manual, the default parameters for the contact modeling of similar materials with similar mesh size provide outputs with reasonable

accuracy. Therefore, the contact between the rigid indenter and steel plate was modeled by using default parameters. For the contact between the HDPE indenter head and the test plate, the dissimilarity of the contact materials will lead to instability in the analysis. To avoid this problem, the SOFT parameter in contact modeling is used to simulate the contact between the plastic indenter and the steel test plate. The SOFT parameter utilizes the soft constraint-based approach to calculate the stiffness of the contact springs in the model. This contact approach is independent of the material constants and is recommended for foam to steel contact.

The indentation rate in the experiment varied between 0.10 – 1.60 mm/s, that is a very low speed with insignificant dynamic effects. In the FEA model, a simulation with real time indentation speed, as noted above, will significantly increase the run time of the analysis. In LS DYNA there are several approaches to decrease the analysis time. Among them, time-scaling and mass-scaling are the common means. In this analysis, time-scaling is used to decrease the total indentation time. Time-scaling involves the application of the load with a speed higher than the real test speed to reduce the simulation time. In this approach, it is important to monitor the kinetic energy level in comparison with the internal energy in the contact model to ascertain that the kinetic energy is negligible. This is to avoid dynamic effects in the analysis due to inertial forces and keep the analysis in quasi-static mode. To monitor the energy data in the contact model, the appropriate output data is called in LS DYNA to provide the energy level during the indentation.

Based on the preceding criteria, a series of analyses with different indentation speeds was simulated and the kinetic energy level was compared to the internal energy. The final

indentation speed for the indenter head in the analysis was equal to 1 m/s. With this indentation speed, the kinetic energy was less than 0.5% of the internal energy in the FEA.

3.5 Failure Criteria and Material Modeling

The shell elements of the support frame and test plate are modelled by "MAT_ PIECEWISE_ LINEAR_ PLASTICITY". This model involves the use of isotropic elasto-plastic material. The stress strain behaviour for this model can be simulated by either a load curve or by introducing a bilinear stress strain curve. The latter is used to simulate the behaviour of the material. The mechanical properties of the steel material used in the analysis are presented in Section 3-2. Figure 3-8 presents the bilinear stress-strain curve for the test plate material.

As described in Chapter 2, a critical strain of 0.2 is considered as the failure criterion. This criterion is simulated by setting the FAIL key value equal to 0.2 in the model properties. This key value eliminates the mesh in the plate field as soon as its strain value reaches the critical strain value. Although this failure criterion does not provide crack propagation in the test specimen, it can be used to estimate the fracture onset location, the maximum lateral indentation of the indenter, and load level at the fracture onset that are the intended outputs in this study.

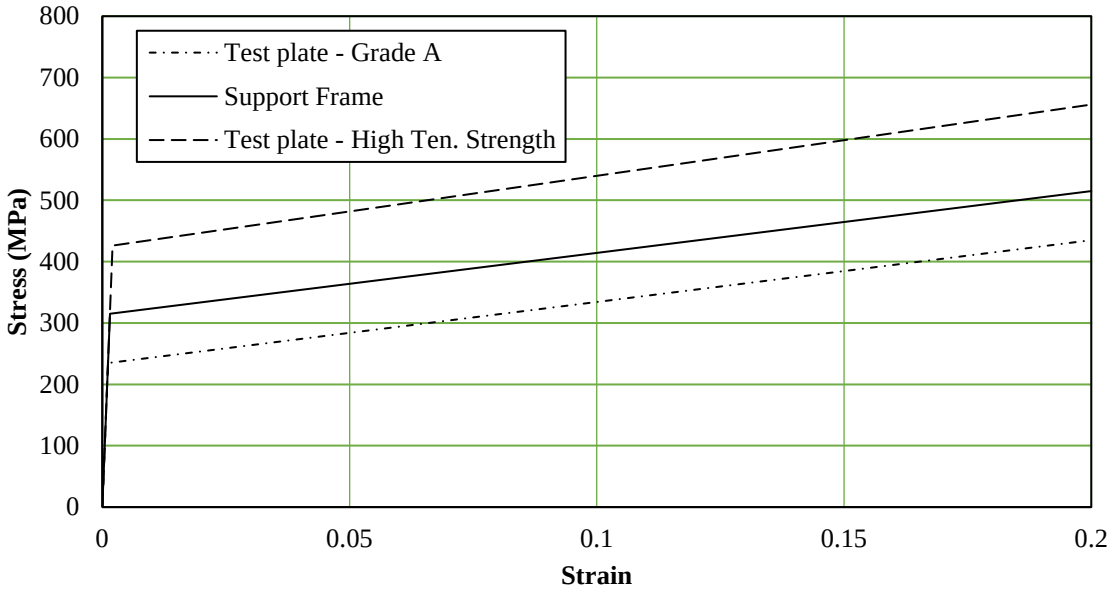

Figure 3-8. Stress-strain behaviour of the material in the FE analysis.

3.6 Finite Element Analysis Results

The final FE models were defined and analyzed with the details as described in the previous sections. In this section, the results of the finite element analysis are presented. The results are provided for thin and thick test specimens separately. Figures 3-9 and 3-10 present the layout of the deflected test specimen at the fracture onset in thick and thin plates respectively.

The location of the fracture onset in the plate field and the lateral force and indentation are summarized in Table 3-5.

Figure 3-9. Deflected thick plate at fracture onset.

Figure 3-10. Deflected thin plate at fracture onset.

Table 3-5. Particulars of fracture onset in the thin and thick plate fields

	Thin Plate	Thick Plate
Distance from the edge in X-dir.	285 mm	323 mm
Lateral indentation	184.3 mm	181.3 mm
Max. VM Stress level	630.4 MPa	891.1 MPa
Total lateral force	201 kN	585 kN

To predict the location of fracture onset, a study of stress distribution is conducted in high stress areas. In Figure 3-11 the Von Mises stress distribution contour is presented in the thin and thick plate fields, in one-time step before the fracture initiation in the plates.

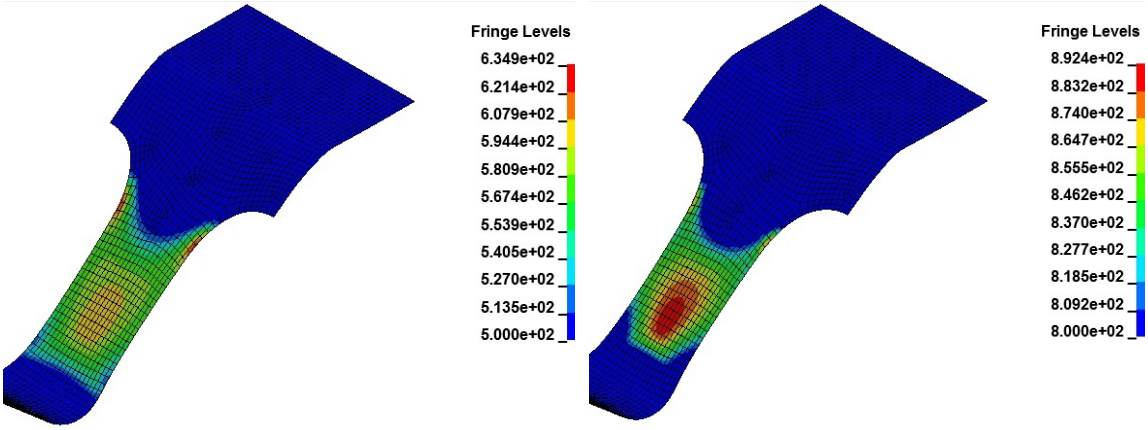

Figure 3-11. Von Mises stress distribution in the thin (left) and thick (right) plate fields (Fringe level in MPa)

The general layout of the stress distribution in the thin and thick plate fields is similar. Detailed review of the stress distribution in the thin and thick plates shows that two high stress areas exist in the plate field. The first area is located approximately 285 mm from the plate end, and the second at approximately 323 mm far from the plate end. The difference in the maximum Von Mises stress level between these areas is less than 4% and 1% for thin and thick test plates, respectively. Figure 3-12 and Figure 3-13 present comparison of Von Misses stress level in the above noted areas in the thin and thick plates, respectively.

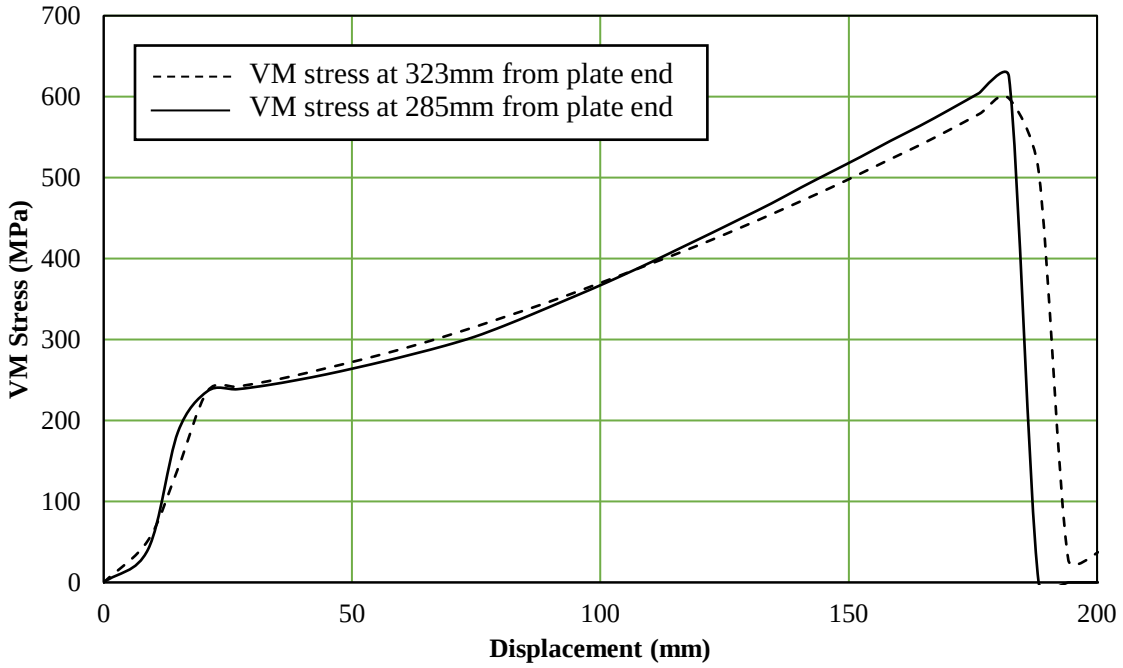

Figure 3-12. Comparison of Von Mises Stress in the thin plate

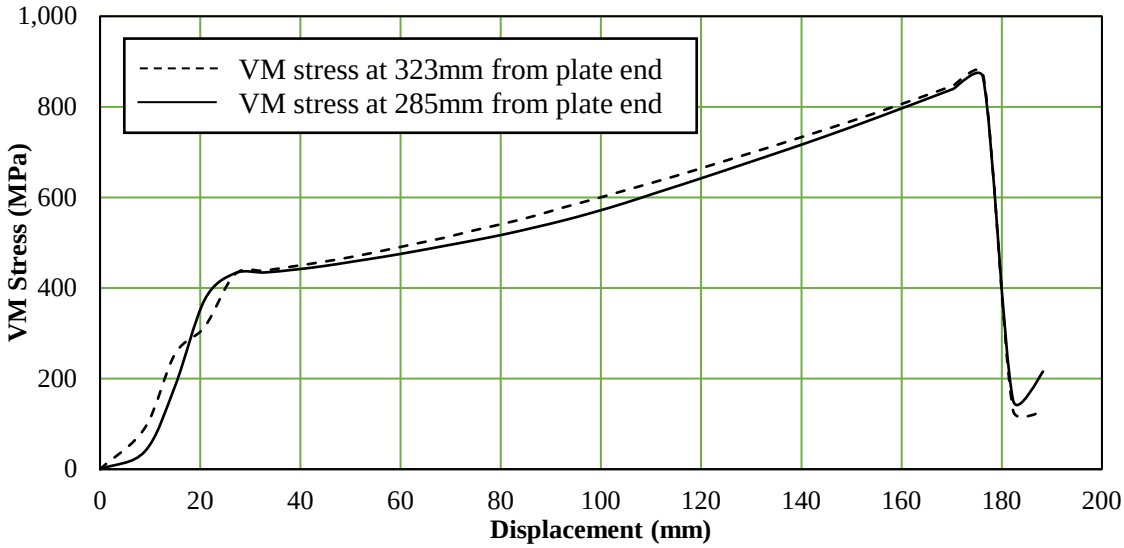

Figure 3-13. Comparison of Von Mises Stress in the thick plate

The strain and VM stress levels in the element with the maximum strain and VM stress are presented in thin and thick plates in Figures 3-14 and 3-15, respectively.

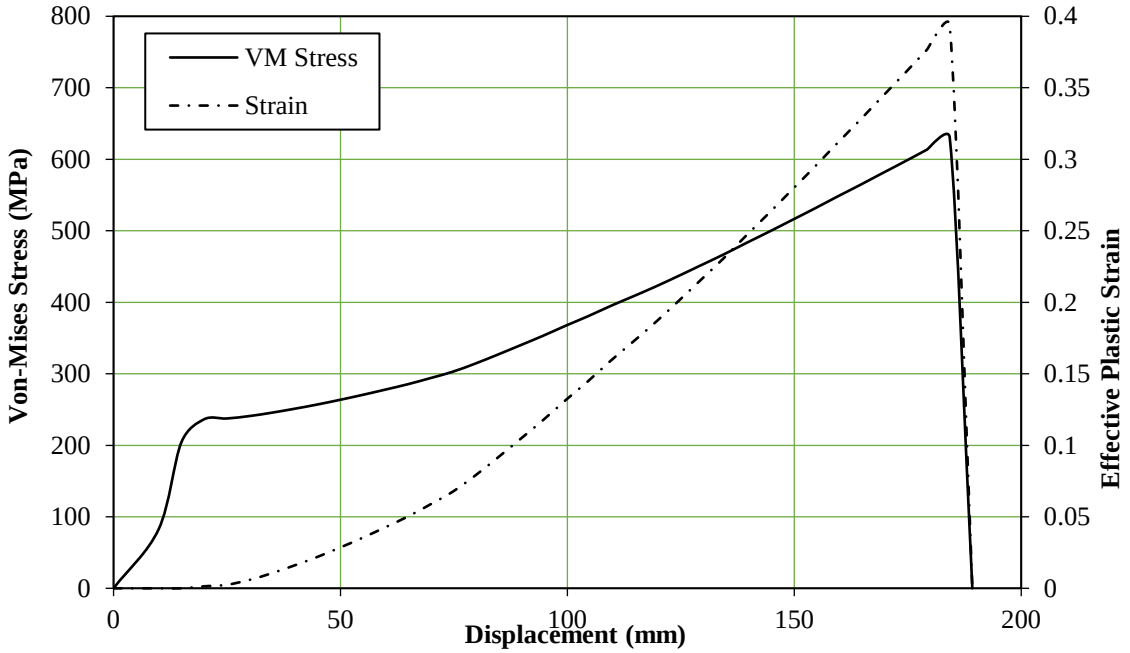

Figure 3-14. Maximum Von Mises Stress and Strain level vs. time in thin plate

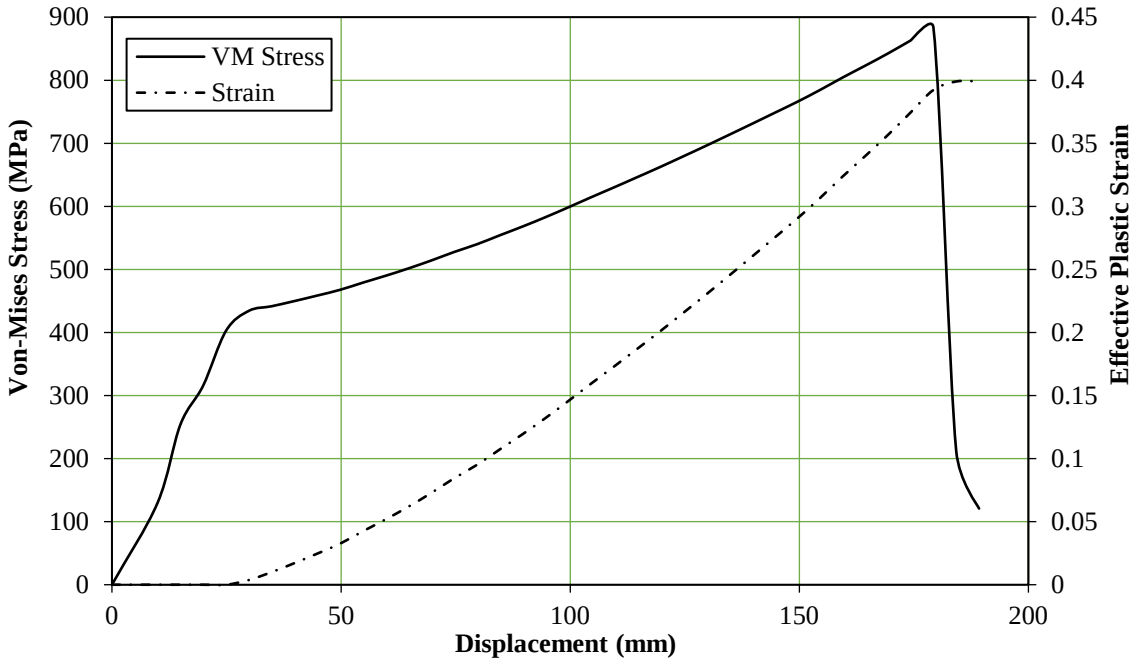

Figure 3-15. Maximum Von Mises Stress and Strain level vs. time in thick plate

Other key parameters in the comparison of the FEA and experiment results are the lateral indentation of the plate and the total force at fracture onset. In Figures 3-16 and 3-17 the total lateral load is presented for thin and thick plates. In Table 3-5, the indentation and total force are listed for each plate.

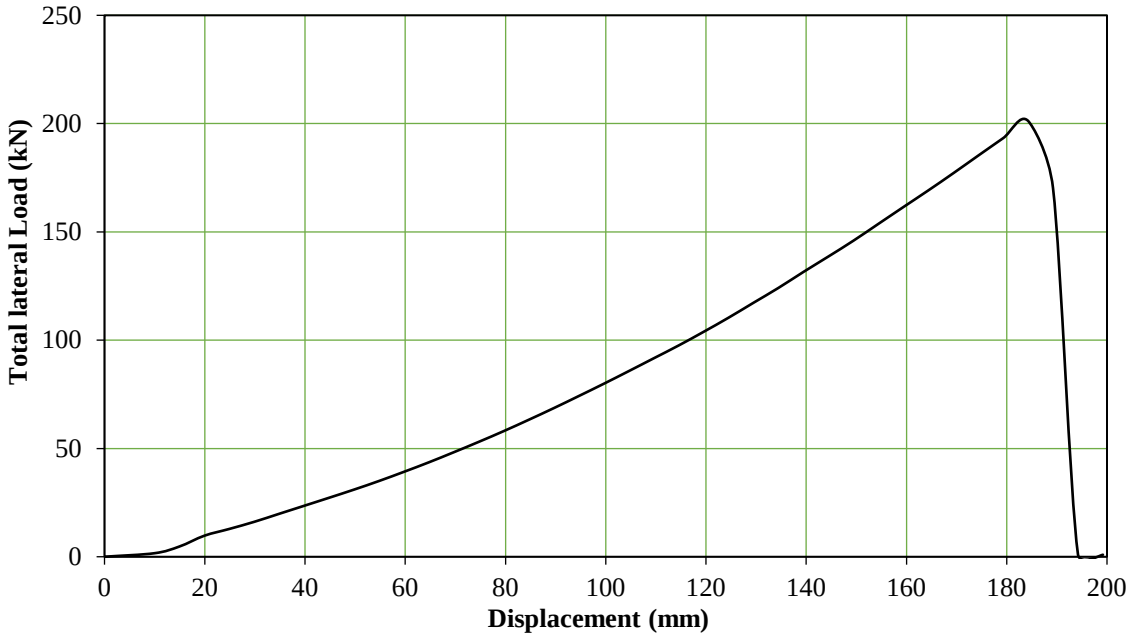

Figure 3-16. Lateral indentation load vs. displacement in thin plate

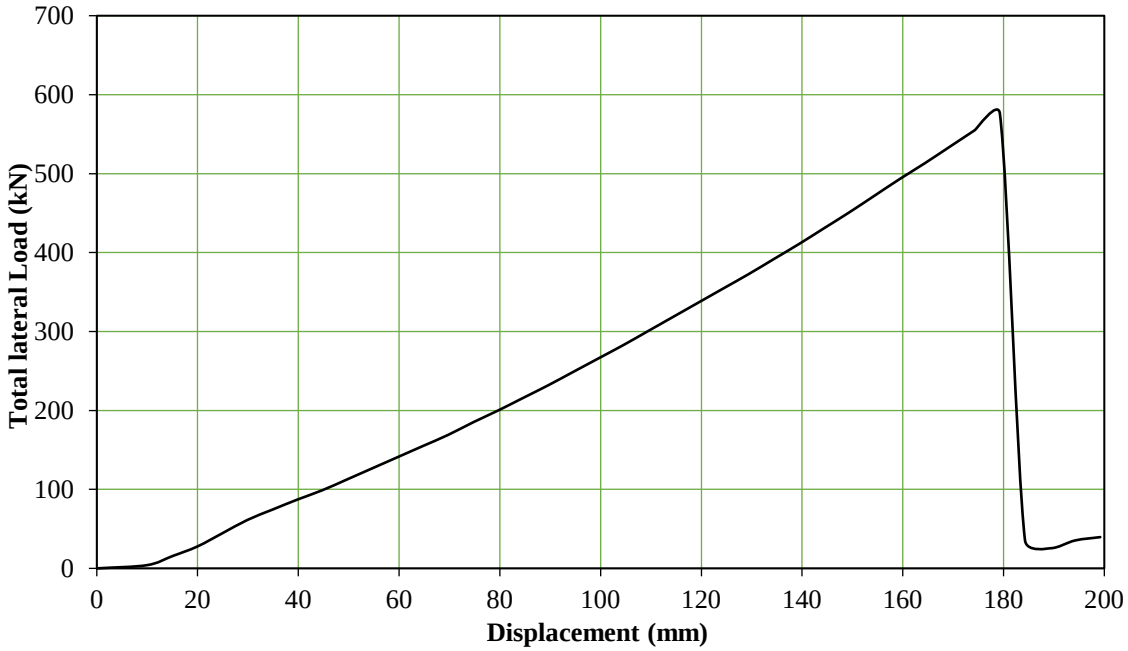

Figure 3-17. Lateral indentation load vs. displacement in thick plate

Chapter 4: Physical Experiment

4.1 Introduction

In Chapter 2, the layout of the test setup was presented. A hydraulic machine is used to apply the lateral indentation to the test plate from the top side. Sensors are connected to the supporting frame, test plate and hydraulic machine to record the applied force, displacement, and strain level in the test setup. A data acquisition system is used to convert the recorded data to digital outputs.

Three video recording cameras are used to monitor the fracture onset and the fracture propagation under the applied load from the upper and lower sides of the test plate.

The final desired results including the load level, location, and displacement at the time of the fracture initiation and the orientation of fracture are extracted from the recorded data. In addition, the strain level data are analyzed to verify the rigidity of the supporting frame during the experiment.

4.2 Installation of test setup

The arrangement of the support frame and the test plate is presented in Figure 4-1.

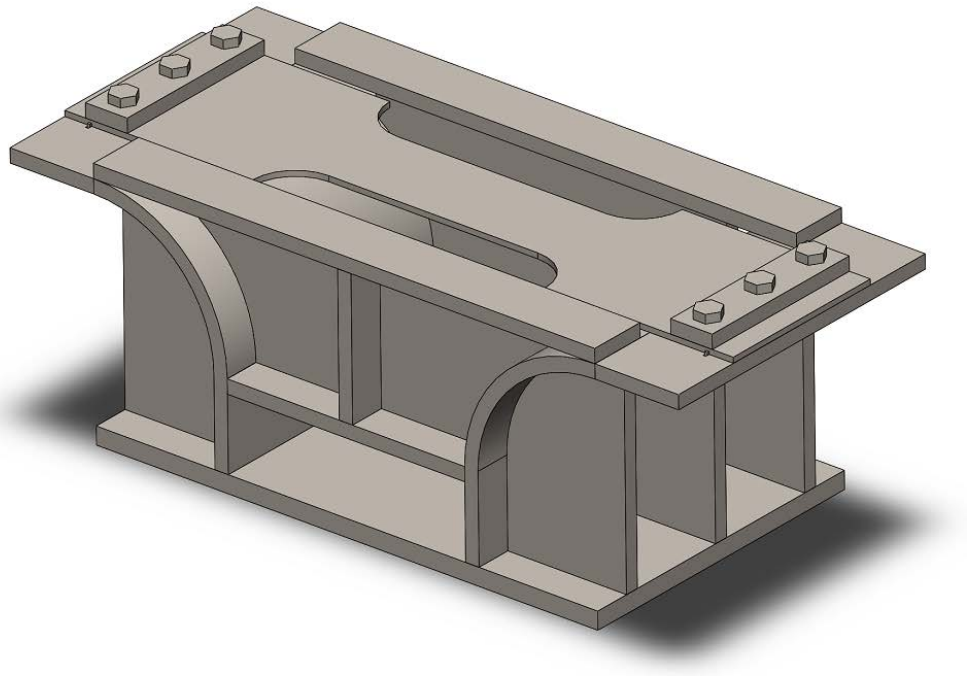

Figure 4-1. The layout of the experiment model

The dimensional limits of the test machine were considered in the design of the test frame in the initial design to ensure the machine could accommodate the supporting frame and indenter during the experiment's progress. Figure 4-2 (repeated from Chapter 2) shows the layout of the test machine. The supporting frame is fitted on top of the bed plate in the area between side bolts (shown with the letter A) and the indenter is connected to the middle crosshead. Four C-clamps are used at each end of the test frame to avoid lateral motion of the test frame on the bed plate. The load is applied by the upward motion of the bed plate against the fixed crosshead. The load cell is connected to the lower side of the bed plate and transmits the data to the data acquisition system. The maximum capacity of the test machine is 1,500 kN with the maximum stroke of 229 mm. Further details related to the test machine are presented in Appendix 3.

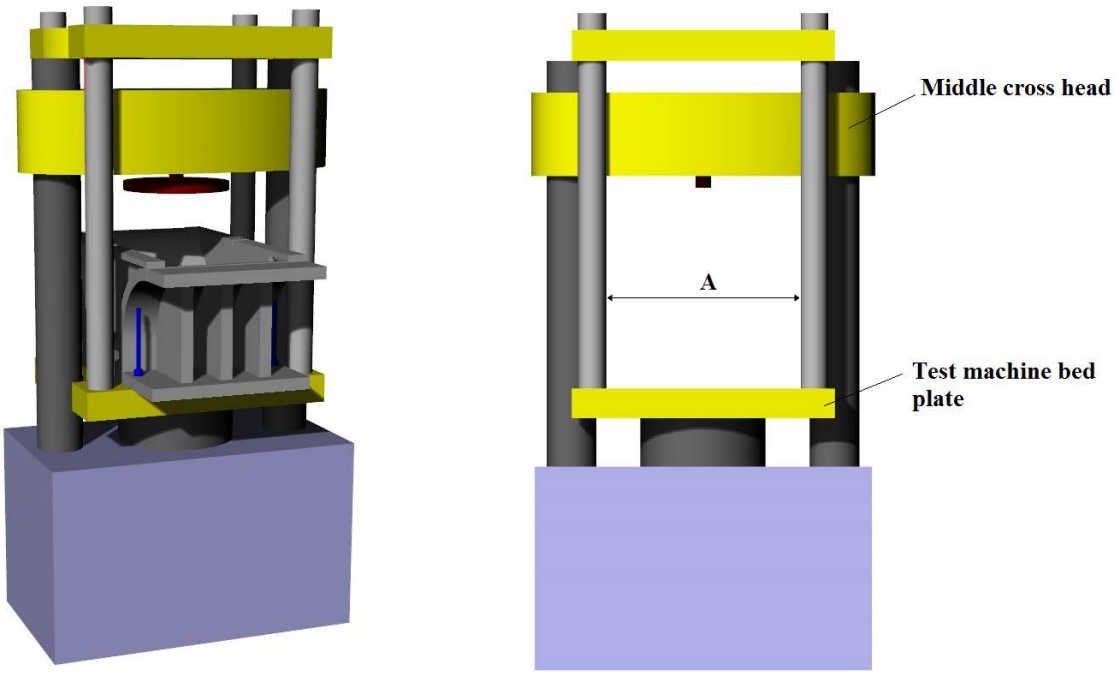

Figure 4-2. The layout of the test machine

The layout of the indenter was shown in Figure 2-5. The indenter head and its connecting rod are passed through the upper and middle crossheads to locate the indenter head on top of the test plate.

4.3.1. Sensors and Recording Devices

Twelve strain gauges (six on each end) are used to monitor the stress level at critical locations of the supporting frame. The locations of the strain gauges are specified with reference to the FEA results and based on the areas with estimated high stress levels. The gages are positioned in a tri-axial orientation in a rectangular rosette circuit. The magnitude and direction of principal stresses can be obtained using rosette analysis. Figure 4-3 shows the orientation of strain gauges.

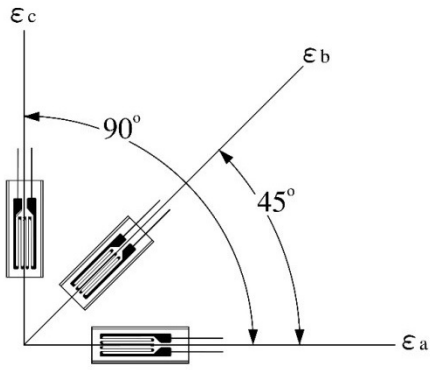

Figure 4-3. Rosette rectangular orientation

The governing equations to calculate the direction and magnitude of principal stresses are presented in Equations 4-1 to 4-3.

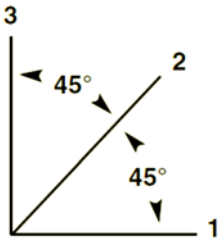

$$\epsilon_{p,q} = \frac{1}{2}\left[\epsilon_1 + \epsilon_3 \pm \sqrt{(\epsilon_1 - \epsilon_3)^2 + (2\epsilon_2 - \epsilon_1 - \epsilon_3)^2}\right] \quad \text{Eq. 4-1}$$

$$\sigma_{p,q} = \frac{E}{2}\left[\frac{\epsilon_1 + \epsilon_3}{1-\nu} \pm \frac{1}{1+\nu}\sqrt{(\epsilon_1 - \epsilon_3)^2 + (2\epsilon_2 - \epsilon_1 - \epsilon_3)^2}\right] \quad \text{Eq. 4-2}$$

$$\theta_{p,q} = \frac{1}{2}\tan^{-1}\frac{2\epsilon_2 - \epsilon_1 - \epsilon_3}{\epsilon_1 - \epsilon_3} \quad \text{Eq. 4-3}$$

where

$\epsilon_1, \epsilon_2, \epsilon_3$: Strain in direction 1, 2 and 3

$\sigma_{p,q}$: Principal stresses

$\epsilon_{p,q}$: Principal strains

$\theta_{p,q}$: Angle from the axis of gage 1 to the nearest principal axis.

In Figure 4-4 the location of the strain gauges on the support frame is shown.

The specifications of the strain gauges are presented in Appendix 3. Two linear position sensors (LVDT) are used to monitor the linear displacements in the experiment. The first LVDT is installed on the upper surface of the middle croshead and the tip of the measuring cable is connected to the lower surface of the top crosshead by a magnetic hook (Figure 4-5). This sensor measures the linear displacement of the test machine bed frame. Combination of the outputs from this sensor and the load cell provides the Load-Displacement curve.

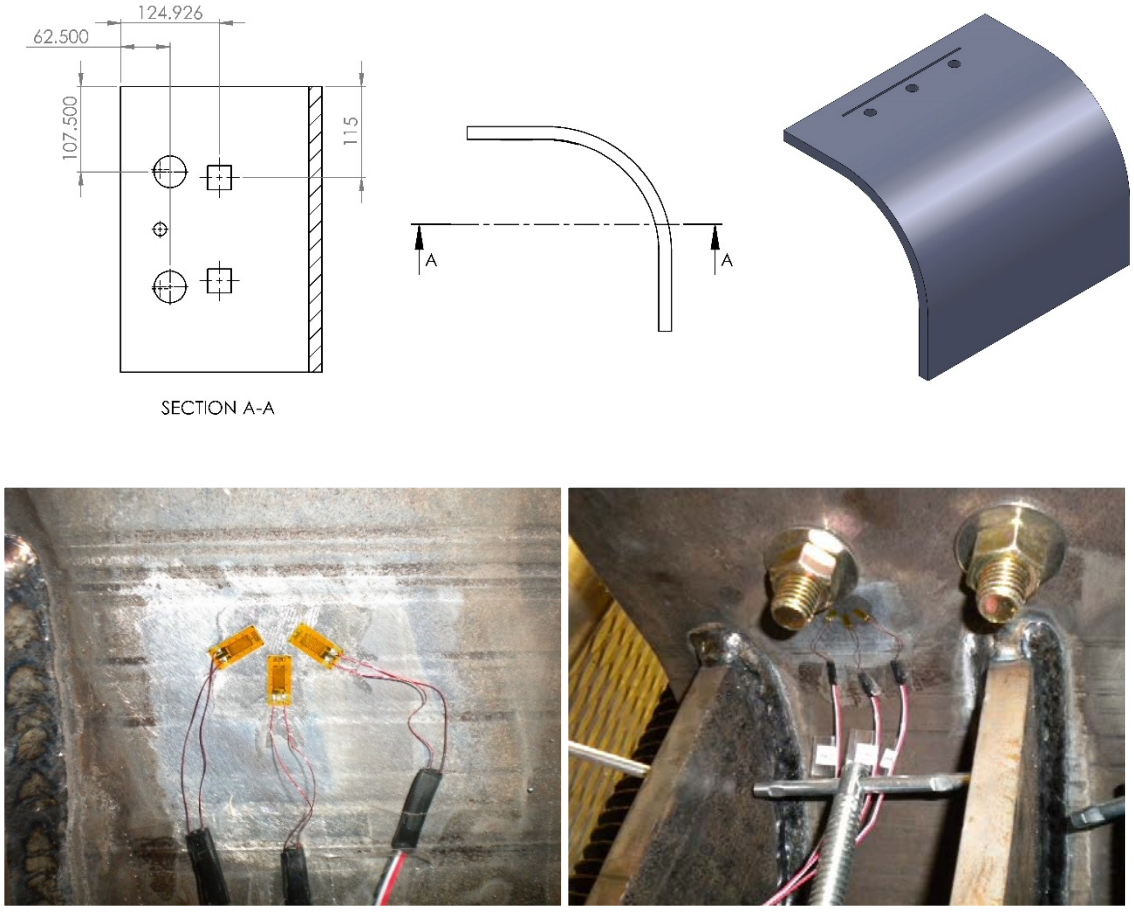

Figure 4-4. The location of the strain gauges on the edge of the support frame and installation on the support frame

The second LVDT is connected to the edge of the support frame to measure any displacement during the indentation. This sensor is used to monitor deflection of the support frame and assess the data to analyze the rigidity of the support frame under the lateral load of the indenter. The specifications of the LVDT sensors are presented in Appendix 3.

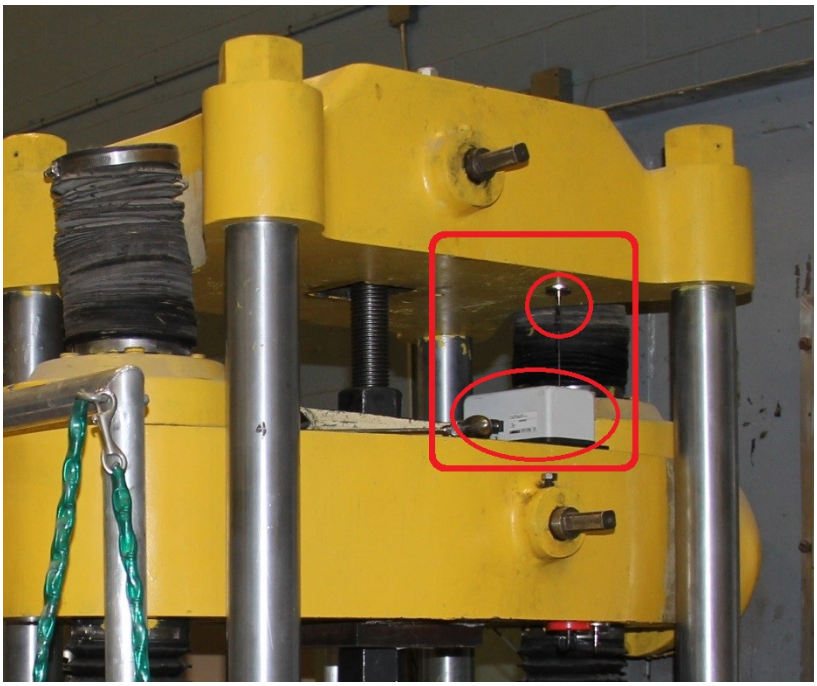

Figure 4-5. Position of LVDT No. 1

The total load applied to the support frame and test plate is measured by a load cell that is a component of the test machine. This load cell is connected to the lower part of the bed frame. An analogue indicator is connected to the load cell which shows the instantaneous value of applied load during the test's progress. The load cell data is also recorded on a computer by a data acquisition system.

Four cameras are used to record the progress of the experiment. Two cameras are installed below the test plate and are used to record the video of the indentation progress and record the fracture initiation location. Due to space limitation between the support frame and test plate, microCAM cameras are used for this purpose. The technical specifications of these cameras are summarized in Appendix 3. Two digital cameras are installed around the supporting frame to capture images and video during the test progress from the top view.

Figure 4-6 shows the lighting and microCAM setup inside the supporting frame.

Figure 4-6. Internal lighting and camera installation

4.3.2 Installation of Supporting Frame and Test Plate

Figure 4-7 shows the arrangement of C-clamps on the support frame.

Prior to each run, a permanent marker was used to draw gridlines on the surface of the test plate. The gridlines will be used to identify the location of fracture onset in comparison to the plate's edges and the center point.

To ensure all experiment parameters and sensors were correctly set up and adjusted prior to each run, a test check sheet was prepared to check all effective items before the run. The check sheet is attached in Appendix 4.

Figure 4-7. Layout of supporting frame on test machine bed

4.3.3 Experiment design

The experiment parameters are summarized in Table 4-1. The purpose of this study it is to analyze the plate behaviour under lateral indentation by a rigid indenter in quasi-static mode

by moving the indenter at very low velocity against the test plate. In quasi-static analysis, the inertial effects are very low and the associated kinetic energy is negligible.

Two plate thicknesses are selected for the review, mild steel for the thin plate and high tensile strength steel for thick plate. Material properties were introduced in Chapter 2.

As a side study the following are also studied in the experiment:

1 The indentation is applied at two different speeds to evaluate the effect of speed on the final results and review the results in non-quasi static mode.

2 The test plates are cut in two directions, parallel and perpendicular to the rolling directions, to study the effects on the plate behaviour.

Table 4-1. List of experiment parameters

Parameter	**Cutting Direction**		**Plate thickness**		**Steel Grade**		**Indenter**			**Speed**		
Test Number	Parallel	Perpendicular	3.18 mm	6.35 mm	A	EH 40	Rigid	Soft	Ice	0.1 mm/s	1.2 mm/s	1.6 mm/s
01		×	×		×		×			×		
02	×		×		×		×			×		
03	×		×		×		×				×	
04		×	×		×				×	×		

05	×		×		×			×		×		
06		×	×		×			×		×		
07		×	×		×		×				×	
08		×	×		×		×					×
10		×		×		×	×			×		
11		×		×		×		×		×		
12	×			×		×	×				×	

4.4 Experimental Results

In the following figures, force-displacement curves from the experimental results are presented.

4.4.1 Test results for thin plates

Figure 4-8 shows force-displacement curves for thin steel plates under the effect of a rigid indenter. The results are discussed in paragraphs A to D below.

A. Comparison of results for Test 01 and 02:

   The results of Test 01 and 02 are presented in Figure 4-8 by a short dashed line and solid line, respectively. In these two tests, the plate behaviour is almost identical and it can be understood that the rolling direction is not an effective parameter at lower speeds. The difference in the maximum force and total displacement at rupture is less than 3% and 1%, respectively. A closer comparison of the diagram for Test 01 and 02 is presented in Figure 4-9.

B. Comparison of results for Test 07, 08, and 03

According to the results of the experiments as presented in Figure 4-8, at a higher indentation speed, the fracture onset occurs at a lower load level and lower displacement. Also, the experimental results for Test 07 and 03 show that the rolling direction parallel to the axis of the plate length provides a higher strength level for the thin plate. A closer comparison of Tests 07, 08 and 03 is presented in Figure 4-10.

C. Comparison of results for Tests 05 and 06:

The results of Tests 05 and 06 represent the plate behaviour at a slow indentation speed of a plastic indenter (Figure 4-11). Similar to the test results of a rigid indenter, the plate behaviour is independent of rolling direction at a low indentation speed. In these test results, the minor fluctuations along the Force-Displacement curve represent the crushing behaviour of the soft indenter during the test progress. The outer surface of the soft indenter does not crush like an ice sample, but its general behaviour in terms of minor fluctuations is similar to the crushing of an ice sample against the plate. According to results of Test 05 and 06, the fracture onset occurs at a lower load level and displacement in comparison to similar tests with a rigid indenter (Tests 01 and 02).

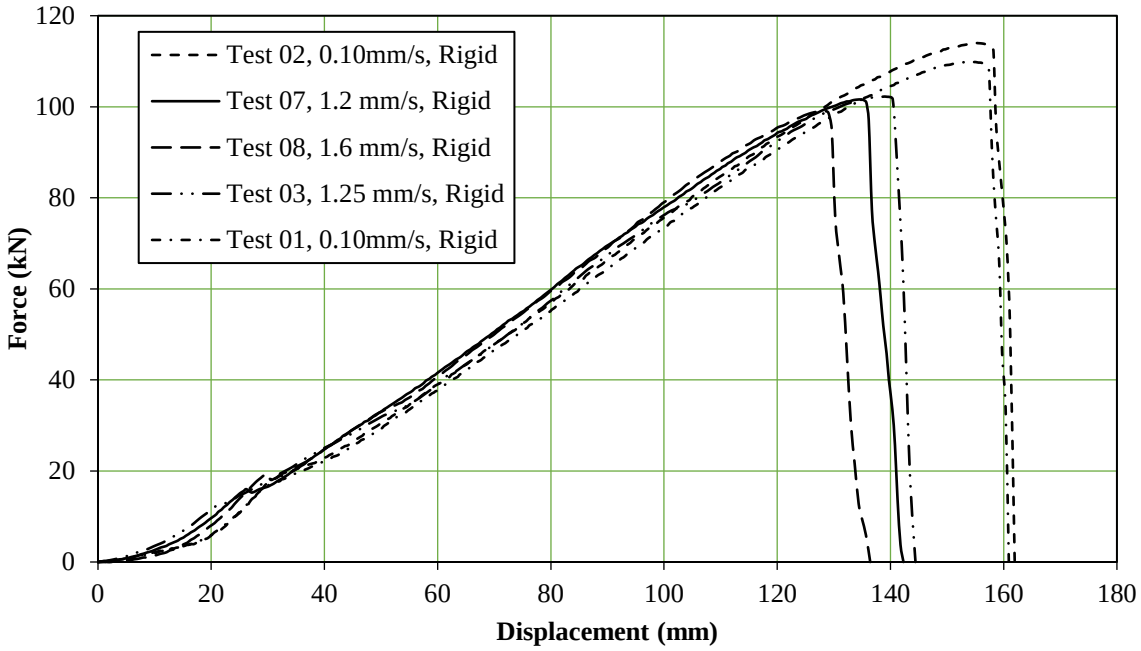

Figure 4-8. Behaviour of thin plates under effect of rigid indenter

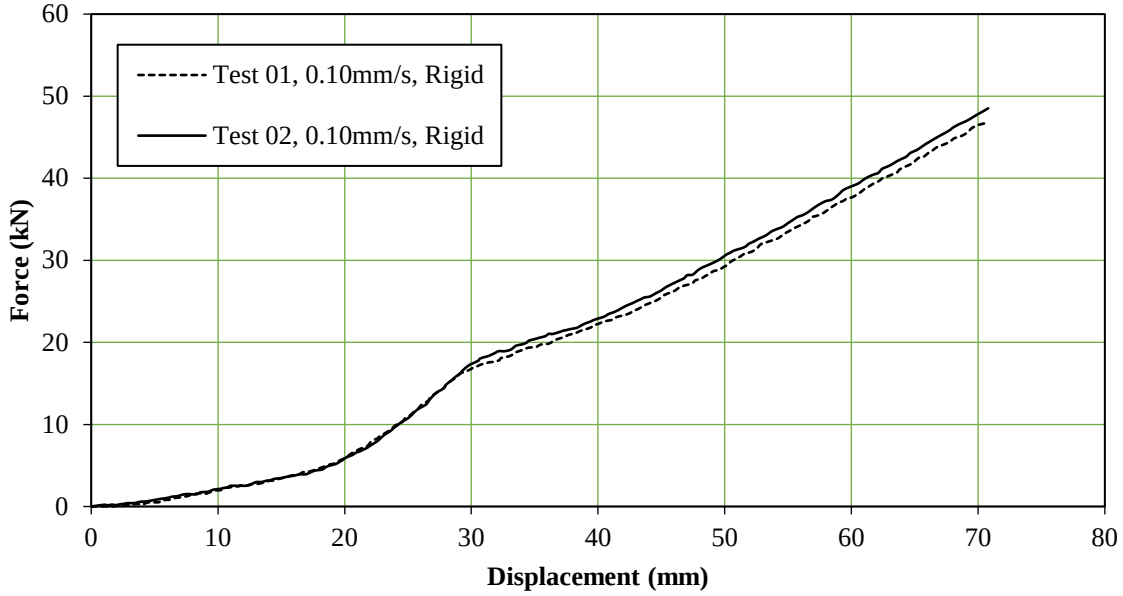

Figure 4-9. Behaviour of thin plates under effect of rigid indenter, Tests 01 and 02

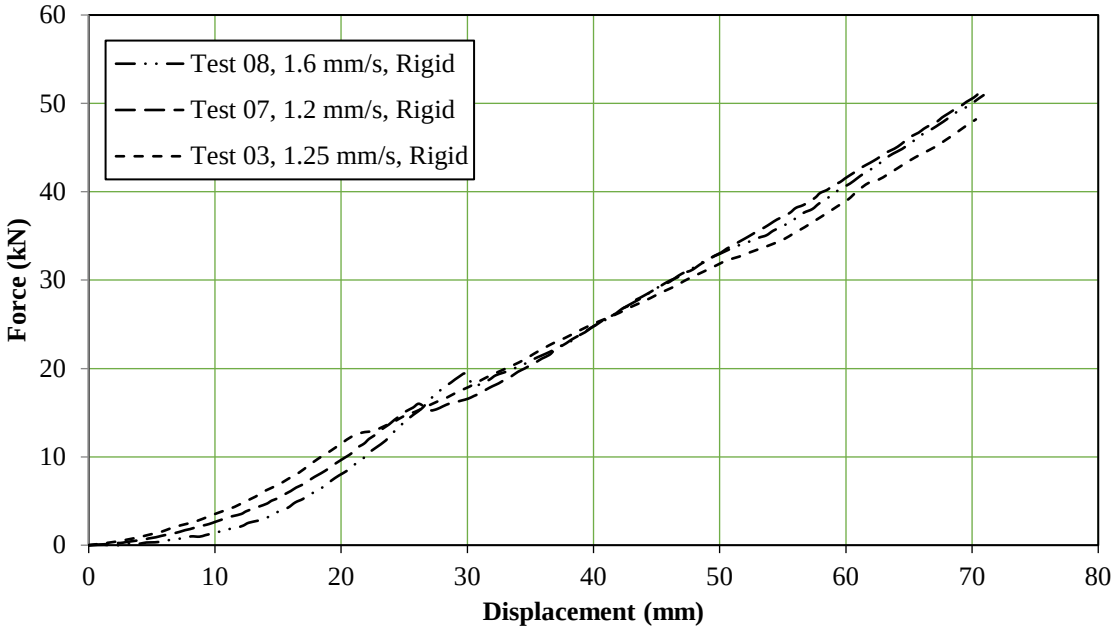

Figure 4-10. Behaviour of thin plates under effect of rigid indenter, Tests 07, 08 and 03

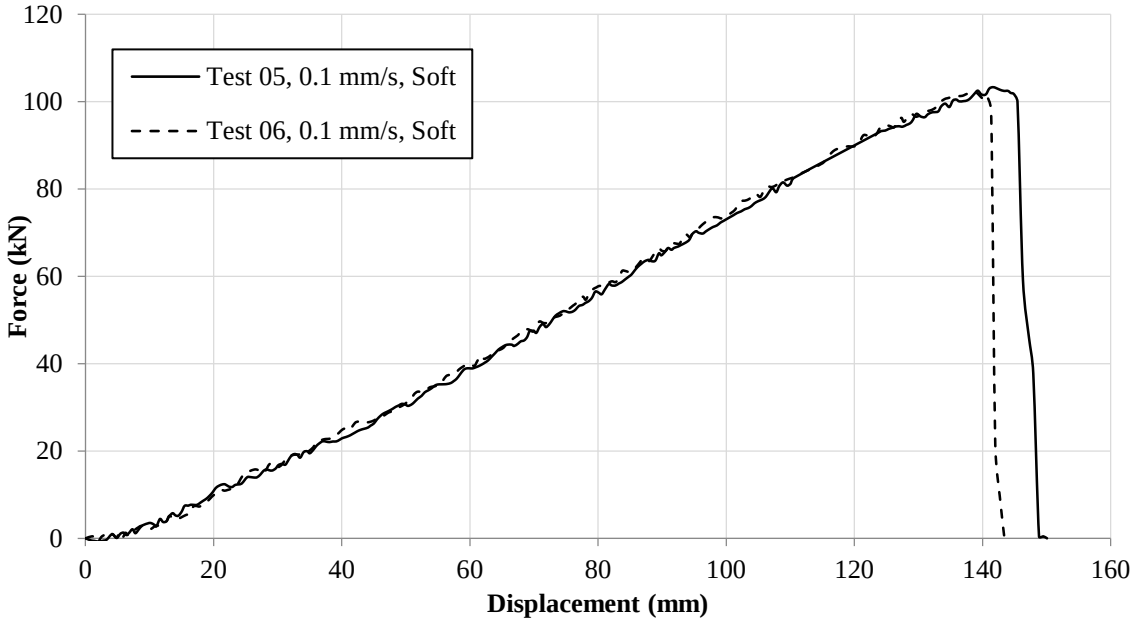

Figure 4-11. Behaviour of thin plates under effect of plastic indenter

D. Results of Test 04 with an ice sample as indenter:

In Test No. 04, truncated cone ice samples were used as indenters. The ice samples were fabricated using purified degassed water and ice chips. The samples were fabricated in circular based moulds with a diameter and height of 25 and 35 cm, respectively. The initial shape of the samples was cylindrical, and a hand saw was used to shape truncated cone samples. The diameter of the upper part of the sample was approximately 10 cm. Figure 4-12 shows one ice sample.

The crushing experiment was conducted at the Structure lab and it was not possible to decrease the temperature to a sub-zero degree. At the time of the experiment, the environmental temperature was about 11˚C. In order to decrease the melting rate during the indentation, the test plate was held in the cold room till it reached the constant temperature of -10˚C. Additionally, some ice bags were placed around the test plate and supporting frame to decrease the temperature around the test specimen.

Figure 4-12. Fabricated ice sample

In this experiment, two ice samples were used. The first ice indenter was pushed against the steel plate up to a total displacement of 151 mm associated with a 146 kN load. That ice sample did not break the test plate. Figure 4-13 shows the progress of indentation of the first ice sample in 5 positions. Although the above noted displacement and force values were relatively higher than the values that were recorded at the time of plate rupture in previous tests, the test plate did not break in Test No. 04. The reasons can be summarized as follows:

- The LVDT sensor records the total displacement of the middle ram that is located on top of the indenter head. In this test, the total displacement is the sum of deflection of the test plate and crushing of ice sample. Therefore, the real deflection of the steel plate is less than the recorded displacement by the sensor.

- The load cell is connected to the bed frame. It records the total force applied to the bed frame by the indenter. In this test, during the crushing, since the upper part of the ice sample is wider than the distance between the side walls of the support frame, the ice sample will be confined between the test plate and frame side walls while pushed down by the ice steel holder connected to the middle ram. Therefore, a portion of total recorded force is applied to the supporting frame walls in addition to the test plate.

A second ice indenter with dimensions similar to the first indenter was used to continue the crushing experiment on the deflected plate. The second indenter also did not break the steel plate. Figure 4-14 shows the side view of the deflected test plate. Total permanent set at the middle of steel plate was about 112 mm after the experiment.

(a) (b)

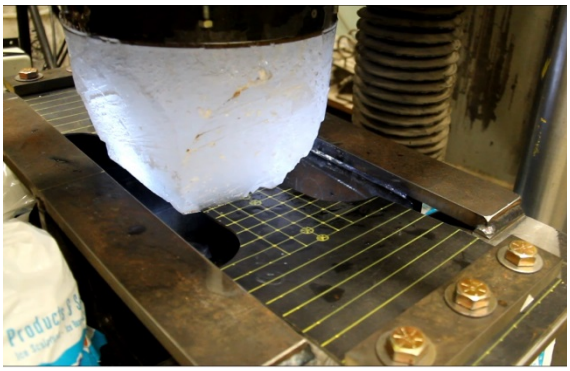

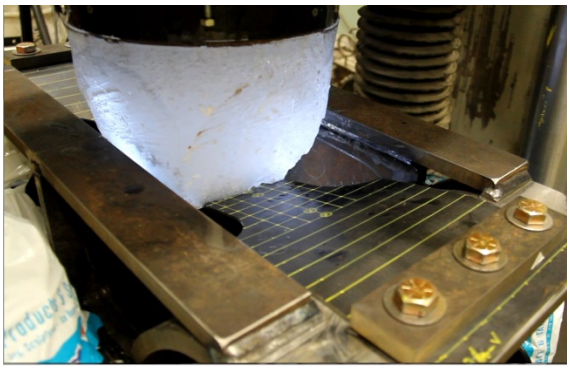

(c) (d)

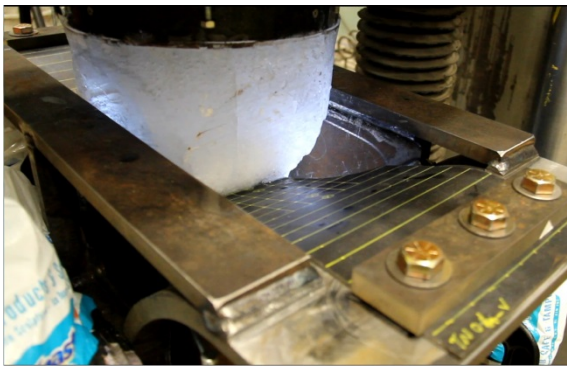

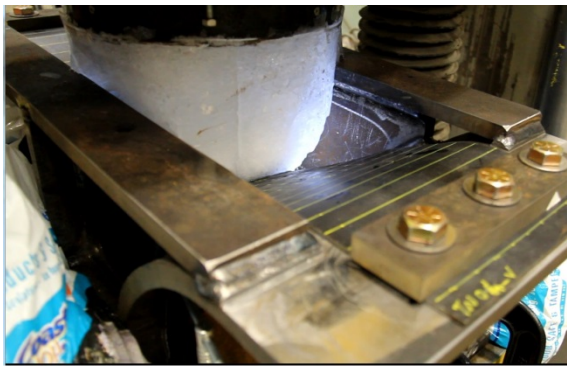

(e)

Figure 4-13. Progress of Test No. 04 under effect of first ice indenter

Figure 4-14. Side view of test plate after Test No. 04

Figure 4-15 shows the force-displacement curve for Test No. 04. In this diagram, the test results for indentation experiments of both samples are presented. It can be understood that “Limit Stress” (Croasdale K.R.) is the governing limit concept in the failure of the ice sample prior to plate rupture. The circled areas on the force-displacement diagram show the effect of fracture in the ice samples that causes localized fluctuations in the curves.

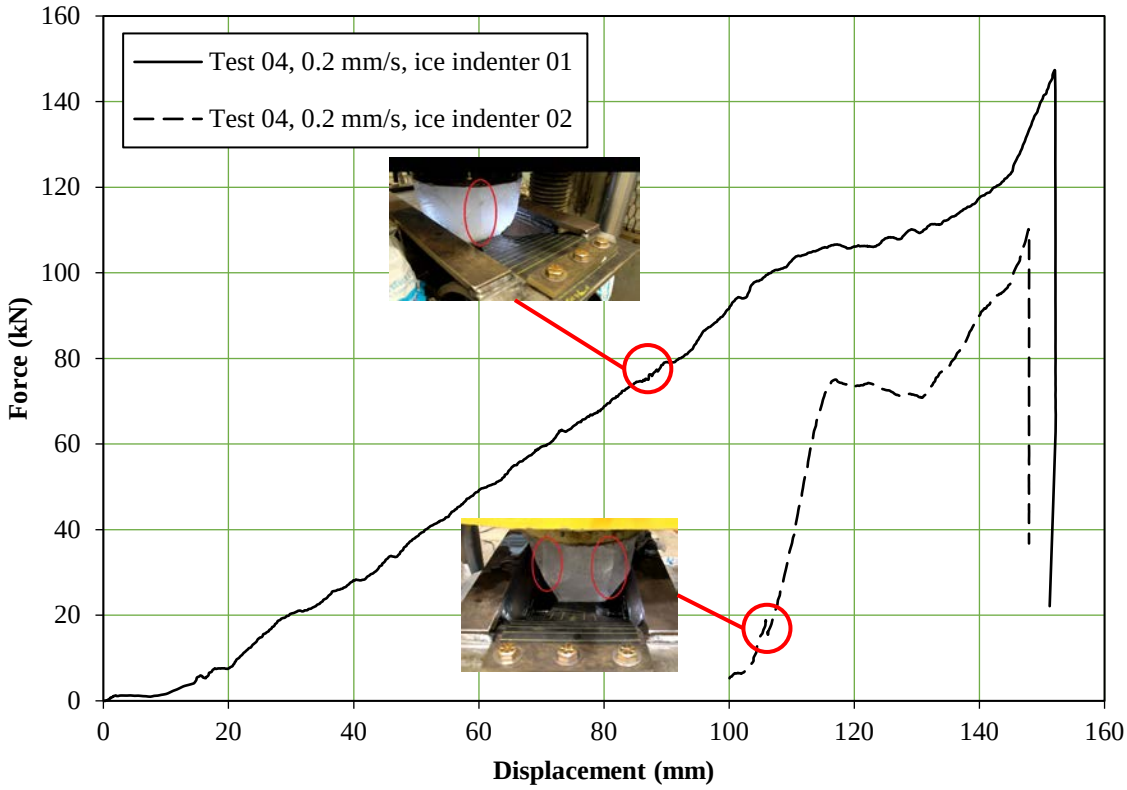

Figure 4-15. Force-displacement diagram, Test No. 04

4.4.2 Test results for thick plates

The thick steel plates' results are presented in Figure 4-16. Two experiments were conducted at an indentation speed of 0.1 mm/s with rigid and soft indenters and one test was conducted at a speed of 1.2 mm/s with rigid indenter.

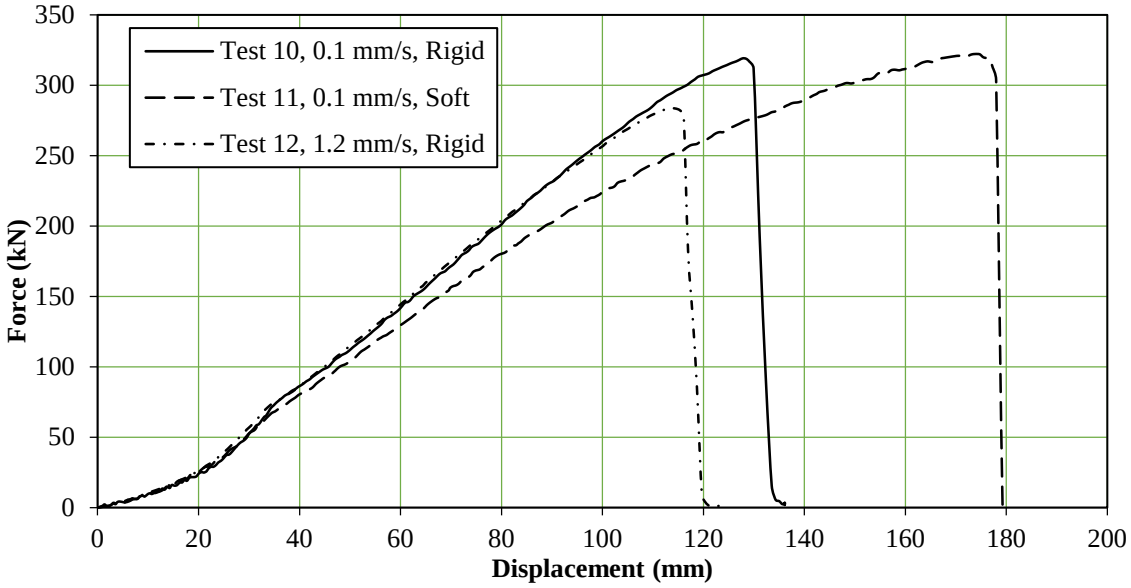

Figure 4-16. Behaviour of the thick plates under effect of rigid and plastic indenter

Diagrams of Tests 10 and 12 show the results of slow and high speed tests, respectively, under the effect of the rigid indenter. The force-displacement curve of the thick plate at higher speed is similar to the plate behaviour at low speed; however, the fracture onset occurs at a lower load level. The diagram of Test No. 11 shows the indentation experiment under the effect of the soft indenter at low speed. In this test, fracture onset occurs at a larger displacement in comparison to the results of the rigid indenter. This difference is the result of deformation of the soft indenter. In the crushing experiment with a plastic indenter, similar to Test No. 04, the indenter starts to deform during the test progress and eventually is totally deformed in the path of its connection to the rigid nut on top of the indenter head and also along its connection to the steel test plate. Therefore, the total displacement recorded by LVDT sensor is the sum of test plate deflection and also the deformation of the soft indenter. In Figure 4-17, the deformed soft indenter after the crushing test is shown.

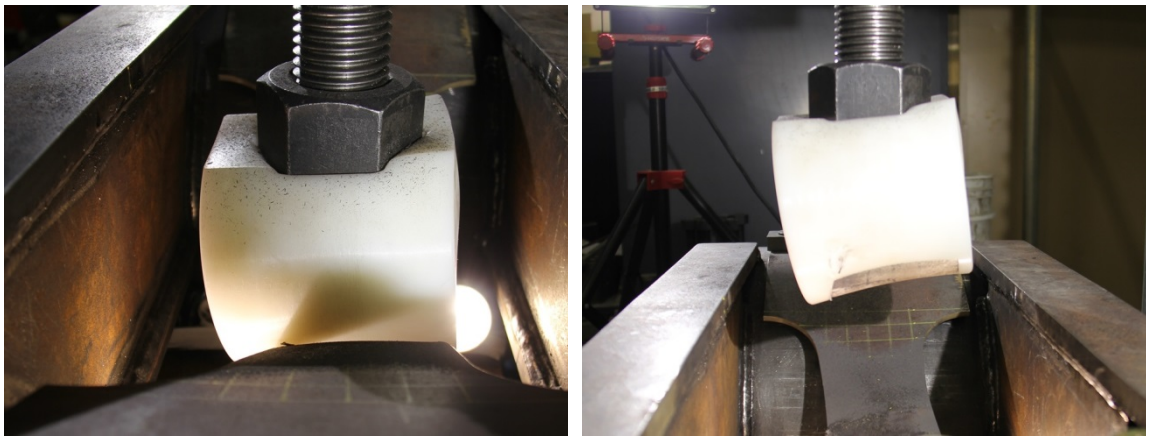

Figure 4-17. Deformed soft indenter after completion of Test No. 11

In the following figures, representative pictures of the crack propagation and broken test plates are presented.

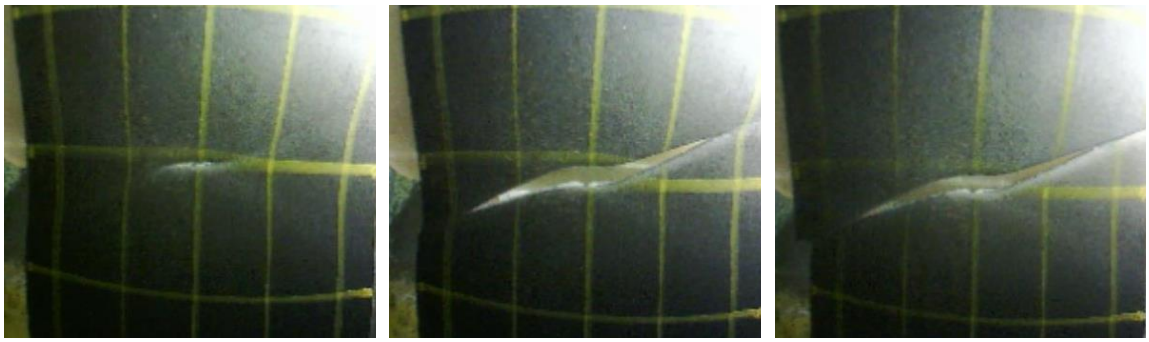

Figure 4-18. Crack propagation in the thin plate, Test No. 01

Figure 4-19. Crack propagation in the thin plate, Test No. 02

Figure 4-20. Crack propagation in the thin plate, Test No. 03

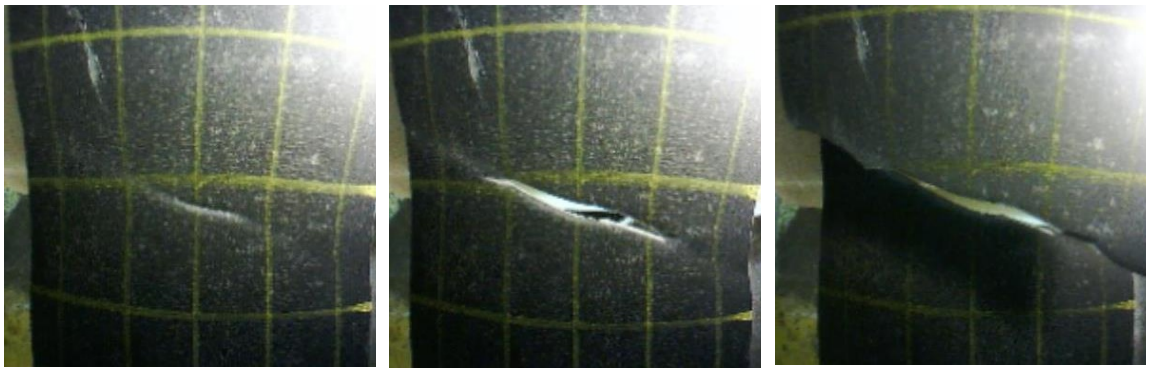

Figure 4-21. Crack propagation in the thin plate, Test No. 05

Figure 4-22. Crack propagation in the thin plate, Test No. 06

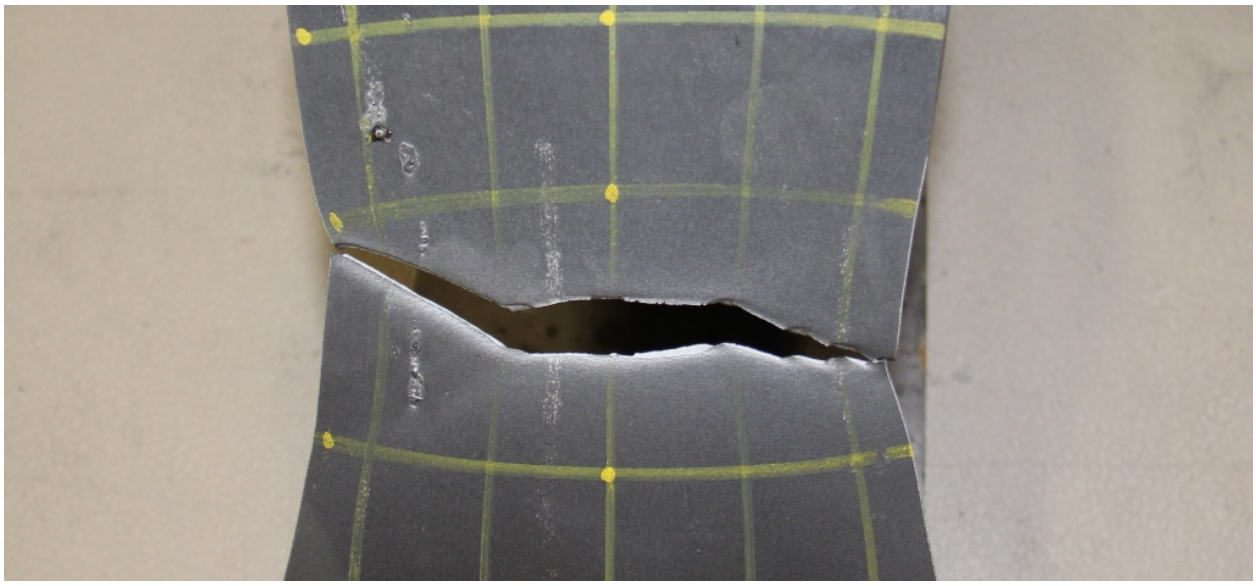

Figure 4-23. Broken test plate, Test No. 07

Figure 4-24. Crack propagation in the thick plate, Test No. 08

Figure 4-25. Crack propagation in the thick plate, Test No. 10

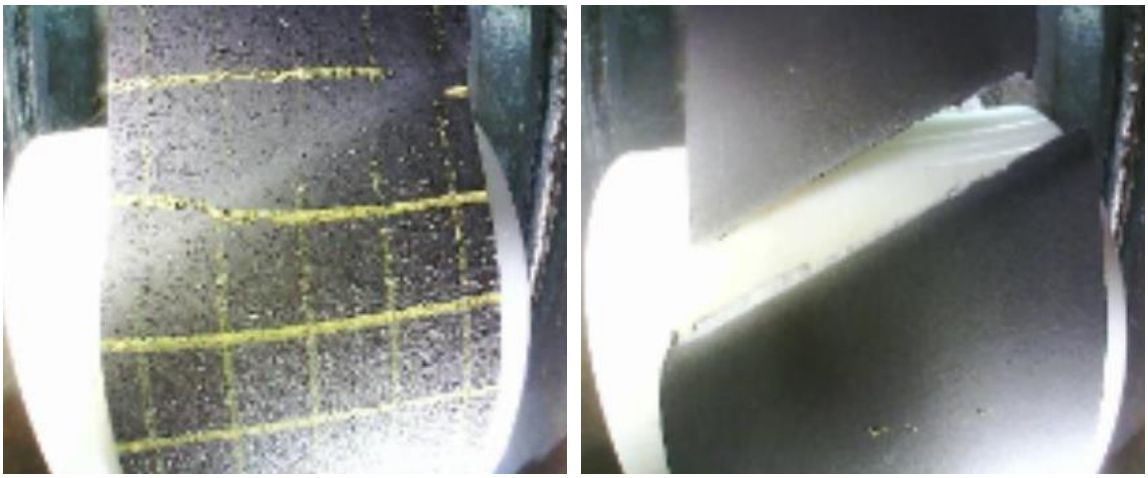

Figure 4-26. Crack propagation in the thick plate, Test No. 11

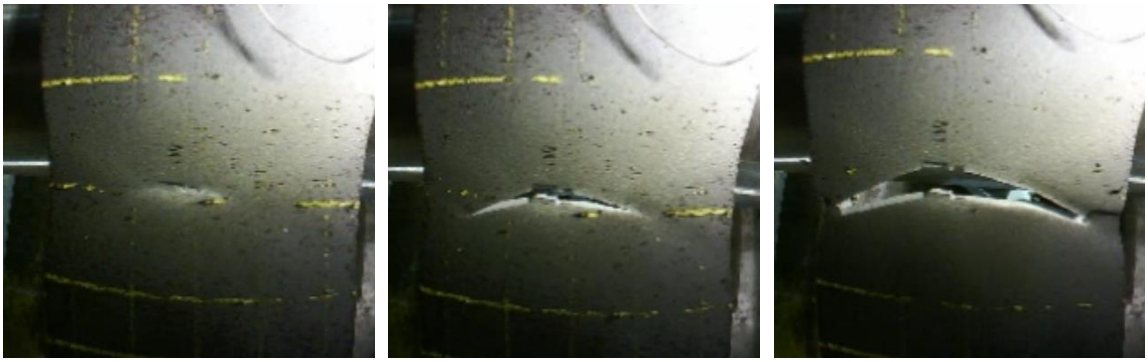

Figure 4-27. Crack propagation in the thick plate, Test No. 12

In all of the preceding tests, the fracture started in the middle of the plate width and propagated toward the edges with an angle about 45 degrees relative to the longitudinal axis of the plate.

In Table 4-2 the test results are summarized for those noted tests.

Table 4-2. Summary of test results

Test	Max Force (kN)	Max Disp.[1] (mm)	Width at rupture[2] (mm)	Rupture location[3]
01	111.98 kN	156.37 mm	76.40 mm	315 mm
02	114.01 kN	154.94 mm	78.80 mm	305 mm
03	107.26 kN	145.74 mm	78.97 mm	320 mm
04	---	111.50 mm[4]	---	---
05	103.33 kN	141.60 mm	77.35 mm	315 mm
06	102.27 kN	138.63 mm	78.20 mm	325 mm
07	101.61 kN	134.71 mm	77.92 mm	290 mm
08	99.11 kN	127.73 mm	78.12 mm	315 mm
10	322.23 kN	128.79 mm	84.80 mm	322 mm
11	319.15 kN	174.30 mm	84.50 mm	335 mm
12	283.81 kN	113.74 mm	84.55 mm	325 mm

Notes:
[1] Total displacement of center of test plate at the time fracture onset
[2] Width of the test plate at location of fracture following necking. The original width was 100 mm. In Figure 4-28, a sample is presented.
[3] Relative to the edge of the test plate
[4] Permanent set in steel test plate

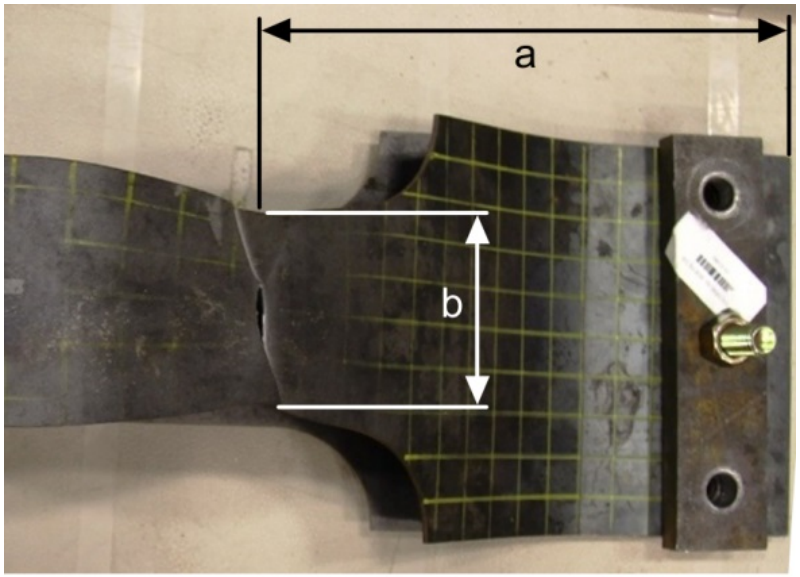

a: distance from plate edge; b: plate width at fracture line

Figure 4-28. Sample of measurements on broken test plate

4.4.3 Results of strain gauge recordings

As noted in previous sections, a combination of 12 strain gauges in 4 groups was used to record the strain level in the supporting frame during the indentation tests. The maximum stress and strain values were recorded for Test No. 11 as follows:

- Maximum principal stress: 271.58 MPa
- Maximum principal strain: 1.10E-3

As expected, the maximum stress value was lower than the yield point and the supporting frame did not experience any plastic deformation.

4.5 Microstructure Study of the Test Plates

As a side study, the microstructure of the steel test plates was reviewed before and after the indentation test.

For this study, small specimens were cut in intact and broken conditions before and after the indentation tests. In the broken sample, the specimen was cut adjacent to the ruptured edge. In order to facilitate working with small sized specimens, they were mounted in plastic molds. The cross section of the specimen was ground gradually by using various coarse to fine sandpapers and the ground surface was polished by a fine diamond powder. Following completion of grinding and polishing, etching liquid was applied. The grain structure of the prepared specimens was examined under a microscope and digital images were produced at 100, 500, and 1000 magnifications. In Figures 4-29 and 4-30 the

microstructure of thin and tick test plates are presented. The magnification in both figures is 1000.

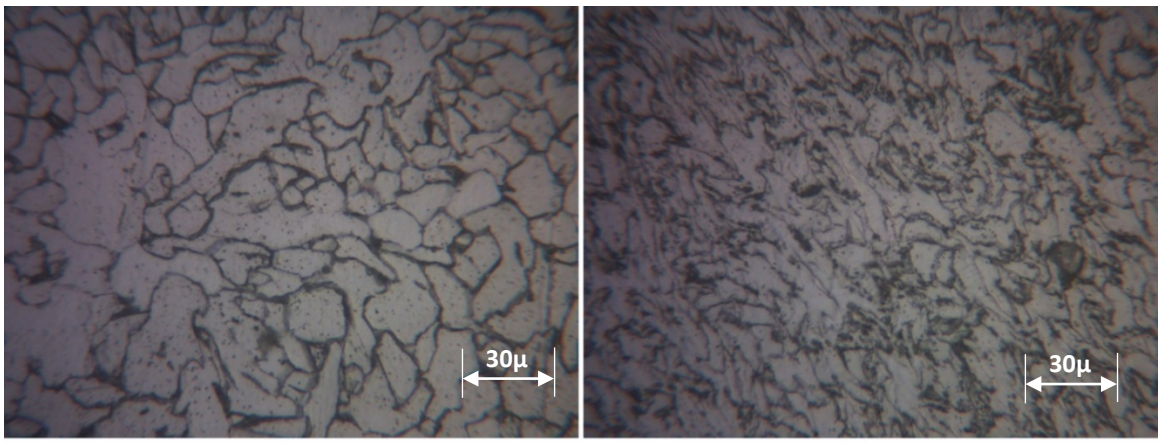

(a) (b)

Figure 4-29. Microstructure of surface of the thin test specimen. (a) intact (b) broken sample

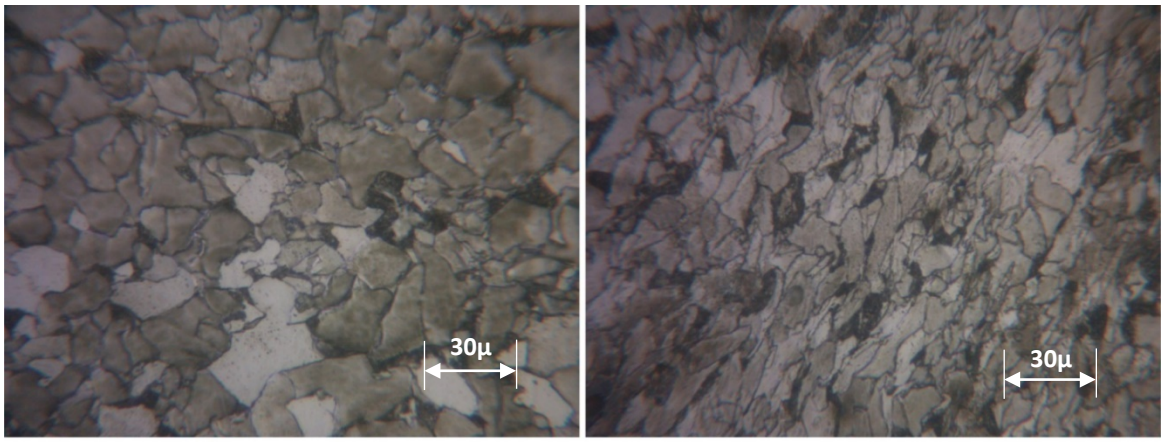

(a) (b)

Figure 4-30. Microstructure of surface of the thick test specimen. (a) intact (b) broken sample

As can be seen in these figures, in comparison to the intact specimens, the grains of the steel specimens are elongated after testing.

Chapter 5: Comparison and Conclusions

5.1 Discussion and Conclusions

The goal of the present work has been to analyze steel plate behaviour to develop a simplified tool for prediction of failure and fracture onset. The research was conducted in two stages. In the first stage, theoretical calculation and non-linear finite element analysis have been conducted to analyze plate behaviour and design the test setup. In the second stage, experimental work has been done to evaluate the analytical and FEA results.

Two plate thicknesses represented by “thin plate” and “thick plate” have been selected for the study. Table 2-5 shows the scantling and mechanical properties of the plates.

Figure 5-1 shows the behaviour of the thin plate based on FEA, theoretical, and experimental analyses. The FEA analysis was completed in quasi static mode and therefore, the results of Test No. 01 (experiment) are compared to the numerical analysis results. With reference to Figure 5-1, the conclusions can be summarized as follows:

- According to experimental results, fracture onset occurs at the displacement of 153 mm associated with the load level of 110 kN.
- Theoretical analysis using Elastic-plastic (EP) behaviour represents the behaviour of the steel plate at lower strain levels. At higher strain levels, EP underestimates the force-displacement behaviour of the steel plate.
- Theoretical analysis using Plastic behaviour predicts the steel plate behaviour at a higher strain level. At a strain level of more than 0.12, the force-displacement curve predicts the plate behaviour accurately, in comparison with the experimental results.

- By combining the experimental result and strain level estimated by the theoretical analysis (Plastic behaviour), strain at fracture onset is estimated as 0.195.
- Finite element analysis overestimates the plate behaviour in comparison to the experiment results. The reason for the higher level of predicted force is the modeling assumption in the FEA model. The Tangent Modulus for the thin plate is assumed to be equal to 1000 MPa in the design stage; however, analysis of tensile test results show that the Tangent modulus for the thin plate is about 720 MPa.
- At critical strain criterion, FEA results estimate the load level of 110 kN and displacement of 124 mm.

In Figure 5-2, the results of theoretical, numerical, and experimental analyses for the thick plate are presented. Test No. 10 was selected to compare its results to FEA and theoretical analysis. Based on analysis of the thick plate, the following conclusions have been made:

- According to experimental results, fracture onset occurs at the displacement of 128 mm associated with the load level of 319 kN.
- At the above noted displacement (128 mm), theoretical analysis (Equation 2-17) was used to estimate the strain level of 0.14 at a load of 325 kN. The load level predicted by Eq. 2-17 is in very good compliance with experimental results.
- At the displacement of 128 mm, displacement at rupture point from experiment, FEA estimates a strain level of 0.24 and a load level of 372 kN.
- The strain level anticipated by theoretical analysis for the thin plate (Figure 5-1) is higher than the strain level in the thick plate. This difference is due to the rigidity of the thick steel plate in comparison to the thin plate. In the theoretical calculation,

as presented in Chapter 2, the strain level is a function of lateral displacement. In the case of the thin plate, the rupture initiated after 161 mm lateral indentation, that is approximately 25% more than the lateral indentation at the rupture point in the thick plate.

- The critical strain criterion of 0.2, in the theoretical analysis predicts the rupture at a load of 378 kN, 19% higher than experimental results.
- At critical strain criterion, FEA results estimate the load level of 343 kN and displacement of 120 mm, 7% more than the experimental results in the load level.

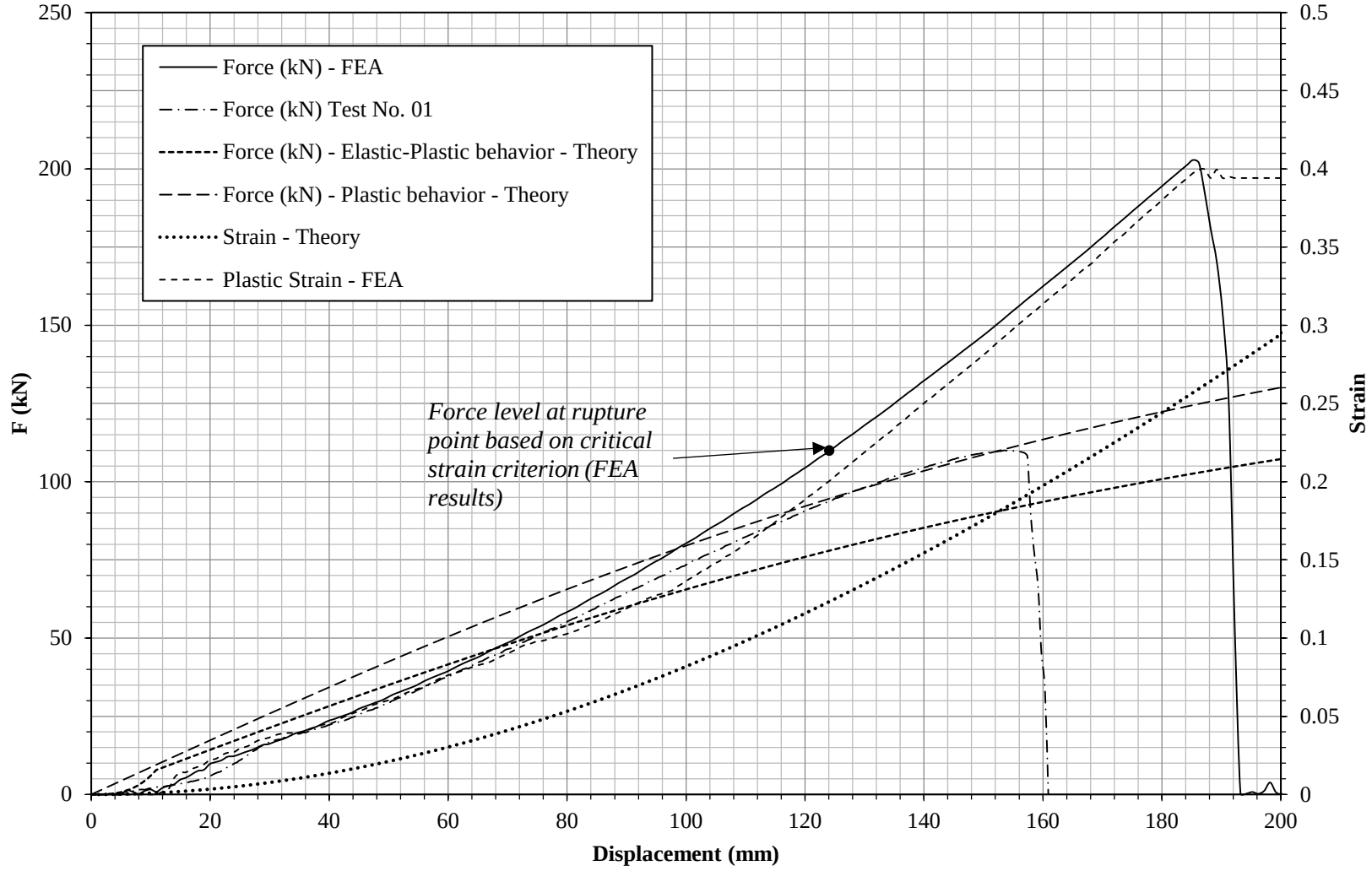

Figure 5-1. Comparison of Theoretical, Numerical and FEA results for thin steel plate

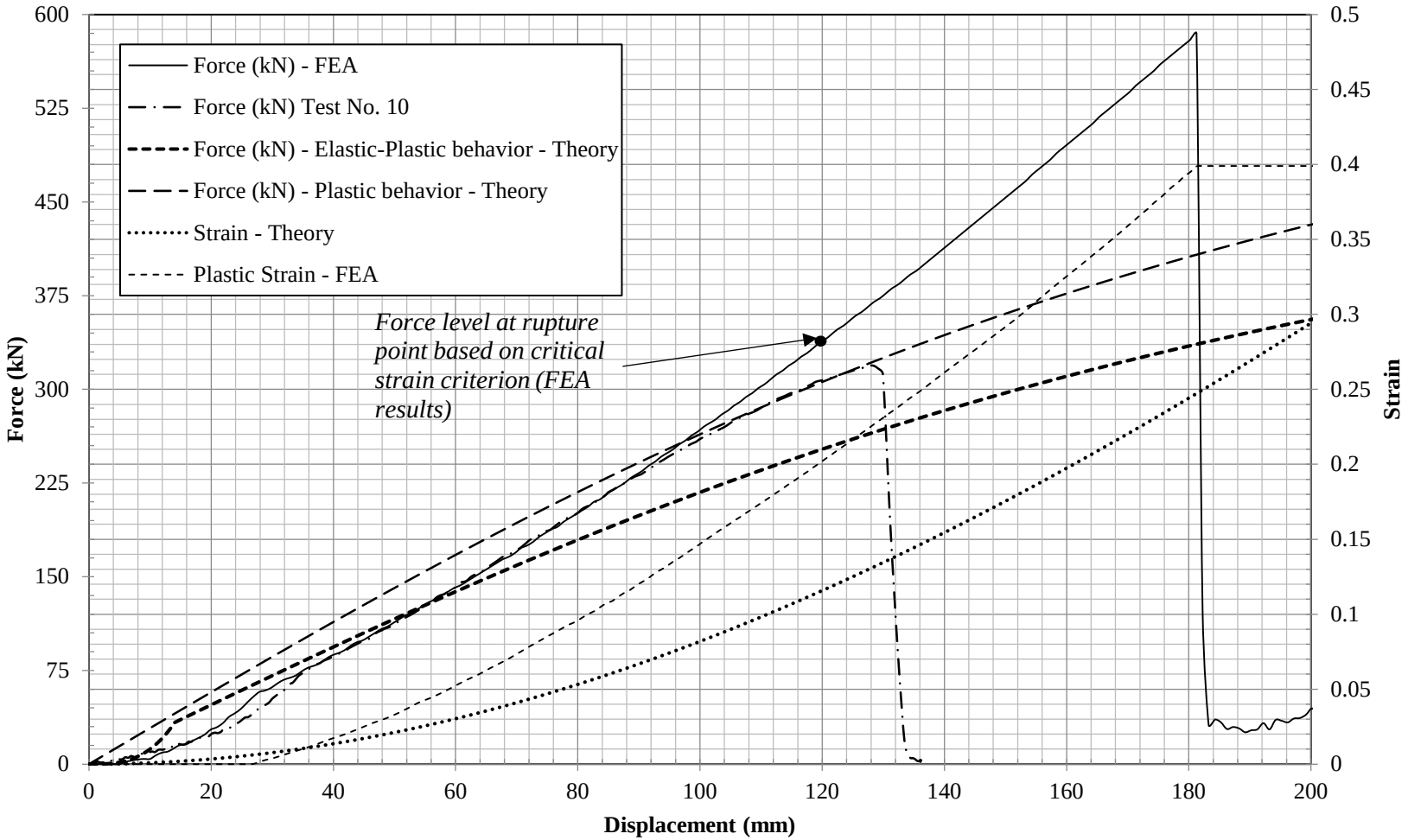

Figure 5-2. Comparison of Theoretical, Numerical and FEA results for thick steel plate

It can be concluded that in steel plate fracture under quasi static lateral loads:

- The theoretical solution as presented in Chapter 3 provides an accurate estimation for the behaviour of a mild steel plate in combination with the critical strain level of 0.2.
- Finite Element Analysis provides more accurate estimation for high tensile steel plate behaviour in combination with the critical strain level, in contrast to theoretical solution.
- The theoretical solution based on Elastic-plastic behaviour provides reasonable results at the lower strain level (less than 0.1).

Considering the experimental results from Chapter 4, at higher strain rates and under the effect of a faster moving load, fracture initiates at lower load and displacement levels.

Based on the aforementioned conclusion, the research objective was achieved by providing an estimation model based on simplified fracture criterion in combination with finite element analysis and a governing equation from analytical solution.

5.2 Recommendations for future works

In this study, the fracture onset at the middle of an unsupported steel plate under a lateral uniform load has been analyzed. Fracture analysis in a supported steel plate would study effect of grillage structure on location of fracture onset, the total failure load and accuracy of critical rupture strain. As mentioned in previous chapters, due to uncontrolled laboratory temperature and limitation of test machine, ice sample could not be used to rupture the steel plate. Employment of a bigger test setup with higher capacity of test machine can be used to initiate the fracture in the steel plate.

Appendix 1: Design of Bolts, keys and keyways

FEA Model to Derive the Forces

Using FEA, the total amount of forces in horizontal and vertical directions are calculated at each end of the test plate where it is connected to the boundary condition. In the FEA model, the connection is made by merging the duplicated nodes between the test plate and the supporting frame. The details of the FEA model are presented in Chapter 3. It should be noted that the failure criterion in the test specimen is a strain level equal to 0.4, which is a relatively conservative design and will overestimate the total force required to initiate the rupture in the plate field.

In design of bolts and keyways, the estimated horizontal and vertical loads at boundaries are used to calculate the normal and shear strength of the connection. The normal strength calculations are conducted by considering the yield strength of the bolts as the threshold value. The selected bolt for connection design is Grade 8 and its mechanical properties are summarized in Table A1-1. The minimum shear area of the bolts is calculated by considering the shear strength of the bolt material. The shear strength value is estimated to be about 60% of the ultimate strength of the bolt material.

Table A1-1. Mechanical properties of Grade 8 bolt.

Grade	Min. Tensile Strength (MPa)	Min. Yield Strength (MPa)	Elongation, Min %	Reduction of Area, Min %
8	1034.21	896.32	12	35

For the thick plate:

Vertical force on each end:

$F_v = 294.33\ kN$

The normal yield stress of the bolt material:

$\sigma_Y = 896.32\ MPa$

Required area on each end:

$$A = SF.\frac{F_v}{\sigma_Y} = SF.328.37\ mm^2$$

Horizontal force on each end:

$F_h = 95.00\ kN$

Shear yield stress of the bolt material:

$\tau_Y = 620.53\ MPa$

Required area on each end:

$$A = SF.\frac{F_h}{\tau_Y} = SF.153.10\ mm^2$$

For the thin plate, the load level is lower than the thick plate and the bolt connection is acceptable to be used in lieu of a weld design.

Considering these calculations and the total required cross sectional area of the bolts, 3 grade 8 bolts with the nominal diameter of 5/8” (15.625 mm) are selected for each end of the test specimen. The total shank area of the bolts at each end of the test specimen with 5/8” bolts is equal to 575.25 mm^2 , which provides a safety factor of 1.75 (175 %) for

normal strength and a safety factor of 3.5 (350 %) for shear strength. In the direct calculations, the effect of moment is neglected and the calculations are simplified. Therefore, one key is added to each end of the boundary with an effective cross section equal to 200*3.175 mm^2 in the shear direction. Figure A1-1 presents the profile view of the end connection design.

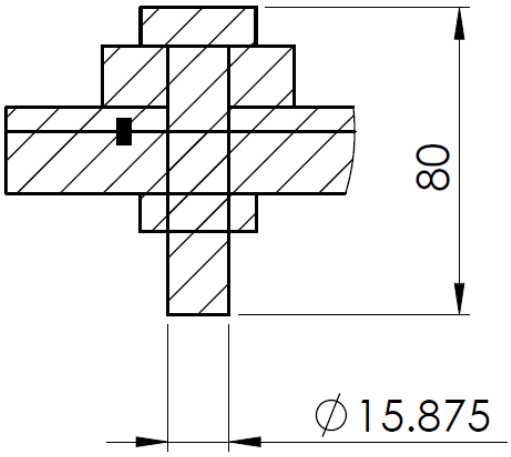

Figure A1-1. Profile view of the end connection design showing the key and one bolt

Appendix 2: Shop Drawings

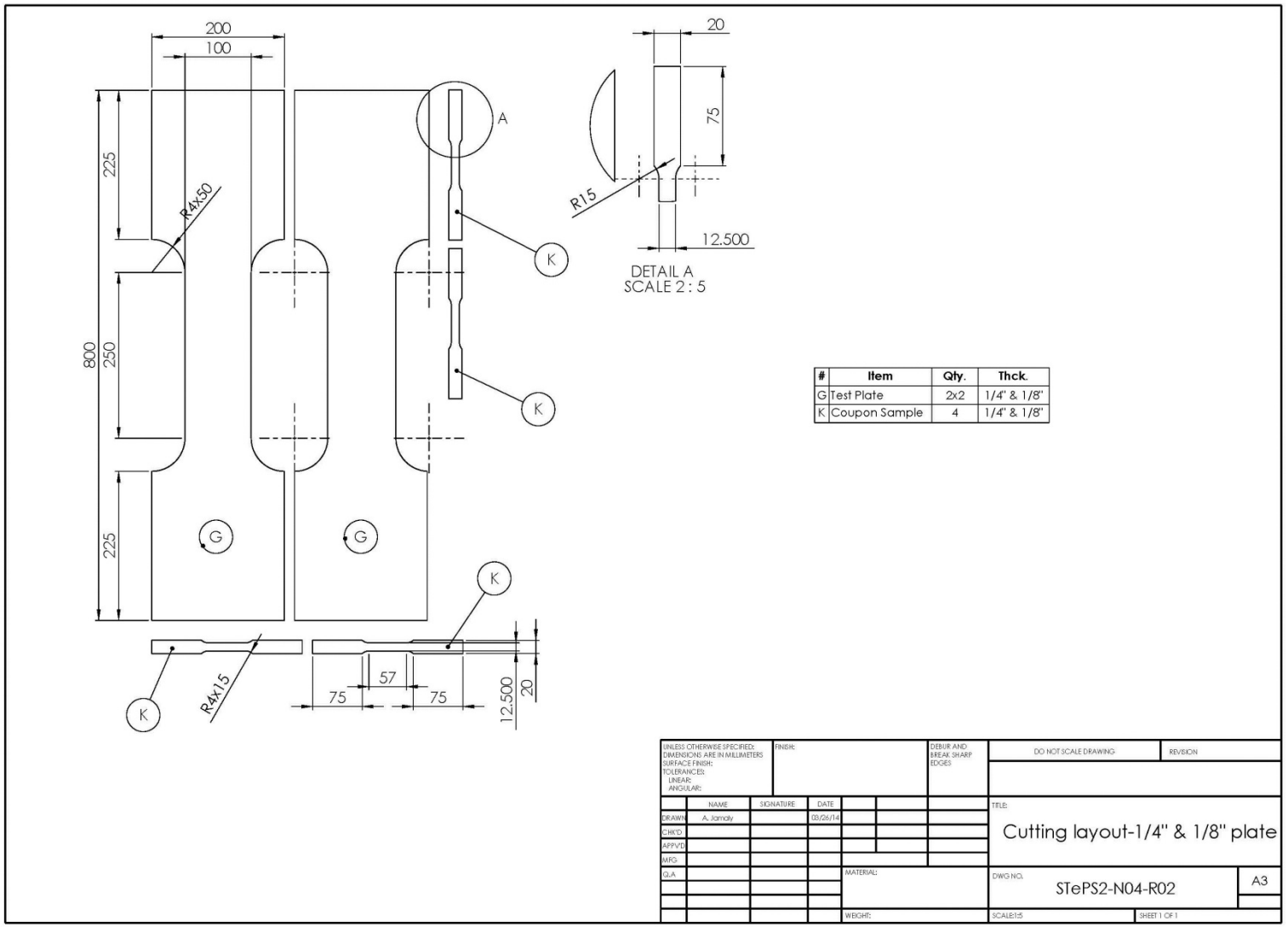

#	Item	Qty.	Thck.
G	Test Plate	2x2	1/4" & 1/8"
K	Coupon Sample	4	1/4" & 1/8"

UNLESS OTHERWISE SPECIFIED: DIMENSIONS ARE IN MILLIMETERS SURFACE FINISH: TOLERANCES: LINEAR: ANGULAR:	FINISH:	DEBUR AND BREAK SHARP EDGES	DO NOT SCALE DRAWING: REVISION
NAME / SIGNATURE / DATE			TITLE: Cutting layout-1/4" & 1/8" plate
DRAWN: A. Jamaly 03/26/14			
CHK'D			
APPV'D			
MFG			
Q.A		MATERIAL:	DWG NO. STePS2-N04-R02 A3
		WEIGHT:	SCALE:1:5 SHEET 1 OF 1

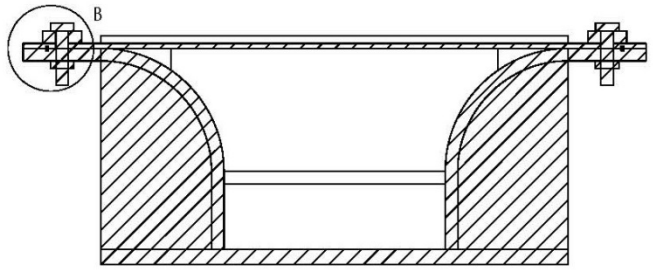

SECTION A-A
SCALE 1 : 5

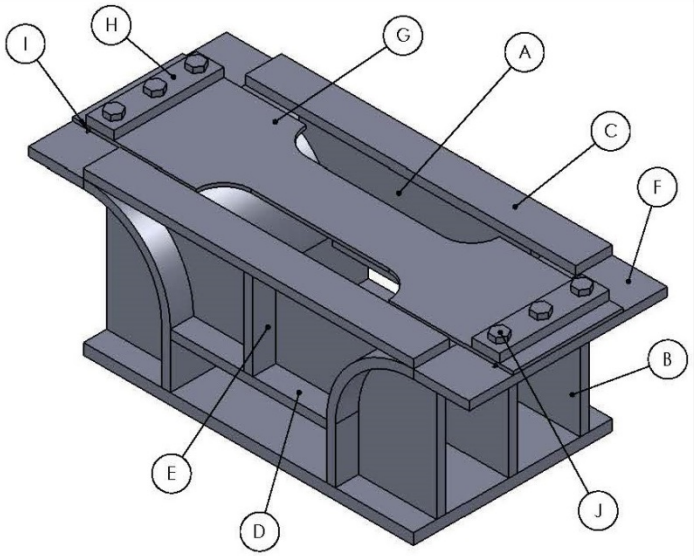

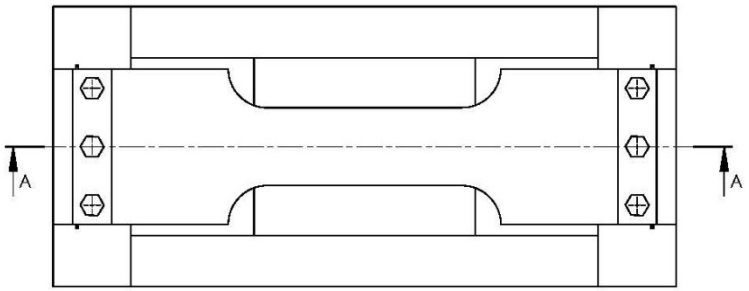

#	Item	Qty.	Thck. /Prop.
A	Longitudinal	2	5/8"
B	Curved Bracket	6	5/8'
C	Top Horizontal	2	5/8"
D	Lower Horizontal	2	5/8"
E	Vertical Rib	2	5/8"
F	Curved End	2	5/8"
G	Test Plate	-	1/4" or 1/8"
H	Upper Bar	2	5/8"
I	Key	4	5/8"
J	Bolt and Nut 5/8"	12	Grade 8

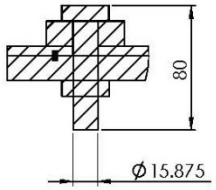

DETAIL B
SCALE 2 : 5

UNLESS OTHERWISE SPECIFIED: DIMENSIONS ARE IN MILLIMETERS SURFACE FINISH: TOLERANCES: LINEAR: ANGULAR:		FINISH:		DEBUR AND BREAK SHARP EDGES	DO NOT SCALE DRAWING	REVISION
	NAME	SIGNATURE	DATE		TITLE: Total Assembly	
DRAWN	A. Jamaly		03/26/14			
CHK'D						
APPV'D						
MFG						
Q.A				MATERIAL:	DWG NO. STePS2-N05-R02	A3
				WEIGHT:	SCALE:1:5	SHEET 1 OF 1

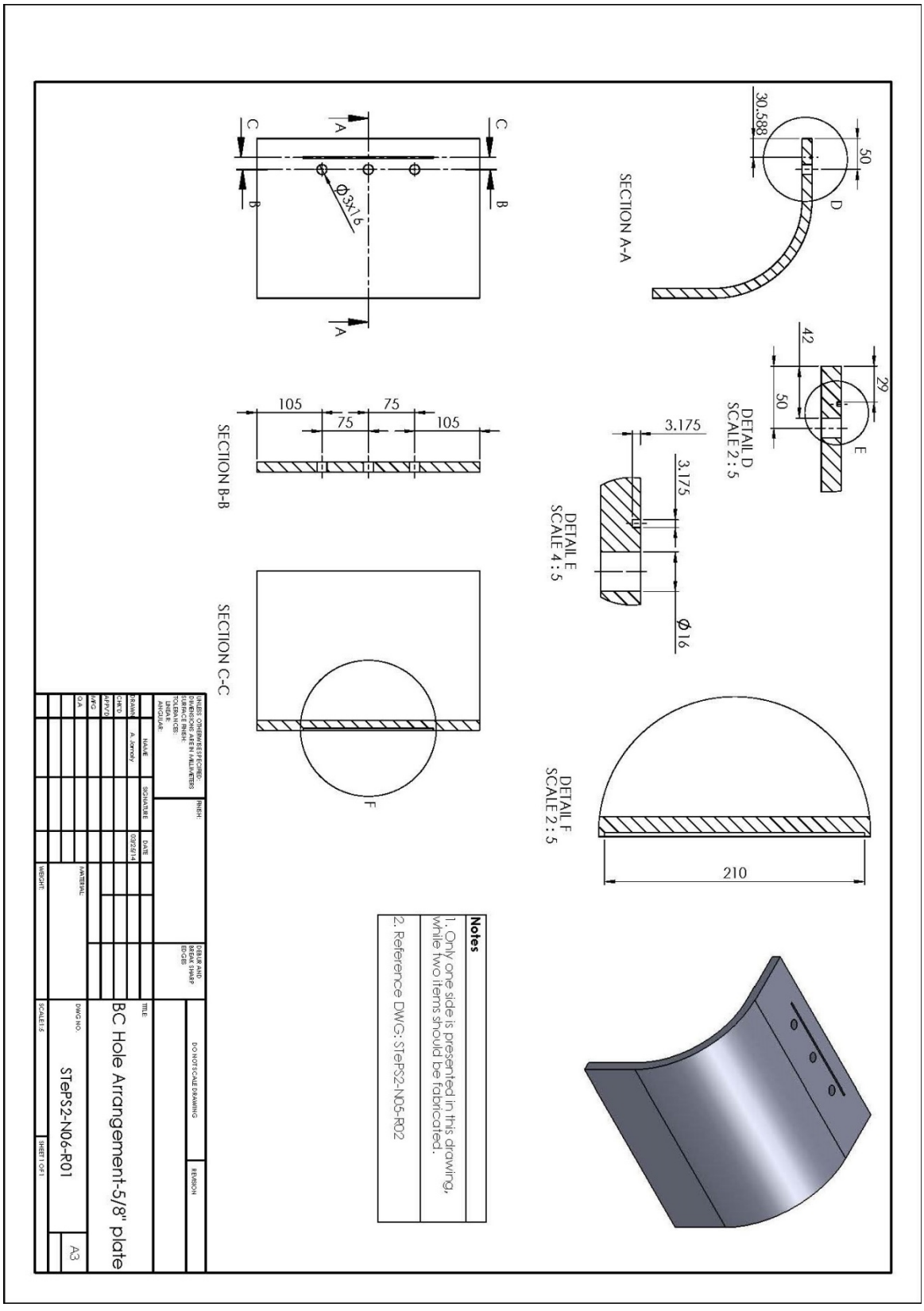
SECTION A-A
DETAIL D
SCALE 2 : 5
DETAIL E
SCALE 4 : 5
DETAIL F
SCALE 2 : 5
SECTION B-B
SECTION C-C
Notes
1. Only one side is presented in this drawing, while two items should be fabricated.
2. Reference DWG: STePS2-N05-R02
BC Hole Arrangement-5/8" plate
STePS2-N06-R01
A3

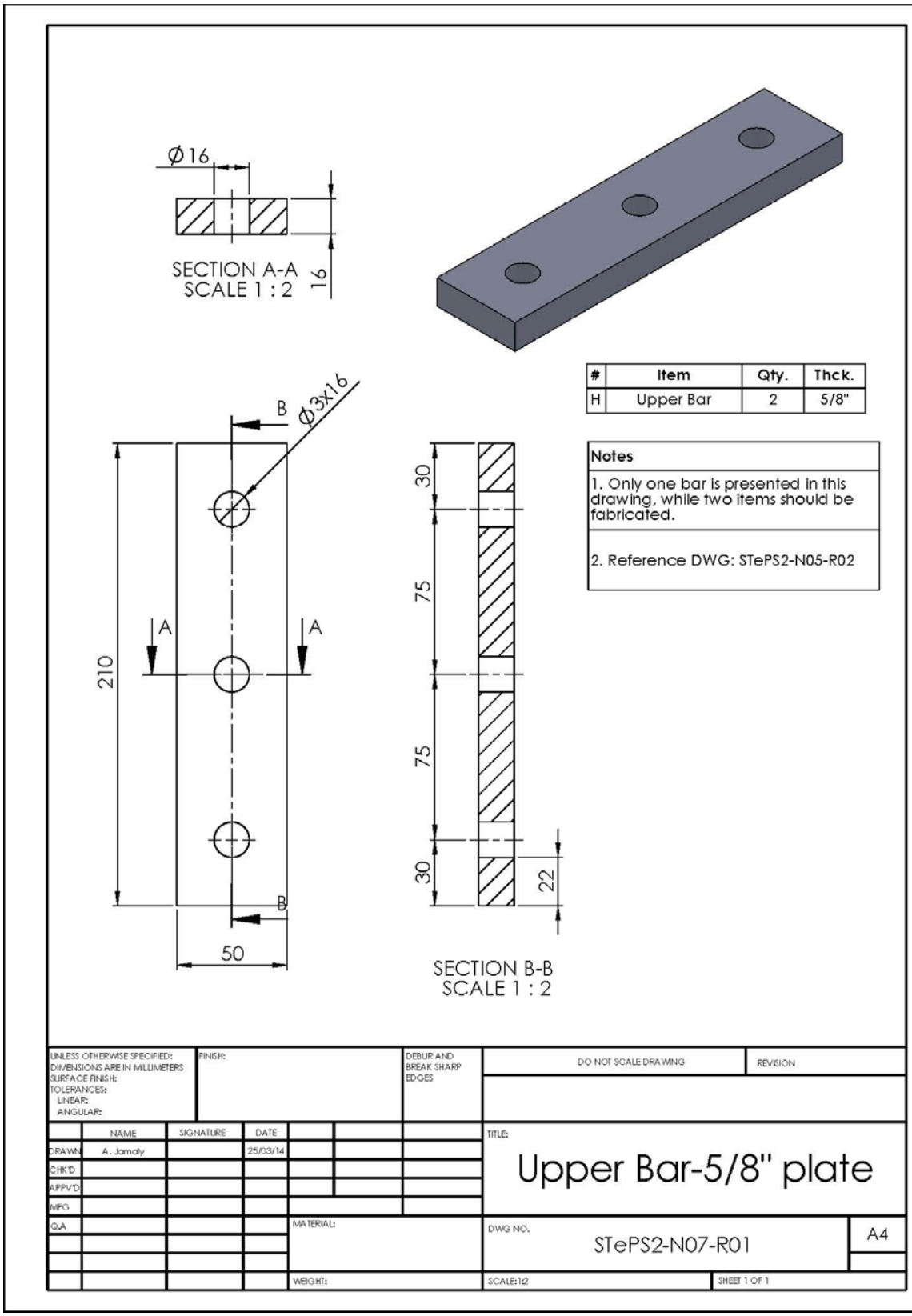
Ø16
SECTION A-A
SCALE 1 : 2
16
B
Ø3x16
A
A
210
B
50
30
75
75
30
22
SECTION B-B
SCALE 1 : 2
| Item | Qty. | Thck.
H | Upper Bar | 2 | 5/8"
Notes
1. Only one bar is presented in this drawing, while two items should be fabricated.
2. Reference DWG: STePS2-N05-R02
UNLESS OTHERWISE SPECIFIED:
DIMENSIONS ARE IN MILLIMETERS
SURFACE FINISH:
TOLERANCES:
LINEAR:
ANGULAR:
FINISH:
DEBUR AND BREAK SHARP EDGES
DO NOT SCALE DRAWING
REVISION
NAME | SIGNATURE | DATE
DRAWN A. Jamaly 25/03/14
CHK'D
APPV'D
MFG
Q.A
MATERIAL:
WEIGHT:
TITLE:
Upper Bar-5/8" plate
DWG NO.
STePS2-N07-R01
A4
SCALE:1:2
SHEET 1 OF 1

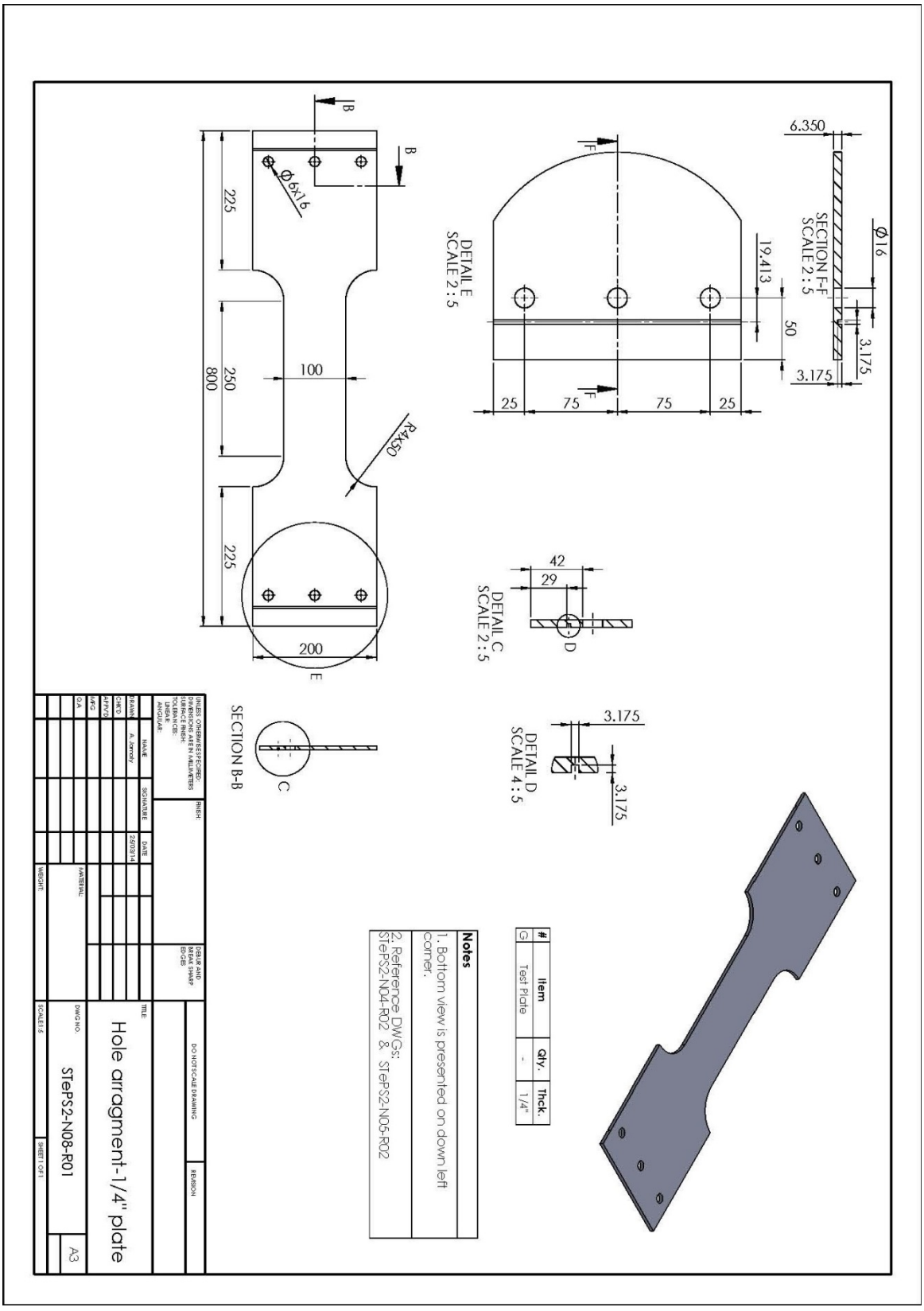
6.350
Ø16
3.175
3.175
SECTION F-F
SCALE 2 : 5
19.413
50
F
F
25
75
75
25
DETAIL E
SCALE 2 : 5
B
B
Ø6x16
225
250
800
100
R450
225
200
E
SECTION B-B
C
42
29
D
DETAIL C
SCALE 2 : 5
3.175
3.175
DETAIL D
SCALE 4 : 5
| Item | Qty. | Thck.
G | Test Plate | - | 1/4"
Notes
1. Bottom view is presented on down left corner.
2. Reference DWGs: STePS2-N04-R02 & STePS2-N05-R02
UNLESS OTHERWISE SPECIFIED: DIMENSIONS ARE IN MILLIMETERS SURFACE FINISH: TOLERANCES: LINEAR: ANGULAR
NAME
SIGNATURE
DATE
DRAWN
A. Jomaa
5/09/14
CHK'D
APPV'D
MFG
Q.A
MATERIAL
WEIGHT
FINISH
DEBUR AND BREAK SHARP EDGES
DO NOT SCALE DRAWING
REVISION
TITLE:
Hole arragment-1/4" plate
SCALE:1:5
DWG NO.
STePS2-N08-R01
A3
SHEET 1 OF 1

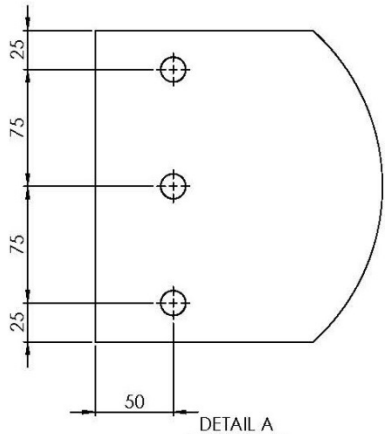

DETAIL A
SCALE 2 : 5

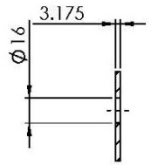

DETAIL C
SCALE 2 : 5

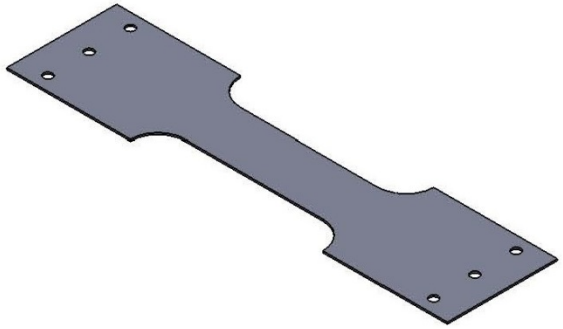

#	Item	Qty.	Thck.
G	Test Plate	-	1/8"

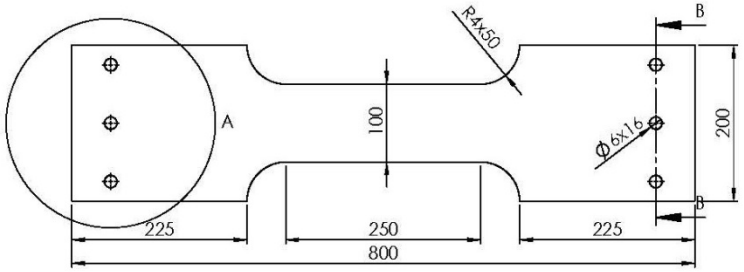

SECTION B-B

Notes
Please note that the thinner plate (1/8") does not have slot for key stock.
Reference DWGs: STePS2-N04-R02 & STePS2-N05-R02

UNLESS OTHERWISE SPECIFIED: DIMENSIONS ARE IN MILLIMETERS SURFACE FINISH: TOLERANCES: LINEAR: ANGULAR:	FINISH:	DEBUR AND BREAK SHARP EDGES	DO NOT SCALE DRAWING / REVISION
NAME / SIGNATURE / DATE			TITLE: Hole Arrangement-1/8" plate
DRAWN: A. Jamaly / 03/25/14			
CHK'D			
APPV'D			
MFG			
Q.A			
MATERIAL:			DWG NO. STePS2-N09-R01 / A3
WEIGHT:			SCALE:1:5 / SHEET 1 OF 1

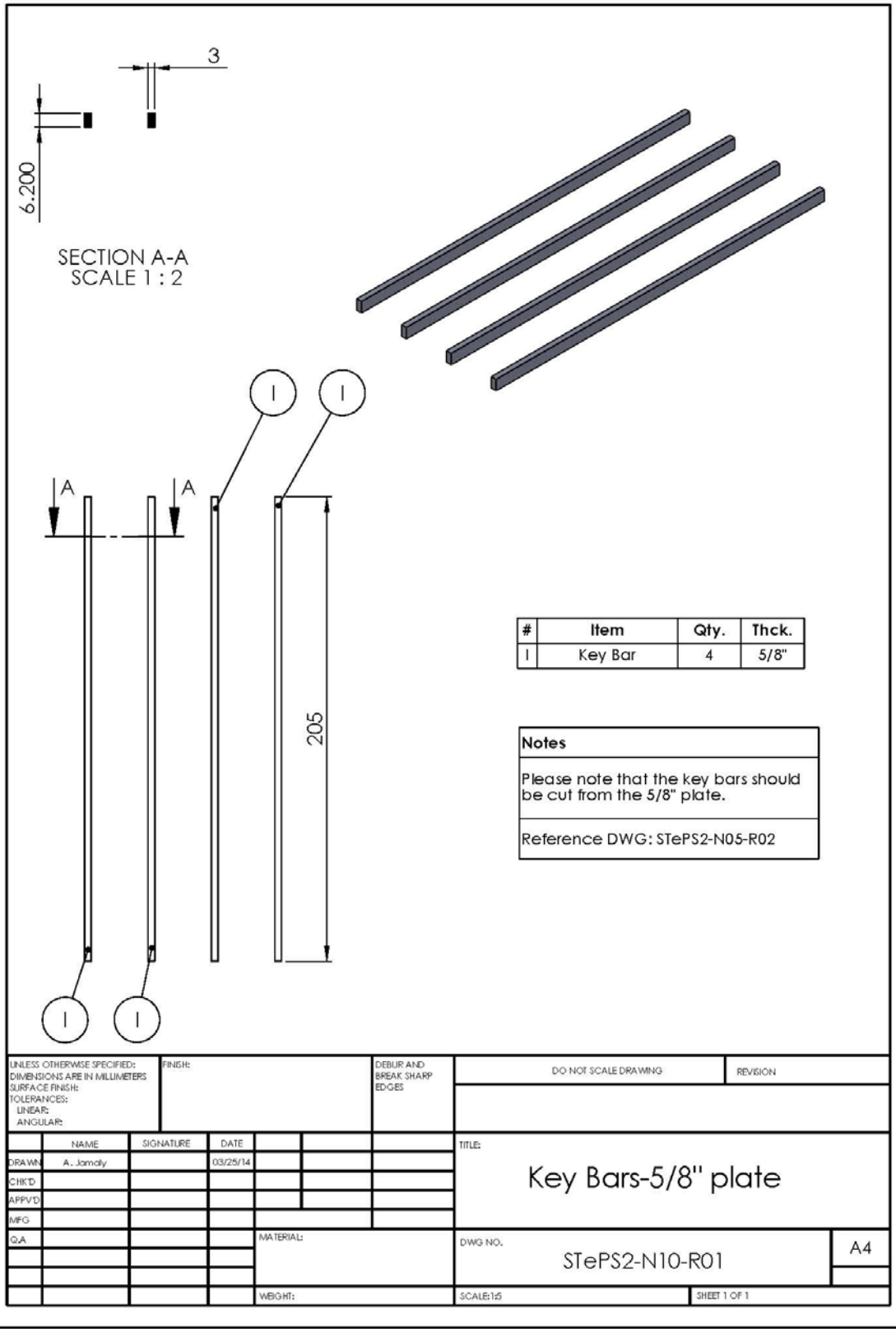

#	Item	Qty.	Thck.
1	Key Bar	4	5/8"

Notes
Please note that the key bars should be cut from the 5/8" plate.
Reference DWG: STePS2-N05-R02

UNLESS OTHERWISE SPECIFIED: DIMENSIONS ARE IN MILLIMETERS SURFACE FINISH: TOLERANCES: LINEAR: ANGULAR:		FINISH:		DEBUR AND BREAK SHARP EDGES		DO NOT SCALE DRAWING	REVISION
	NAME	SIGNATURE	DATE			TITLE: Key Bars-5/8" plate	
DRAWN	A. Jamaly		03/25/14				
CHK'D							
APPV'D							
MFG							
Q.A				MATERIAL:		DWG NO. STePS2-N10-R01	A4
				WEIGHT:		SCALE:1:5	SHEET 1 OF 1

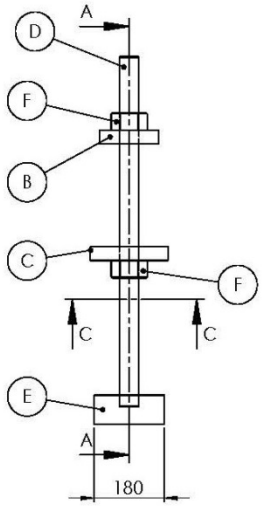

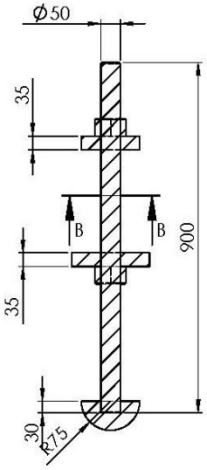

SECTION A-A

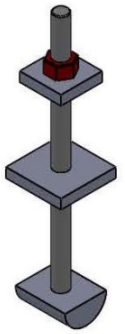

Notes
The threads dimension is not provided. Instead, a sample will be given with the drawings.
The bolt is not required to be fabricated. Please use the provided bolt.
The nuts are not required to be fabricated. The available nuts will be provided for threading dimensions.
Reference drawings: STePS2-N013-R02 & STePS2-N015-R01

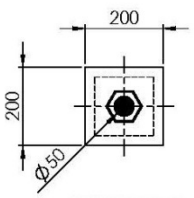

SECTION C-C

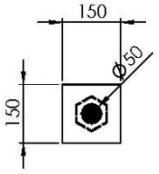

SECTION B-B

#	Item	Material	Dimension
E	Half Cylinder Indenter	Steel	Ø150, 180 mm
B	Upper Plate	Steel	150mmx150mmx1 2/5"
C	Lower Plate	Steel	200mmx200mmx1 2/5"
D	Bolt	Steel	Ø50mm
F	Nut	Steel	Sample

UNLESS OTHERWISE SPECIFIED: DIMENSIONS ARE IN MILLIMETERS SURFACE FINISH: TOLERANCES: LINEAR: ANGULAR:		FINISH:			DEBUR AND BREAK SHARP EDGES	DO NOT SCALE DRAWING / REVISION
	NAME	SIGNATURE	DATE			TITLE: Indenter Assembly-Steel
DRAWN	A. Jamaly		03/27/14			
CHK'D						
APPV'D						
MFG						
Q.A				MATERIAL:		DWG NO. STePS2-N14-R02 / A3
				WEIGHT:		SCALE:1:10 / SHEET 1 OF 1

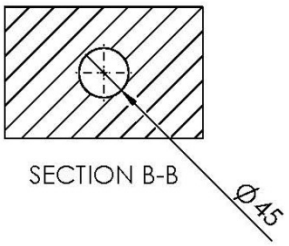

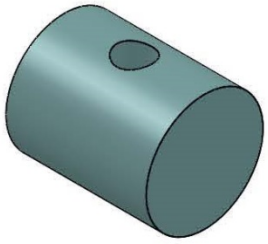

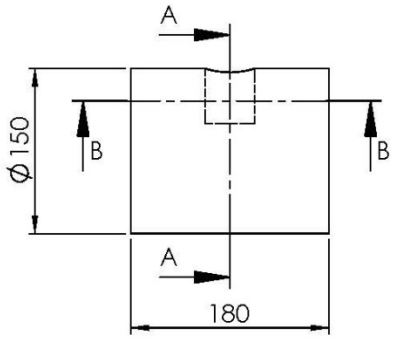

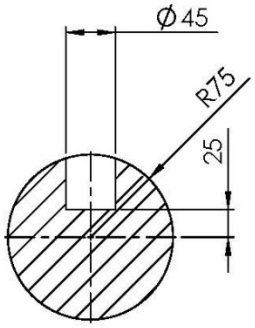

SECTION A-A

#	Item	Material	Dimension
A	Cylindrical Indenter	HDPE nylon	Ø150, 180 mm

UNLESS OTHERWISE SPECIFIED: DIMENSIONS ARE IN MILLIMETERS SURFACE FINISH: TOLERANCES: LINEAR: ANGULAR:		FINISH:			DEBUR AND BREAK SHARP EDGES	DO NOT SCALE DRAWING	REVISION
	NAME	SIGNATURE	DATE			TITLE:	
DRAWN	A. Jamaly		03/26/14			Indenter Layout-HDPE plastic	
CHK'D							
APPV'D							
MFG							
Q.A				MATERIAL:		DWG NO. STePS2-N12-R01	A4
				WEIGHT:		SCALE:1:5	SHEET 1 OF 1

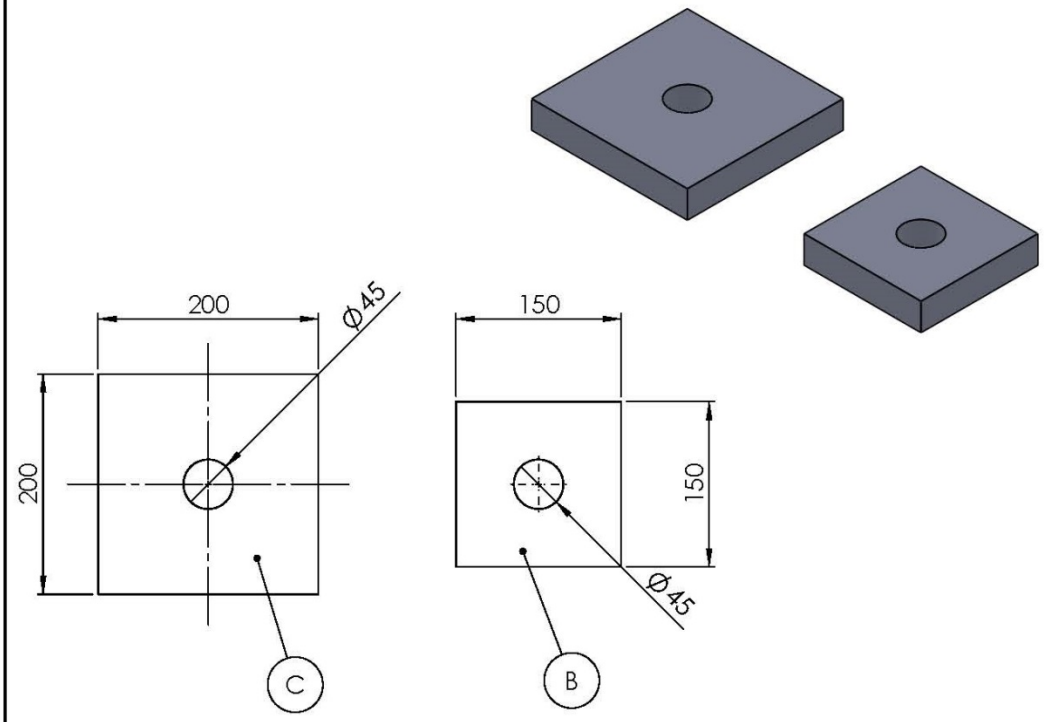

#	Item	Material	Dimension
B	Upper Plate	Steel	150mmx150mmx1 2/5"
C	Lower Plate	Steel	200mmx200mmx1 2/5"

UNLESS OTHERWISE SPECIFIED: DIMENSIONS ARE IN MILLIMETERS SURFACE FINISH: TOLERANCES: LINEAR: ANGULAR:		FINISH:			DEBUR AND BREAK SHARP EDGES	DO NOT SCALE DRAWING	REVISION
	NAME	SIGNATURE	DATE			TITLE:	
DRAWN	A. Jamaly		03/27/14			Indenter plates-1 2/5" plate	
CHK'D							
APPV'D							
MFG							
Q.A				MATERIAL:		DWG NO. STePS2-N13-R02	A4
				WEIGHT:		SCALE:1:5	SHEET 1 OF 1

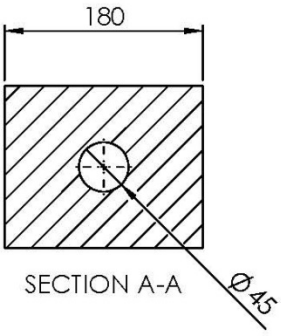

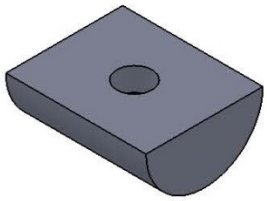

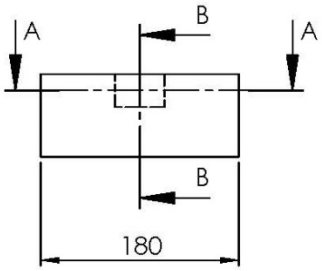

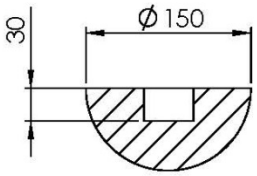

#	Item	Material	Dimension
E	Half Cyllinder Indenter	Steel	Ø150, 180 mm

UNLESS OTHERWISE SPECIFIED: DIMENSIONS ARE IN MILLIMETERS SURFACE FINISH: TOLERANCES: LINEAR: ANGULAR:		FINISH:			DEBUR AND BREAK SHARP EDGES	DO NOT SCALE DRAWING	REVISION
	NAME	SIGNATURE	DATE			TITLE:	
DRAWN	A. Jamaly		03/27/14			Indenter Layout-Steel	
CHK'D							
APPV'D							
MFG							
Q.A				MATERIAL:		DWG NO. STePS2-N15-R01	A4
				WEIGHT:		SCALE:1:5	SHEET 1 OF 1

Appendix 3: Specification of Test Machine, Sensors, and Cameras

Two sets of general purpose strain gauges are used in the experiment. Figure A3-1 shows the enlarged layout of the strain gauge. The particulars of the strain gauges are summarized in Table A3-1.

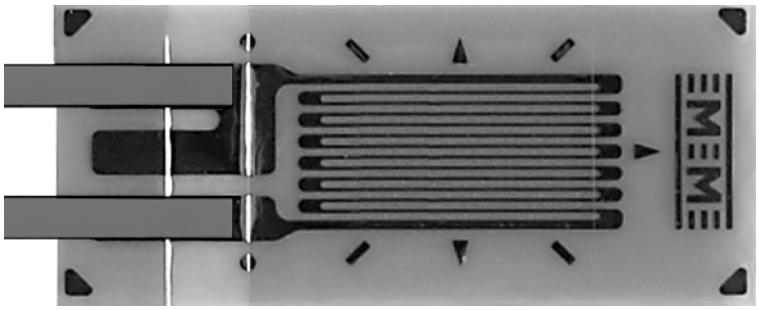

Figure A3-1. Enlarged layout of strain gauges used in the experiment

Table A3-1. Particulars of the strain gages

Gauge Type	**No. 1**	**No. 2**
Gauge designation	C2A-06-125LW-120	C2A-06-125LW-350
Resistance (Ohm)	120.0±0.6%	350.0±0.6%
Gauge factor (%/100°C)	+1.2±0.2	+1.3±0.2
Gauge length (mm)	3.18	
Overall length (mm)	6.05	
Grid width (mm)	1.78	
Overall width (mm)	2.03	
Matrix Length (mm)	8.00	
Matrix width (mm)	4.32	

Figure A3-2 shows the LVDT sensor used in the experiment.

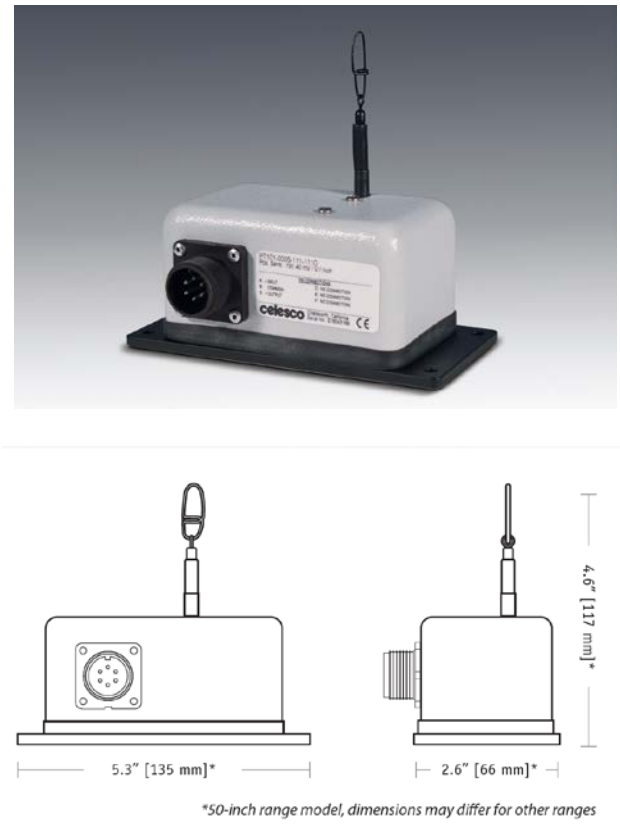

Figure A3-2. LVDT sensor

Technical specifications of the sensor are summarized in Table A3-2 below.

Table A3-2. Particulars of the LVDT sensor

Item	**Value**
Full stroke range	0-50 inches
Accuracy	0.1 %
Max acceleration	2 g
Cable exit	top exit
Electrical connection	terminal strip

Technical specifications of micro cameras are presented in Table A3-3.

Table A3-3. Technical specifications of micro cameras

Item	**Value**
Manufacturer	Leopard Imaging Inc.
Dimensions	L:40 mm, W: 30 mm, H:23 mm
Resolution	H:2592, V:1944
Pixel size	H:1.4 um, V: 1.4 um
Supply voltage	USB 2.0 or 5 VDC power source
Mass	8 g
Environment temperature range for operation	0 – 50 °C

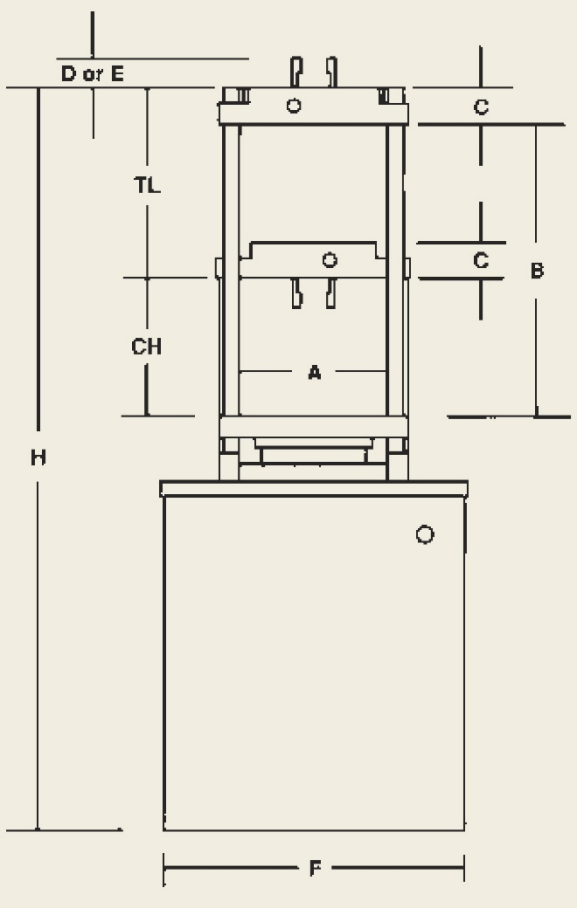

Figure A3-3. The layout of the test machine

The specifications of the test machine are summarized in Table A3-4, as follows, with reference to Figure A3-3:

Table A3-4. The specification of the test machine

Item	**Value**
Trademark	Tinius Olsen
Model	300 $_6$
Capacity	1500 kN
Stroke	229 mm
Testing speed	0-76 mm/min
Adjustable crosshead speed	305 mm/min
Clearance Between Screws (A)	610 mm
Standard Opening (B)	1175 mm
Crosshead Thickness (C)	216 mm
Grip Guard Thickness (D)	114 mm
Lever Height (E)	222 mm
Width (F)	940 mm
Depth (G)	851 mm
Height (H)	2445 mm
Machine Net weight	5444 kg
Machine gross weight	6034 kg

Appendix 4: Test Check Sheet

Lab work checklist

Sample No.: ……	Grid Spacing: ……	Date: ……
Indenter Type: ……	Indentation Speed: ……	Cutting Dir.: ……
Initial Gap: ……		

Test Specimen Marking	☐
Grips on Test Setup	☐
Grip on Position Sensor	☐
External Lights	☐
Internal Lights	☐
Enough Space on Camera Memories	☐
Laptop Battery Status (Cable Connection)	☐
Internal Cameras view	☐
External Cameras view	☐
Specimen Key stock and Bolts	☐
Connection of Cameras to Laptop	☐
Connection of Hard Drive to Laptop	☐
Correct address of location for recording videos	☐
Readiness of Recording devices - Position Sensor 1 - Position Sensor 2 - Strain Gauges - Load Cell	☐
Data recording log file	☐
Connection of Position Sensor to Specimen	☐
Starting the recording devices simultaneously with Camera Recording	☐
Fracture Location: ……	
Fracture Distance from Edge: ……	
Other Comments:	

References

Abraham J., Plastic Response of Ship Structure Subject to Ice Loading, M.Eng. Thesis, 2008, Memorial University of Newfoundland, St. John's

ABS Rules for Building and Classing Steel Vessels, Part 6, July 2014

ABS Rules for Testing and Certification of Materials, 2015

Alsos H. S., Analysis of Ship Grounding Assessment of Ship Damage, Fracture and Hull Girder Behavior, Norwegian University of Science and Technology, Trondheim, April 2008

Amdahl J. and Kavlie D., Experimental and Numerical Simulation of Double Hull Stranding, DNV - MIT Workshop on "Mechanics of Ship Collision and Grounding", 1992

Bamford and Stewart, Application of the IACS Common Structural Rules for Oil Tankers to FPSOs, OTC 18964

Bishop A., Petroleum Potential of the Arctic: Challenges and Solutions, Oilfield Review Winter 2010/2011: 22, no. 4., 2011

Bond J., Kennedy S., Physical Testing and Finite Element Analysis of Icebreaking Ship Structures in the Post-Yield Region, International Journal of Offshore and Polar Engineering, Volume 10, Pages 34-40, 2000

Common Structural Rules for Double Hull Oil Tankers and Common Structural Rules for Bulk Carriers, IACS, July 2012

Croasdale K.R., The Limiting Driving Force Approach to Ice Loads, K.R. Croasdale &Assocs. Ltd., OTC 4716

Daley C., Lecture Notes for Engineering 6003, Ship Structures II, Memorial University, St. John's, Canada, 2014

Daley C., Plating and Framing Design in the Unified Requirements for Polar Class Ships, POAC '01, Ottawa, Canada, 2001

Frontier Energy, Issue 7. Oil, gas and shipping in the Arctic and ice affected regions, Spring 2014.

Hughes et al., Ship Structural Analysis and Design, The Society of Naval Architects and Marine Engineers, 2010

Jamaly A., Seif T., Daley C., Analytical approach for predicting fracture in structures due to lateral ice indentation, ICETECH14, July 2014, Banff, AL, Canada

Kozarski N., Importance of Strain Hardening in Plastic Response of Rectangular Beams Subjected to Bending Loads, 2005, Master of Engineering, St. John's

Lamb T., Ship Design and Construction, The Society of Naval Architects and Marine Engineers, 2003

Marine Technology, Society of Naval Architects and Marine Engineers, October 2014

Minorsky V. U., An Analysis of Ship Collisions with Reference to Protection of Nuclear Power Plants. Journal of Ship Research, 3:1-4, 1959

MSC Res. 287(87), 2010, IMO, London

Okumoto Y. et al., Design of ship hull structures, A Practical Guide for Engineers, Springer, 2009

Paik et al., Ultimate Limit State Design of Ship Hulls, 2002, ABS Technical papers

Pill I., Tabri K., Finite Element Simulations of Ship Collisions: a Coupled Approach to External Dynamics and inner Mechanics, Analysis and Design of Marine Structures, 2009

Rahman M., Structural Resistance of Polar Ships and FPSO´S to Ice Loading, Norwegian University of Science and Technology, June 2012

Ratzlaff K.P., Kennedy D.J.L., Analysis of Continuous Steel Plates Subjected to Uniform Transverse Loads, Canadian Journal of Civil Engineering, Volume 12, Pages 685-699, 1985

Ratzlaff K.P., Kennedy D.J.L., Behaviour and ultimate strength of continuous steel plates subjected to uniform transverse loads, Canadian Journal of Civil Engineering, Volume 13, Pages 76-85, 1986

Sanderson T. J. O., Ice Mechanics-Risk to Offshore Structures, 1988

Seif T., Ductile Fracture Analysis in a Steel Plate by Cohesive Zone Modeling, M.Eng. Thesis, Memorial University of Newfoundland, July 2014

Simonsen, B. C. Ship Grounding on Rock: 1. Lyngby: Techn. Univ., Dep. of Ocean Engineering, 1997

Simonsen, B. C. Ship Grounding on Rock: 2. Lyngby: Techn. Univ., Dep. of Ocean Engineering, 1997

Simonsen B. C., Tornqvist R., Experimental and Numerical Modelling of Ductile Crack Propagation in Large-Scale Shell Structures, Marine Structures 17 (2004) 1–27.

SOLAS Reg. II-1/3-10

SSC 393

Stang, A. H., Greenspan, M., and Newman, S. B. Poisson's ratio of some structural alloys for large strains, Pages 211-221, Journal of Research of the National Bureau of Standards, 37, 1946.

Wang G., Arita K., Liu D., Behavior of a Double Hull in a Variety of Stranding or Collision Scenarios, Marine Structures, Volume 13, Pages 147-187, 2000.

Wierzbicki T., Simonsen B. C., Rupture Analysis of Oil Tankers in a Side Collision: Global Structural Model of Bow Indentation into Ship Side, Massachusetts Institute of Technology, 1996